行政院原子能委員會

委託研究計畫研究報告

SOFC 電池堆接合件高溫耐久機械性能分析(III)

Analysis of High-Temperature Mechanical Durability of SOFC Stack Joints (III)

計畫編號：1022001INER031

受委託機關（構）：國立中央大學

計畫主持人：林志光 教授

聯絡電話：03-4267340

E-mail address：t330014@cc.ncu.edu.tw

核研所聯絡人員：劉建國、吳思翰

報告日期：102 年 12 月

目錄

頁數

中文摘要

本研究主旨在探討固態氧化物燃料電池(SOFC)用 GC-9 封裝玻璃陶瓷和金屬連接板不銹鋼(Crofer 22 H)與 GC-9 封裝玻璃陶瓷和陶瓷電極板(PEN)接合件之介面破裂阻抗及破壞模式。藉由製作三款三明治試片，經不同時效處理在不同溫度下(25 ^{o}C-800 ^{o}C)測試，藉以評估不同溫度與時效處理對接合件介面破裂阻抗的影響。

實驗結果顯示，經過 100 小時時效處理後之封裝玻璃陶瓷與金屬連接板之接合介面破裂阻抗與時效處理前在不同溫度下並無明顯之差異。至於經過 1000 小時時效處理後之介面破裂阻抗與經過 100 小時處理後試片在相同溫度下有些許差異，推測與封裝玻璃陶瓷經過較長時效處理後結晶相的增加及介面裂紋成長於不同氧化層之間有關，然而隨著溫度變化的趨勢並無明顯之差異。在室溫至 700 ^{o}C 間，介面破裂阻抗會隨著溫度增加而提高，且破裂阻抗最大值發生在 700 ^{o}C，此乃 700 ^{o}C 高於 GC-9 之玻璃轉化溫度，使 GC-9 有明顯的黏滯現象，致使裂縫跨橋效應發生；在 700 ^{o}C 至 800 ^{o}C 則會隨著溫度增加而下降，主要是因為跨橋效應影響下降且 750 ^{o}C 高於玻璃軟化溫度，玻璃流動性大增所致。關於封裝玻璃陶瓷與陶瓷電極板接合件之介面破裂阻抗，僅在室溫下測試，裂縫會沿著介面成長，然而在其他高溫下，裂縫皆直接穿過陶瓷電極板並未沿著介面成長。實驗結果顯示，在室溫下，介面破裂阻抗經過 100 小時時效處理後有明顯的提升。

由微結構及破斷面分析顯示，封裝玻璃陶瓷與金屬連接板介面有兩種破壞模式。第一，脫層現象發生在玻璃陶瓷基材與鉻酸鋇層之界面。第二，脫層現象發生於鉻酸鋇層之內。對於封裝玻璃陶瓷與陶瓷電極板介面，裂縫於陶瓷電極板與玻璃陶瓷基材之介面以及在玻璃陶瓷基材裡成長。

另外，藉由對一款 SOFC 電池堆進行具有介面裂縫之有限元素熱應力

模擬分析，且將計算所得之圓形裂縫尖端在特定模態 I 及模態 II 比例角之應變能釋放率與實驗所得之介面破裂阻抗比對，發現該款 SOFC 電池堆所能容許最大的介面裂縫或缺陷尺寸為 70 μm。

Abstract

The interfacial fracture energy of glass-ceramic (GC-9)/metallic interconnect (Crofer 22 H) and glass-ceramic/PEN joints for solid oxide fuel cell (SOFC) stack is investigated using a four-point bending test technique. The interfacial fracture energy is determined at room temperature, 650 ^{o}C, 700 ^{o}C, 750 ^{o}C, 800 ^{o}C by testing three types of sandwich-like specimens. The effects of temperature and aging treatment on the interfacial fracture energy are studied.

A 100 h-aging treatment does not significantly influence the interfacial fracture energy of glass-ceramic/metallic interconnect joint. Compared with that of 100 h-aged condition, a difference is found for the 1000 h-aged interfacial fracture energy at each given temperature. It may result from change of crystalline phase content in a longer aging treatment and difference in fracture site. However, the variation trend of interfacial fracture energy with temperature is similar for all the given aged conditions. The interfacial fracture energy increases with temperature from room temperature to a peak value at 700 ^{o}C. As 700 ^{o}C is higher than the glass transition temperature (668 ^{o}C), a greater viscosity takes place and causes a crack bridging phenomenon. The interfacial fracture energy decreases at 750 ^{o}C due to a softening behavior of GC-9 as the temperature is higher than the softening temperature (745 ^{o}C). The interfacial fracture energy decreases further at 800 ^{o}C as a result of flowability of GC-9. For the glass-ceramic/PEN joint, interfacial cracking takes place only when the test is conducted at room temperature. At elevated temperatures, crack penetrates though PEN directly leading to specimen fracture without interfacial cracking.

Comparison of the interfacial fracture energy for non-aged and 100 h-aged specimens indicates the interfacial fracture energy increases after a 100 h-aging treatment.

Through analysis of interfacial microstructure, two types of fracture modes are identified for the glass-ceramic/metallic interconnect joint. Firstly, delamination takes place at the interface between the glass-ceramic substrate and chromate layer. Secondly, delamination occurs within the chromate layer. For the glass-ceramic/PEN joint, crack propagates along the interface between GC-9 and PEN and also kinks into the glass-ceramic layer.

A simulation through finite element analysis is conducted to calculate the energy release rate at the crack front of an interfacial circular crack placed at the highly stressed region in a prototypical SOFC stack subjected to thermal stresses. Comparison of the simulation and experimental results at specific mixity angles between Mode I and Mode II indicates that the critical crack or defect size at the interface of the joint of GC-9 glass-ceramic sealant and Crofer 22 H interconnect in the given SOFC stack is 70 μm.

1. INTRODUCTION

1.1 Solid Oxide Fuel Cell

A solid oxide fuel cell (SOFC) is one of the cleanest and most efficient devices for electric power generation. It converts chemical energy directly to electrical power without an intermediate step of conversion to heat such that the efficiency typically reaches about 50%. The heat which takes place during operation is recoverable for generation of electricity, so the efficiency of SOFCs with an integrated steam turbine system is higher than 90% [1]. Compared with other fuel cells, the most important features of SOFC are (1) that components are made of solids, (2) that electrochemical reactions occur without noble catalysts and solid oxides possess highly ionic conductivity at a high operation temperature of 600 ^{o}C-1000 ^{o}C, and (3) that internal reforming allows direct use of nature gas [2]. The typical SOFC configuration designs are tubular and planar cells. Planar SOFCs attract more attention because of lower fabricating cost, higher current density, and lower operating temperature [3,4].

The schematic of operating principle of an SOFC using hydrogen as fuel is shown in Fig. 1 [5]. Fuel and oxidant flow though the anode and cathode, respectively, to proceed electrochemical reactions at elevated temperature. The electrochemical reactions involved include,

Anode: $H_2 + O^{2-} \rightarrow H_2O + 2e^-$ (1)

Cathode: $\frac{1}{2}O_2 + 2e^- \rightarrow O^{2-}$ (2)

Overall: $H_2 + \frac{1}{2}O_2 \rightarrow H_2O$ (3)

For a unit cell, it is composed of a positive electrode-electrolyte-negative electrode (PEN) plate, interconnects, sealants, and a nickel mesh. To obtain a higher power density for electrical application, connecting unit cells in series through interconnects is necessary. Structural scheme of a planar SOFC stack is shown in Fig. 2 [6]. Interconnects connecting each cell and nickel mesh work as a current connector and fuel gas manifold. In a planar SOFC stack, hermetic sealants play an important role in keeping fuel and oxidant from mixing. Mixture of gases will generate damages of stack and decrease the electrochemical performance. Unfortunately, due to mismatch of coefficient of thermal expansion (CTE), there are great thermal stresses at sealant between dissimilar materials during operation. Therefore, the development of sealant for SOFC is one of the challenges to meet the reliability target.

1.2 Glass Sealant

For long-term reliability and performance, sealing in SOFCs is a critical issue. Sealants must have good resistance to both oxidizing and reducing environments and good chemical compatibility with adjacent components. Sealants developed for SOFC include rigid seals and compressive seals [2,4]. The compressive sealing such as mica-based sealants does not require a rigid bond with the other SOFC components; however, an application of constant load is needed. For compressive seals, requirement of CTE match between neighboring components is not as demanded as that in rigid seals. The developed materials for rigid seals include brazing, glass, and glass-ceramic sealants. For rigid seals, there is no need of any mechanically applied load but a more strict CTE match is required to prevent leakage and cracking [4]. For brittle glass and glass-ceramic sealants, they are susceptible to breaking when subjected to tensile stresses as a result of thermal mismatch. Glass sealants are commonly used in planar SOFC stacks because of generally lower price and easy application. The most important criteria for selection of a suitable glass-ceramic sealant are the glass transition temperature (T_g) and CTE [4,7,8].

A glass-ceramic sealant must provide sufficient viscosity and good wetting behavior for sealing, but it should not soften too much to flow during operation for maintaining sufficient rigidity and gas-tight seal. Thereafter, the operation temperature of a planar SOFC using glass-ceramic sealants must be higher than the T_g, which makes glass-ceramic sealants change from brittle to ductile. Glass-ceramics are a composite which consists of amorphous and crystalline phases. During operation and sintering process, the amorphous phases transform into crystalline phases. Although the strength of resulting sealants becomes stronger than that of the initial state, microvoids and cracks could be generated between these two phases as a result of CTE mismatch. The viscosity and flowability of amorphous phases contribute to relaxation of thermal stresses caused by thermal mismatch at operation. Material properties such as Young's modulus and CTE change with the degree of crystallization. Crystallization of a glass is dependent on its composition and thermal events so that controlling the crystallization is important to have suitable viscosity and wetting behavior.

Cracks and microvoids within a glass-ceramic sealant would influence the joint strength and structural integrity significantly. The SOFC operating temperature is commonly higher than T_g, which results in presence of viscosity and possibility of crack healing. Crack healing at elevated temperature makes the glass-ceramic sealants restore material properties [9-12]. It was evident that radial cracks created by Vickers indentation at room temperature tended to disappear after the samples were exposed to

elevated temperature for a certain length of time [7,9,10]. However, the pre-existing cracks in glass-ceramic sealants would grow slowly under corrosive agents such as humid atmosphere at operating temperature for a long period of time without applied load, and the phenomenon was called slow crack growth (SCG) [7]. The humidity is able to destroy the oxygen-silicon network [7].

Many compositions of glass and glass-ceramic sealants for planar SOFC have been developed. In the cases of barium-containing glass-ceramics for SOFCs, the formation of barium silicate leads to an increase in CTE [4]. Crystallization of a barium-containing glass is faster than that of one containing other alkaline-earth metal elements due to a lower activation energy of barium [4]. The influences of each constituent in a glass-ceramic sealant are different. Boron oxide is commonly used as a modifier in silicate glasses to decrease the T_g and zirconia is added to decrease the CTE [4].

Choi and Bansal [13] studied the mechanical properties of some glass sealants with different reinforcements. In the study of Zhao et al. [7], mechanical properties for glass-ceramic sealants of various compositions and reinforcements by metallic or ceramic fillers were investigated. Indentation was carried out for the materials after the joining process and additional aging at operation temperature, and the results revealed the elastic modulus, hardness, and fracture toughness increased with increasing aging time for some materials but decreased for the others [7]. It indicates that the mechanical properties are dependent on thermal events.

Several glass-ceramic systems have been developed for sealants in planar SOFCs. For example, BaO-CaO-Al_2O_3-SiO_2 (BCAS) glass systems have been developed and investigated [13-20], with a focus on a commercial BCAS glass, designated as G-18 (35 mol% BaO, 35 mol% SiO_2, 15 mol% CaO, 10 mol% B_2O_3, and 5 mol% Al_2O_3). A new glass-ceramic sealant (designated as GC-9) containing BaO, B_2O_3, Al_2O_3, and SiO_2 for intermediate-temperature planar SOFC at 700 ^oC-750 ^oC has been developed at the Institute of Nuclear Energy Research (INER). Mechanical properties of GC-9 at various temperatures were investigated by Chang [10]. In the study of Chang [10], in order to generate different degrees of crystallization, GC-9 samples were sintered at 850 ^oC and then aged at 750 ^oC for 4 h and 100 h, designated as non-aged and aged, sintered GC-9, respectively [10]. Results of Chang [10] revealed that the extent of crystallization was increased with an increasing aging time; otherwise, the types of crystalline phases were not changed. At temperature below T_g, there was a significant improvement of flexural strength at high temperature because of a crack healing effect, as compared to the room-temperature strength [10]. Even if mechanical strength of the aged GC-9 was increased, the ability for relaxing thermal stresses could diminish at high temperature because of a less amount of amorphous phases. Nevertheless, the strength and stiffness of both aged

and non-aged GC-9 glass-ceramics were decreased at temperature above T_g.

1.3 Joint of Glass-Ceramic Sealant, Metallic Interconnect, and Cell

In intermediate-temperature SOFCs (IT-SOFCs), glass-ceramic sealants are commonly used to join interconnects and cells. Figure 3 [8] shows the locations where sealants are used in a planar SOFC stack with metallic internal gas manifolds and metallic interconnects. Common seals include: (a) cell to metal frame; (b) metal frame to metallic interconnect; (c) frame/interconnect pair to electrically insulating spacer; (d) stack to base manifold plate [8]. Among these locations, sealing at (b) and (d) can be referred to as a joint of glass-ceramic sealant and metallic interconnect.

During cyclic operation of an SOFC, there is a buildup of thermal stresses leading the sealants to be subjected to tensile and shear stresses [21-23]. The failure of sealants could result in degradation of cell performance if the stresses exceed the corresponding strength of the joint. Therefore, it is necessary to investigate the mechanical properties of the joint between cell and metallic interconnect for assessment of the structural reliability of an SOFC. Because of the multi-layer structure in a joint, the mechanical properties of a joint do not belong to that of a single material while they are interfacial properties between dissimilar materials. Any interaction between the glass-ceramic sealant and interconnect may influence the mechanical properties of the joint.

Malzbender and Zhao [24] evaluated the Young's modulus, hardness, and fracture toughness of glass-ceramics using microindentation. Crofer 22 H/glass-ceramic/Crofer 22 H sandwich specimens were prepared to simulate the seal in a stack [24]. Results indicated that the Young's modulus, hardness, and fracture toughness were functions of the distance from the interface of metal and glass-ceramic [24]. It seems that the differences in material properties and residual stresses influence the strength of interface. A modified rupture testing technique was developed by placing a sealed disk specimen in a test fixture and pressurizing the backside of the sample until rupture of seal [25]. In that study, an anode-supported bilayer (NiO-5YSZ/5YSZ) and eight different ferritic stainless steels, five of which had a chromia scale and three of which had an alumina scale, were sealed using a G-18 glass-ceramic to make sealed disk specimens [25]. In addition to testing as-joined specimens, the sealed disk specimens after exposure to ambient air at 750 ^{o}C for various hold times were also tested [25]. Cyclic thermal testing was performed between room temperature and 750 ^{o}C for a number of cycles. The joint of alumina-forming ferritic steel substrates and G-18 was stronger than that of the others in both as-joined and aged conditions [25]. The two major factors in determining the joint strength are

the composition and thickness of the reaction zone between the metal's oxide scale and G-18 glass [25]. The barium chromate layer that grew on the chromia-forming steels exhibited poorer thermal expansion match and tended to become thicker at SOFC operating environments [25].

Stephens et al. [26] investigated the interfacial strength between the G18 glass-ceramic and Crofer 22 APU substrate at temperatures from 25 ^{o}C to 800 ^{o}C under both tensile and shear loading. Two different failure modes were observed in the tensile tests, bulk failure mode referring to failure occurring through the glass layer, and interfacial failure mode referring to failure occurring at the glass-metal interface [26]. In the study of Chen [27], the joint strength of GC-9 and Crofer 22 H was investigated under both tensile and shear loading at room temperature and 800 ^{o}C. For both tensile and shear joints, the joint strength decreases with an increase in temperature [27]. The fracture sites for the tensile joint are within the GC-9 layer at room temperature and 800 ^{o}C, while those for the shear joint are at the metal/chromia and glass/chromate interfaces, respectively [27]. In a further study by Yeh [28], the effect of interconnect with LSM coating on shear and tensile joint strength was investigated at 800 ^{o}C. There is a significant decrease in shear and tensile joint strength for samples with LSM coating because of generation of microvoids and micocracks in the chromate layer during sintering process [28]. Results indicate that both tensile and shear joint strength are lower than the flexural strength of GC-9 so that it is attributed to initiation and propagation of cracks within the interfaces [27,28].

In terms of mechanical strength of a joint, the interface between dissimilar materials is where cracks usually initiate and propagate so that it is the weakest part in a joint. The interfacial cracking resistance is important particularly for the joints involving brittle materials such as glass-ceramic sealants and PENs because of the pre-existing defects. Even though glass-ceramics have the ability to heal cracks at the SOFC operating temperature, the crack-healing ability is limited and cannot recover all kinds of cracks. In the study of Malzbender et al. [29], interfacial fracture energy was investigated for the joint of SOFC components using a four point bending test technique at room temperature in air. Firstly, to investigate the interfacial characteristics between the muti-layers within the PEN, the PEN was glued to a steel strip, and the notched anode side was used as a stiffener in the test [29]. The weakest part of the PEN with a composite cathode was found to be the interface between the functional layer and the mechanical support layer within the cathode [29]. Secondly, sandwich specimens with glass-ceramic sealant between two interconnect steel strips were used to determine the interfacial fracture energy for the glass-ceramic/interconnect joint, and a notch was made at one of the interconnect strips [29]. In order to investigate the effect of crystallization of glass-ceramic, some sandwich specimens were aged at 800 ^{o}C for one or five days [29]. The results

revealed that the cracking path was partly along the interface and partly within the glass-ceramic, which did not influence the interfacial fracture energy [29]. The interfacial fracture energy increases with increasing aging time [29]. For the specimens aged for five days, there is more interfacial delamination than that for specimens aged for one day, and the glass-ceramic has disintegrated into numerous chipping flakes [29].

On the other hand, a chromia layer is formed on the metallic interconnect side during sintering the joint of glass-ceramic and interconnect. Sun et al. [30] evaluated the interfacial adhesion strength of Crofer 22 APU and its oxide layer at room temperature using an indentation technique with a Rockwell ball indenter. The applied indentation load was from 60 kgf to 150 kgf, and scanning electron microscopy (SEM) was used to observe the delamination and spallation. Results indicated that under a certain indentation load, more spalled samples were observed with increasing oxide scale thickness [30]. For the specimens with a thicker oxide layer, full radial debonding of the scale was observed, while only partial flaking was observed in specimens with a thinner oxide layer [30].

Some other studies have investigated the fracture toughness of SOFC components such as bulk glass-ceramics and PENs [7,24,31,32]. In Ref. [29], the interfacial fracture energy for a multi-layer PEN and for a glass-ceramic/interconnect joint was investigated only at room temperature in air. However, SOFC stacks work at high temperature, but there is little work in literature related to the interfacial fracture energy of relevant joints at operating temperature. Thus, it is needed to investigate the interfacial fracture energy of relevant joints at SOFC working temperature.

1.4 Simulation of Cracking Behavior

Johnson and Qu [33] conducted a three dimensional (3D) numerical simulation to analyze fracture properties of PEN. A commercial finite element analysis (FEA) code, ANSYS, was used to create a simplified PEN with thermally induced stresses, and the area of high stresses was then determined [33]. The results of this analysis led to the consideration of three different fracture models, namely a vertical straight crack in the electrolyte, a vertical penny crack in the anode, and an interfacial penny crack between the anode and electrolyte [33]. A Fracture Mechanical Analyzer (FMA) code, which is a post-processing program capable of calculating fracture parameters, was employed in conjunction with the FEA programs [33]. In the first case of cracking in the electrolyte, it was found that the model geometry constrained significantly crack growth within the electrolyte itself and that the opening mode stress intensity factor K_I was virtually independent of crack length [33]. In the second case, the vertical crack in the anode was the most

likely source of failure, although the calculated stress intensity factor never exceeded the fracture toughness of the material [33]. Finally, the energy release rate calculated by the stress intensity factor never exceeded the critical value, so the interfacial delamination would not take place [33].

Nguyen et al. [34] investigated the damage and fracture issues of glass and ceramic materials used in SOFCs using both discrete and continuum damage models with a modified boundary layer (MBL) modeling approach. Analyses of an internal crack and of an interfacial crack between dissimilar materials were conducted using the MBL modeling approach [34]. Firstly, fracture toughness of the G18/YSZ interface as a function of the mode mixity was obtained using the discrete modeling associated with the MBL approach [34]. Secondly, the continuum damage model was used in the MBL analysis to determine the direction of propagation of a G18/YSZ interface crack [34]. Results revealed that the interfacial crack never propagated into the YSZ material which possesses much higher fracture energy [34].

In Refs. [33,34], the energy release rate was analyzed using a simplified model such that the structure and thermal condition of a complete SOFC stack was not taken into account. To study the structural integrity of an SOFC stack, it is necessary to investigate the interfacial energy release rate in an SOFC stack with a repeated, multi-layer cell structure.

1.5 Purposes

The high operating temperature enables SOFCs to have a superior efficiency of energy conversion while accompanying concerns such as degradation of materials as a result of undesirable reactions between components. The high-temperature operation of SOFC could cause significant thermal stresses because of CTE mismatch and temperature gradients. In an SOFC stack, it is difficult to repair sealants when they fail or fracture because they are bonded to several components, such as interconnects and PENs. When subjected to thermal stresses, some pre-existent pores or defects in a ceramic component such as PEN or glass-ceramic sealant could grow to failure and degrade the electrical performance of an SOFC system. As hermetic sealants are weaker than other components in the SOFC stack, a systematic investigation of mechanical properties of joints of glass-ceramic/metallic interconnect and glass-ceramic/PEN at room temperature to 800 ^{o}C is necessary for development of a reliable SOFC stack. Cracks may initiate at the interface of the joint of glass-ceramic/PEN and/or of the joint of glass-ceramic/metallic interconnect. It is thus important to study the interfacial cracking behavior for these two types of joints in the planar SOFC stack.

There are two parts in the present study. Firstly, interfacial fracture

energy of glass-ceramic/PEN and glass-ceramic/metallic interconnect joints is evaluated at room temperature to 800 ^{o}C. In order to investigate the effect of crystallization of glass-ceramic on the interfacial fracture energy, some samples are also tested after aging at 800 ^{o}C in air for a certain period of time to simulate the SOFC working environment. Fractographic and microstructual analyses are conducted with SEM and correlated with the mechanical testing results. Secondly, a commercial FEA code is applied to investigate the thermal stress distribution in a prototypical planar SOFC stack at operation and shutdown stages. The highly stressed regions at the glass-ceramic/metallic interconnect interface are identified. Cracks of various sizes are placed at these regions, and the stress intensity factors are calculated. In comparison with the interfacial fracture energy determined by experiment, the critical crack size which would lead to spontaneously interfacial delamination could be determined. It is hoped that results of the current study can provide some useful information for assessing the structural integrity of the planar SOFC stack.

2. MATERIALS AND EXPERIMENTAL PROCEDURES

2.1 Materials and Specimen Preparation

As shown in Fig. 3, the joint at location S1 is composed of PEN, glass-ceramic sealant, and interconnect, and that at locations S2 and S4 is classified as a joint of glass-ceramic sealant and metallic interconnect. In order to investigate the interfacial fracture energy of glass-ceramic/PEN and glass-ceramic/interconnect joints, three types of sandwich-like specimens were used in this study, as shown in Fig. 4. The metallic interconnect/glass-ceramic/notched metallic interconnect (Fig. 4(a)) and metallic interconnect/glass-ceramic/notched PEN (Fig. 4(c)) specimens were used to investigate the interfacial fracture energy of the glass-ceramic/interconnect joint for different mode mixity in fracture. The interfacial fracture energy of the glass-ceramic/PEN joint was evaluated by testing the PEN/glass-ceramic/notched metallic interconnect specimen (Fig. 4(b)).

The GC-9 glass sealant used in the present work was developed at INER for intermediate-temperature planar SOFC. The major chemical composition of the GC-9 glass sealant includes 0-40 mol% BaO, 0-40 mol% SiO_2, 0-15 mol% B_2O_3, 0-15 mol% CaO, 0-15 mol% La_2O_3, 0-10 mol% Al_2O_3, and 0-5 mol% ZrO_2. It was made by mixing the constituent oxide powders followed by melting at 1550 ^oC for 10 h. After melting, it was poured into a mold preheated to 680 ^oC to produce GC-9 glass ingots. The GC-9 glass ingots were then annealed at 680 ^oC for 8 h and cooled down to room temperature. GC-9 glass powders were made by crushing the as-cast glass ingots and sieving with 325 mesh sieves. The average size of the glass powder is 45 μm. Slurries were made by adding into the GC-9 powders the desired amounts of solvent (alcohol), binder (ethyl celluloid), and plasticizer (polyethylene glycol). Anode-supported half cell without cathode was provided by the vendor (Ningbo Institute of Material Technology and Engineering, Ningbo, China). The half cell (total thickness of about 400 μm) is composed of NiO-YSZ/YSZ. The thickness of the YSZ electrolyte is about 10 μm–15 μm. The interconnect used is a commercial ferritic stainless steel, Crofer 22 H (ThyssenKrupp VDM GmbH, Werdohl, Germany), which is a heat-resistant alloy developed for application in SOFCs. The plane dimensions of both cell and interconnect are 5 cm x 5 cm. The thickness of the interconnect plate is 2.5 mm. For the PEN/glass-ceramic/notched metallic interconnect specimen (Fig. 4(b)) and the metallic interconnect/glass-ceramic/notched PEN specimen (Fig. 4(c)), a slurry of GC-9 was spread both on the electrolyte side of PEN and one side of

interconnect. A slurry of GC-9 was spread on one side of each interconnect for the metallic interconnect/glass-ceramic/notched metallic interconnect sandwich specimen (Fig. 4(a)). The as-assembled sandwich specimens were then put into a furnace to dry the slurry at 80 ^{o}C.

The PEN/glass-ceramic/metallic interconnect and metallic interconnect/glass-ceramic/metallic interconnect sandwich plates were then joined under a compressive load through appropriate heat treatments. In order to simulate a practical assembling process of an SOFC stack, the applied compressive load is 12.25 kPa. In the sintering process, the jointed plates were firstly held at 500 ^{o}C for 1 h, heated to 900 ^{o}C, and held for 4 h. The heating rate at each step is 5 ^{o}C/min. After the jointing process, the thickness of GC-9 is about 0.6–0.7 mm. Each sandwich plate was then cut by a diamond saw into rectangular specimens with dimensions 4 mm x 3.5 mm x 45 mm and 4 mm x 5.6 mm x 45 mm (Fig. 4) for four-point bending test. A spark-erosion wire cutting technique or a diamond saw was used to generate the notch on each specimen. Some specimens were aged in air at 800 ^{o}C for 100 h or 1000 h to understand the effects of crystallization of the glass-ceramic sealant on the interfacial fracture energy. Machining direction was along the 45-mm-length longitudinal direction.

2.2 Four-Point Bending Test

Four-point bending tests were performed using a commercial closed-loop servo-hydraulic material test machine attached with a furnace. The flexural loading fixture (Fig. 5) with a 20-mm inner loading span and a 40-mm outer loading span was made of alumina in order to perform tests at 25 ^{o}C, 650 ^{o}C, 700 ^{o}C, 750 ^{o}C, and 800 ^{o}C. The specimen was heated to the specified temperature at a heating rate of 6 ^{o}C/min. The specimen was then held at the specified temperature for 3 min before applying the load. The load was applied under displacement control with a displacement rate of 0.005 mm/s. For each test, a CCD camera with a high magnification lens is applied to record the cracking process in the specimen during the loading period. Experimental set-up for the four-point bending test is shown in Fig. 6. The load-displacement relationship is recorded for each test to calculate the interfacial fracture energy. The recorded videography is used to identify the corresponding points in the load-displacement curve at various cracking stages. Five specimens are used for repeated four-point bending tests at each temperature.

In this study, each layer of the multi-layered specimen is assumed to be isotropic and behave in a linear elastic manner. As shown in Fig. 7 [35], the interfacial crack is subjected to a constant bending moment in a four-point bending test as long as it remains within the inner loading span. An

analytical estimate of the strain energy release rate can be obtained for cracks located between the inner loading points [36]. The strain energy release rate is in a steady state when the crack length is much larger than the thickness of the upper layer of the specimen [36]. Furthermore, the strain energy release rate is independent of crack length, and the crack length measurement is unnecessary for the four-point bending test [37,38]. The value of the strain energy release rate can be derived from the difference in strain energy in the uncracked and cracked specimens [29,37,39]. Based on Euler-Bernoulli beam theory with a plane strain condition for a uniform isotropic beam, the strain energy is [29]

$$U = \frac{(1-\nu^2)M^2}{2wEI} \tag{4}$$

where U is the strain energy, E is the Young's modulus, I is the moment of inertia of the beam cross section, w is the width of the specimen, v is the Poisson's ratio, and M is the bending moment between the two inner loading points and equal to $Pa/2$. P is the applied load and a is the distance between the outer and inner loading points. The load P is constant in the load-deflection curve as long as the interfacial crack propagates in a steady state condition [29].

The fracture energy of interfacial fracture between layer j and j+1 of a n-layered composite beam with a plane strain condition is given as [39]

$$G_{int} = \frac{P^2a^2}{8w}\left(\frac{1}{\Sigma_s} - \frac{1}{\Sigma_c}\right) \tag{5}$$

where Σ_s and Σ_c are beam stiffness of the debonded and intact regions, respectively, of the specimen shown in Fig. 7 and P is the applied load corresponding to the onset of the propagation of interfacial crack. The composite beam stiffness is be defined as [39]

$$\Sigma = \int_{beam} \frac{E(y)}{1-\nu^2(y)} y^2 dA \tag{6}$$

where y is the location from the neutral axis, $E(y)$ and $\nu(y)$ are the Young's modulus and the Poisson's ratio, respectively, at location y, and A is the cross-sectional area of the composite beam. The layers are numbered from 1 at the bottom to n at the top. For the intact regions in the specimen, the position of the neutral axis from the bottom surface (y_{in}) is defined as [29]

$$y_{in} = \frac{\sum_{i=1}^{n}\left(E_i w_i t_i\left(2\sum_{k=1}^{i-1} t_k + t_i\right)\right)}{2\sum_{i=1}^{n} E_i w_i t_i} \tag{7}$$

For the debonded regions in the specimen, the position of the neutral axis from the bottom surface (y_{deb}) is given as [29]

$$y_{deb} = \frac{\sum_{i=1}^{j}\left(E_i w_i t_i\left(2\sum_{k=1}^{i-1} t_k + t_i\right)\right)}{2\sum_{i=1}^{j} E_i w_i t_i} \tag{8}$$

where E_i is the Young's modulus, w_i is the width, and t_i is the thickness for a rectangular cross section of layer i in the specimen.

The critical interfacial stress intensity factor K_{int} for a plane strain condition can be determined as [29]

$$K_{int} = \sqrt{G_{int} E'_{int}} \tag{9}$$

where the interfacial elastic modulus E'_{int} between layers j and $j+1$ is defined as [29]

$$\frac{1}{E'_{int}} = \frac{1}{2}\left(\frac{1}{E'_j} + \frac{1}{E'_{j+1}}\right) \tag{10}$$

where the Young's modulus of layer j for a plane strain condition (E'_j) is defined as

$$E'_j = \frac{E_j}{1-\nu^2} \tag{11}$$

2.3 Microstructural Analysis

After four-point bending test, some samples were cut along the longitudinal direction to observe the cross section of the joint to investigate the interfacial cracking characteristics in the joint. The cross sections were finely polished to optical finish. SEM was also employed to examine the interfacial morphology between the glass-ceramic sealant, metallic interconnect, and PEN. An energy dispersive spectrometer (EDS) module

attached to the SEM was used for composition analysis in order to determine various elemental distributions in the interfacial fracture surface.

3. MODELING

3.1 Finite Element Model

A commercial FEA code, ABAQUS, was applied to analyze the thermal stress distributions and stress intensity factors in a 3-cell planar SOFC stack at both room temperature and operating temperature. The FEA model was constructed based on the stack design developed at INER. Because the geometry of the planar SOFC stack is symmetric, only one half of the stack configuration is needed for building up a 3D FEA model. In the current study, such a 3D model was constructed for a SOFC stack consisting of three unit cells. Each unit cell is composed of a PEN assembly, interconnect, glass-ceramic sealant, and nickel mesh. The three unit cells were bonded together through glass-ceramic sealants to become a 3-cell SOFC stack. Figure 8 shows the schematic of this planar multi-cell SOFC stack. The plane area of the PEN and interconnect used here is 80 × 80 mm^2 and 150 × 100 mm^2, respectively. The thickness of PEN is 0.7 mm while the thickness of interconnect and frame is between 2 and 2.5 mm depending on the location of the flow channel. The operating temperature profile was firstly determined by an integrated electrochemical and thermal analysis at INER, and the thermal stress distributions and stress intensity factors were subsequently calculated by importing the temperature profile into the FEA model. There are two models applied in determining thermal stress distributions and stress intensity factors, respectively. For the model used to analyze the thermal stress distributions without cracks, an 8-node linear solid element (C3D8R) [40] was employed in this study.

Generally, in most cases the singularity at a crack tip should be considered in small-strain analysis. Including the singularity in the analysis often improves the accuracy of the stress intensity factor calculation because the stresses and strains in the region close to the crack tip are more accurate [41]. Therefore, in addition to the C3D8R element, 6-node linear solid element (C3D6) [40], 15-node quadratic solid element (C3D15) [40], 20-node quadratic solid element (C3D20R) [40], and the collapsed element (C3D20R) were also employed in the FEA model with cracks to calculate stress intensity factors. In the present study, $r^{-1/2}$ for a linear elastic fracture mechanics (LEFM) application was applied by degenerating the C3D20R element into a collapsed element by moving the nodes on the collapsed face of the edge planes together and moving the nodes to the 1/4 points, as shown in Fig. 9. The strain singularities applied in small-strain LEFM analysis are [41].

$$\varepsilon \propto r^{-1/2} \tag{12}$$

The collapsed element and quadratic elements such as C3D15 and C3D20R were used at the region around the interfacial crack, as shown in Fig. 10 where the different colors represent different materials. Figure 11 shows the focused and refined mesh configuration around an interfacial circular crack. The local cracking region (Fig. 10) is much smaller than that of the global model, and it varies with the interfacial crack size. Except the local cracking region, the linear elements such as C3D6 and C3D8R were applied in the other part of the global model

3.2 Material Properties

Material properties used in the FEA model are described below. Considering an anode-supported PEN is primarily composed of anode material (Ni/YSZ), temperature-dependent elastic modulus of anode was used as that for PEN (see Table 1) [25]. As shown in Table 1, the elastic modulus of PEN is decreased with increasing temperature. Table 2 is the tensile properties of Crofer 22 H used as frame and interconnect [42]. The resultant stress-strain curves of Crofer 22 H at different temperatures (Fig. 12) reveal that the tensile strength and elastic modulus are decreased with increasing temperature [42]. These stress-strain curve data are imported into the FEA models.

Table 3 shows the Young's modulus of GC-9 glass-ceramic with variously aged conditions at different temperatures [28], and that of the non-aged GC-9 was used in FEA analysis. Table 4 [43,44] lists the elastic properties of nickel mesh. The elastic modulus of nickel mesh is obtained by assuming that there's 95 vol.% of porosity in nickel mesh such that 5% of the elastic modulus of bulk nickel is used for nickel mesh [43]. The elastic modulus of nickel decreases with increasing temperature at a rate of 0.003675 GPa/^{o}C [44]. It was therefore assumed that the elastic modulus was decreased from 9.9 to 7.1 GPa when nickel mesh was heated from 25 to 800 ^{o}C. Figure 13 shows the variation of thermal expansion behavior with temperature for each SOFC component. The Poisson's ratio of Crofer 22 H and GC-9 at various temperatures is assumed to be 0.3. Except Crofer 22 H which can deform inelastically, the PEN, nickel, and GC-9 were assumed elastic in solving the thermal stress distribution. However, based on LEFM, the linear elastic material property of Crofer 22 H is used only in the local region (Fig. 10) of the model applied in determining the stress intensity factors.

3.3 Boundary Conditions

Figure 14 shows a plane-support at the bottom of the FEA model for

analysis. The bottom surface of the bottom interconnect is constrained in *z* direction. Along the symmetric plane, translation in the *y* direction is constrained. A fixed constraint is applied to a point on the symmetric plane to prevent translation of the whole stack model. The interfaces between glass-ceramic and interconnect/frame are all constrained by a tight constraint condition. The PEN, frame, and glass-ceramic sealant are boned together and considered as one component in the FEA analysis, but the material properties of PEN, frame, and glass-ceramic sealant are set for each appropriate part in that component. Similarly, the nickel mesh and interconnect are set as a component. The interfaces between other connecting pairs of components, including PEN with interconnect and PEN with nickel mesh are all constrained by a contact constraint condition. In general, the stress caused by self weight of SOFC components is relatively small compared to the thermal stresses such that it is neglected in the simulation. To simplify the analysis, friction between contact pairs is not considered.

3.4 Temperature Profile

To solve the thermal stress distribution at steady-state operation, temperature profile at operation stage is needed. The steady-state temperature profiles are generated through an approach combining electrochemical and heat-transfer analyses developed in a previous study using a 3-cell-stack heat-transfer model [47]. That study [47] used a counter-flow stack configuration which produces a greater power density compared to other flow patterns. The calculation procedure integrated electrochemical reactions in the SOFC with an FEA model for thermo-mechanical analysis of the interconnect through iteration processes so that a unified temperature distribution with heat loss effect was obtained [47]. The obtained temperature profiles in the whole 3-cell stack are shown in Fig. 15 and imported into the 3D FEA model for solving thermal stress distributions and stress intensity factors. It is also assumed that in-plane temperature gradients are much larger than cross-plane gradients in each component layer such that the temperature gradient through the thickness in each layer is neglected.

3.5 Investigated Cases

3.5.1 Thermal stress analysis

As mentioned above, thermal stress distributions in the given planar

SOFC stack at room temperature and operating temperature are solved using the commercial ABAQUS code. As a GC-9 glass-ceramic is used as sealants, unit cells are assembled together to form a multi-cell SOFC stack at 800 ^{o}C or above. The SOFC stack is assumed to be stress free initially at such an assembling temperature (800 ^{o}C). After the assembling process, the multi-cell stack is then slowly cooled down to room temperature for future operation. In the following thermal stress analyses, the residual stresses in the SOFC stack at room temperature before operation are first calculated by considering a temperature drop from 800 ^{o}C of the stress-free condition to room temperature. Then, the thermal stresses at operation stage are evaluated with consideration of such existing residual stresses. Therefore, the sequence of temperature fields imported into the FEA model in the current study takes the following order: (1) uniform distribution at 800 ^{o}C, (2) uniform distribution at room temperature, and (3) non-uniform temperature profile at operation stage, as shown in Fig. 16.

3.5.2 Calculation of stress intensity factor

As in LEFM for homogeneous isotropic solid, the interfacial fracture energy and the interfacial stress intensity factor are used to describe the mechanical behavior of interfacial cracks [48]. The fracture energy quantifies the change in potential energy accompanying an increment of crack extension; the stress intensity factor characterizes the stress, strain, and displacement around the crack tip [48]. The fracture energy describes global behavior while the interfacial stress intensity factor is a local parameter [48].

To perform a stress intensity factor calculation, the crack tip, crack front, seam, and the virtual crack extension direction should be defined. Duplicate overlapping nodes on the seam are generated, and these coincident nodes are free to move apart when the seam separates, as shown in Fig. 17 [49]. The crack tip and seam of a circular crack are placed at the highly stressed region in the interface of glass-ceramic/interconnect joint which is identified in the thermal stress analysis. The virtual crack extension direction is set along the interface and in the radial direction for the embedded circular crack. Initially, the diameter of the embedded circular crack is set to be 100 μm to calculate the stress intensity factors and energy release rate in the given 3-cell SOFC stack for comparison with the experimental fracture resistance. After that, the crack size is adjusted to find the critical crack size such that the calculated energy release rate at the highly stressed region is equal to the experimental interfacial fracture energy. Contour integral is used to calculate interfacial stress intensity factors in the ABAQUS code [49]. Figures 18 and 19 illustrate how ABAQUS code computes successive contour integrals for 2D and 3D models, respectively, by adding layers of elements.

The sequence of imported temperature profile is the same as that in thermal stress analysis (Fig. 16). In the present study, the crack tip and crack front of the given interfacial circular crack are defined as a line such that the first contour is defined by specifying the nodes at the crack tip [41]. In calculating stress intensity factor, the first contour integral may not be accurate [41]. To check the accuracy for these contours, results of the first five contours are selected to compare with that of the first contour [41]. Values of the stress intensity factor are considered good if the results are approximately constant from one contour to the next [41]. Finally, the stress intensity factors at various positions along the crack front can be determined.

4. RESULTS AND DISCUSSION

Based on Eq. (5) in Section 2.2, the interfacial fracture energy is dependent on geometrical parameters, material properties at various temperatures, and the critical load corresponding to the onset of interfacial cracking. The material properties of Crofer 22 H and GC-9 are given in Table 2 [42] and Table 3 [28], respectively. The Young's modulus of PEN is determined as 232.9 GPa using a ring-on-ring test at room temperature. The Poisson's ratio of Crofer 22 H, GC-9, and PEN is assumed to be 0.3. Due to constant material properties and small variation in specimen geometry, the critical load which causes propagation of an interfacial crack is the key parameter in determining the interfacial fracture energy at a given temperature. Therefore, how to determine the critical load in the load-displacement curve is very important.

Usually, two types of interfacial crack extension take place during four-point bending test: (1) stable propagation, also known as crack creeping and (2) nonstable propagation, also called crack bursting [39]. Which type of propagation takes place is attributed to the variation of interfacial fracture energy with position of interfacial crack and to the factors dependent on the beam stiffness [39]. During crack creeping of an interfacial crack within the inner loading span, the interfacial fracture energy is independent of crack length and is almost constant. Therefore, the applied load does not change with increasing displacement in the load-displacement curve [29,38,39]. When the crack bursting occurs, a load drop can be found in the load-displacement curve. The load corresponding to the onset of crack propagation in Eq. (5) is defined as [39]

$$P = \sqrt{P_1 P_2} \tag{13}$$

where P_1 and P_2 are the maximum and minimum load during the load drop, namely the load before and after the load drop, respectively.

4.1 Interfacial Cracking Resistance of Glass-Ceramic/Metallic Interconnect Joint

4.1.1 Non-aged metallic interconnect/glass-ceramic/notched metallic interconnect

There are two glass-ceramic/interconnect interfaces in the joint specimen of Fig. 4(a). To distinguish the position, the interface near the notch is called the first interface, and the other is called the second interface thereafter.

Figure 20(a) shows the load-displacement relationship at room temperature. In the outlined region, the applied load becomes stable and is independent of the increasing displacement. No crack was observed in the recorded video-graphy corresponding to that region. Perhaps, it is because the CCD camera records only one side of the joint specimen during test or the crack is too sharp and small to observe. However, there is a significant difference in the stiffness of specimen, namely slope of the load-displacement curve, between the outlined region and the preceding linear portion. Therefore, it is thought that the crack which initiates at the notch penetrates through the glass-ceramic layer (middle part of Fig. 20(b)) and then propagates along the second interface, as shown in Fig. 20(b). The interfacial fracture energy and critical interfacial stress intensity factor are thus determined using the constant load value in that plateau. When the crack leaves the inner loading span after the crack creeping region, the applied load increases again due to a termination of crack propagation [29,36,38,39].

There are two load drops in the load-displacement curve obtained at 650 ^{o}C (Fig. 21(a)). Cracking at the first and second load drop is shown in Fig. 21(b) and 21(c), respectively. Each load drop is attributed to initiation of a crack, followed by penetration through the glass-ceramic layer and propagation along the second interface. Because propagation of an interfacial crack is included in first load drop, the interfacial crack propagation is classified as a type of crack bursting. The first load drop is thus used to determine the interfacial fracture energy.

As shown in Fig. 22(a), the load initially increases with increasing displacement until the maximum value is reached. Then, the load decreases as a result of initiation of cracks at notch, penetrating through the glass-ceramic layer and propagating along the second interface, as shown in Fig. 22(b). The load becomes stable when the crack length is much larger than the thickness of the intact layer of the specimen [36]. Consequently, the load in the outlined region of Fig. 22(a) is applied to calculate the interfacial fracture energy.

The load-displacement relationship for the joint specimen tested at 750 ^{o}C is shown in Fig. 23(a). The curve is similar to that for specimen tested at 700 ^{o}C (Fig. 22(a)). Cracks penetrate through the glass-ceramic layer and propagate along the second interface (Fig. 22(b)). The load-displacement relationship and cracking pattern for 750 ^{o}C show a similar behavior to that for 700 ^{o}C such that the load used to calculate the interfacial fracture energy is also taken from the stable region outlined in Fig. 22(a).

As shown in Fig. 24(a), two distinct plateaus are outlined in the load-displacement curve obtained at 800 ^{o}C. At the first plateau, crack propagates along the first interface (Fig. 24(b)). Then, the crack penetrates through the glass-ceramic layer and propagates along the second interface (Fig. 24(c)). Therefore, the loads in the first and second plateau are both

used to calculate the interfacial fracture energy at various interfaces.

4.1.2 100 h-aged metallic interconnect/glass-ceramic/notched metallic interconnect

Figure 25(a) shows the load-displacement relationship obtained at room temperature for a 100 h-aged specimen. In comparison with the load-displacement relationship for a non-aged specimen (Fig. 20(a)), there is no obvious difference between each other. Crack initiates at the notch, penetrates through the glass-ceramic layer, and propagates along the second interface, as shown Fig. 25(b). The fracture behavior and cracking pattern at room temperature for non-aged and 100 h-aged specimens are similar so that the load in the outlined stable region is used to calculate the interfacial fracture energy, as shown in Fig. 25(a).

There are three load drops in the load-displacement curve obtained at 650 ^{o}C for a 100 h-aged specimen (Fig. 26(a)). The first load drop indicates initiation of a crack, penetration through the glass-ceramic layer, and propagation along the second interface (Fig. 26(b)). The crack opening displacement increases abruptly at the second load drop (Fig. 26(c)) in comparison with that at the first load drop (Fig. 26(b)). Therefore, the second load drop is attributed to a release of strain energy against the resistance of interfacial crack propagation. The other crack which initiates and propagates into the second interface (Fig. 26(d)) causes the third load drop. Because the onset of interfacial crack propagation takes place in the first load drop, the type of crack propagation is classified as crack bursting. The first load drop is thus used to determine the interfacial fracture energy.

The load-displacement relationship obtained at 700 ^{o}C for a 100 h-aged specimen is shown in Fig. 27(a), and the load initially increases with increasing displacement until the maximum value is reached. Then, the load decreases and becomes stable as a result of initiation of cracks at notch, penetrating through the glass-ceramic layer and propagating along the second interface, as shown in Fig. 27(b). The crack propagation is classified as crack creeping. The constant load in the outlined stable region of Fig. 27(a) is applied in calculating the interfacial fracture energy for the 100 h-aged specimen.

The load-displacement relationship for a 100 h-aged specimen tested at 750 ^{o}C is shown in Fig. 28(a). The curve which consists of two load drops is similar to that for a non-aged specimen tested at 650 ^{o}C (Fig. 21(a)). Crack penetrates through the glass-ceramic layer and propagates along the second interface for both load drops (Fig. 28(b) and 28(c)). The fracture pattern at 750 ^{o}C is also similar to that for a non-aged specimen tested at 650 ^{o}C such that the first load drop in Fig. 28(a), crack bursting, is used to calculate the

interfacial fracture energy.

As shown in Fig. 29(a), a distinct plateaus is outlined in the load-displacement relationship for a 100 h-aged specimen tested at 800 ^{o}C. Cracks initiate and penetrate through the glass-ceramic layer, followed by propagation along the second interface (Fig. 29(b)). For such a crack creeping behavior, the interfacial fracture energy is determined using the constant load in the plateau.

4.1.3 1000 h-aged metallic interconnect/glass-ceramic/notched metallic interconnect

Figure 30(a) shows the load-displacement relationship obtained at room temperature for a 1000 h-aged specimen. Cracks initiate at the notch, penetrate through the glass-ceramic layer, and propagate along the second interface, as shown Fig. 30(b). The load in the outlined stable region is used to calculate the interfacial fracture energy, as shown in Fig. 30(a).

There are three load drops in the load-displacement curve obtained at 650 ^{o}C for a 1000 h-aged specimen (Fig. 31(a)). Cracking patterns at 650 ^{o}C for 100 h-aged and 1000 h-aged specimens are similar. The first load drop indicates initiation of a crack, penetration through the glass-ceramic layer, and propagation along the second interface (Fig. 31(b)). Consequently, the first load drop is used to calculate the interfacial fracture energy.

In the load-displacement relationship obtained at 700 ^{o}C (Fig. 32(a)), the load initially increases with increasing displacement until the maximum value is reached. Then, the load decreases and becomes stable as a result of initiation of cracks at notch, penetration through the glass-ceramic layer, and propagation along the second interface, as shown in Fig. 32(b). The crack propagation is classified as crack creeping. The constant load in the outlined stable region of Fig. 32(a) is applied in calculating the interfacial fracture energy for the 1000 h-aged specimen.

As shown in Fig. 33(a), a distinct plateaus is outlined in the load-displacement relationship for a 1000 h-aged specimen tested at 750 ^{o}C. Cracks initiate and penetrate through the glass-ceramic layer, followed by propagation along the second interface (Fig. 33(b)). For such a crack creeping behavior, the interfacial fracture energy is determined using the constant load in the plateau.

The load-displacement relationship for a 1000 h-aged specimen tested at 800 ^{o}C is shown in Fig. 34(a). Crack initiates and penetrates through glass-ceramic, and then propagates along the second interface (Fig. 34(b)). The interfacial fracture energy is also determined using the constant load in the plateau.

4.1.4 Metallic interconnect/glass-ceramic/notched PEN

Figure 35(a) shows the load-displacement relationship obtained at room temperature for a joint specimen of metallic interconnect/glass-ceramic/notched PEN. In the load-displacement curve, there are a plateau and a small load drop. In comparison with the load-displacement relationship for non-aged metallic interconnect/glass-ceramic/notched metallic interconnect tested at room temperature (Fig. 20(a)), the plateau is caused by a crack which initiates from the notch and propagates along the second interface (Fig. 20(b)). The load in the plateau (Fig. 35(a)) is used to calculate the interfacial fracture energy.

4.1.5 Interfacial fracture energy and critical interfacial stress intensity factor

For interfaces which are significantly less tough than the neighboring bulk materials, a crack will grow along the interface [35]. Usually, when the energy release rate is larger than the interfacial fracture energy, an interfacial crack will propagate. However, the interfacial fracture energy varies between pure opening mode ($\psi = 0^o$) and pure shearing mode ($\psi = 90^o$). The mixity angle, ψ, is defined as [35]

$$\psi = \tan^{-1}\left(\frac{K_{II}}{K_I}\right) \tag{14}$$

where K_I and K_{II} are the stress intensity factors in opening mode and shearing mode, respectively. Both the geometry of specimen and the relative elastic properties can influence the mixity angle [35]. In the present study, the four-point bending test involves combinations of normal and shear displacements along the crack such that the interfacial fracture energy determined by the analytical formula given in Section 2.2 is a mixed-mode fracture energy. Therefore, the critical interfacial stress intensity factor (K_{int}) is also different from K_{Ic} of pure opening mode and is also classified as a mixed mode of failure. As only the interfacial fracture energy can be determined from the experimental data, determination of the mixity angle for the given four-point bending tests is made with the help of an FEA analysis described below.

For determining the mixity angle, a 2D FEA model used to calculate K_I and K_{II} by ABAQUS code is introduced an interfacial crack in the four-point bending specimen under plane strain condition. Due to symmetry of specimen, an half specimen such as metallic

interconnect/glass-ceramic/metallic interconnect and metallic interconnect/glass-ceramic/PEN joints with an interfacial crack is modeled, but the notch is not considered in the model. Because the interfacial fracture energy is independent of crack length when a crack is within the two inner loading points, the crack length is set to be 1 mm in the model. The applied load, *P*, is obtained from the experimental load-displacement curve, as discussed above. Based on the specimen configurations and experimental observations, three models (Fig. 36) with an interfacial crack at different interfaces are constructed for calculating stress intensity factors, and the virtual crack extension is set along the specific glass-ceramic/metallic interconnect interface. The mesh configuration of metallic interconnect/glass-ceramic/metallic interconnect with a crack at the second interface (Fig. 36(a)) is shown as an example in Fig. 37. The mesh configuration for the other two models (Fig. 36(b) and 36(c)) is similar. The contour integral is used to calculate the interfacial fracture energy and stress intensity factors such as K_I and K_{II} in ABAQUS code. The calculated interfacial fracture energy by FEA model is then compared with the experimental value to validate the numerical approach. Once it is confirmed, the stress intensity factors K_I and K_{II} for the given four-point bending tests can be obtained from the FEA analysis results. The difference between the interfacial fracture energy calculated by ABAQUS and that determined by experimental data and fracture mechanics formula is less than 10%. In this regard, the FEA models are validated and the calculated stress intensity factors can be used to determine the mixity angle by Eq. (14). The interfacial fracture energy and critical stress intensity factor are determined using Eqs. (5) and (9), respectively. Tables 5-8 list the experimentally determined interfacial fracture energy and critical stress intensity factor (average value and standard deviation) for the given joint specimens at various temperatures.

As described above, the interfacial fracture energy is not constant, and it varies with mixity angle. For non-aged, 100 h-aged, and 1000 h-aged specimens, the mixity angle ranges from 45^o to 49^o, except that at the first interface of non-aged specimen at 800 ^{o}C. It is attributed to the difference in the location of interfacial crack [50]. Interfacial crack at the first interface causes a negative mixity angle, while that at the second interface results in a positive mixity angle [50]. For the close mixity angles, it indicates a similar loading configuration during test. Figure 38 shows the average interfacial fracture energy of non-aged, 100 h-aged, and 1000 h-aged glass-ceramic/metallic interconnect joints at the given temperatures. Note that the non-aged average interfacial fracture energy at 800 ^{o}C in Fig. 38 is calculated from the second interface to be consistent with other temperatures. Results indicates that there is no obvious difference between non-aged and 100 h-aged conditions, and the trends of variation with temperature in the

curves for non-aged, 100 h-aged, 1000 h-aged specimens are similar. For a given aged condition, the interfacial fracture energy increases from room temperature to 700 ^{o}C (Fig. 38). The fracture energy is generally expected to increase at higher temperature because materials become tougher and softer. The thermal properties of the non-aged GC-9 bulk glass, such as T_g, and softening temperature (T_s) are 668 ^{o}C and 745 ^{o}C, respectively [10]. For the GC-9 after various aged conditions, the T_g and T_s increase a little bit from that for the non-aged GC-9 [10]. A maximum interfacial fracture energy takes place at 700 ^{o}C. As 700 ^{o}C is higher than T_g (668 ^{o}C), a greater viscosity takes place and causes a bridging phenomenon (Fig. 39) in the crack at the glass-ceramic/metallic interconnect interface. It needs more energy to overcome the bridging barriers for driving the interfacial crack to propagate. The interfacial fracture energy decreases at 750 ^{o}C and it is attributed to a softening behavior of GC-9 as the temperature is higher than T_s (745 ^{o}C). The interfacial fracture energy decreases further at 800 ^{o}C as a result of flowability of GC-9. Non-aged, 100 h-aged, and 1000 h-aged conditions show a similar trend in the variation of interfacial fracture energy with temperature indicating the glassy phase plays a very important role in determining the interfacial fracture resistance of the GC-9/Crofer 22 H joint.

Although the trend of curves for variously aged conditions is similar, the interfacial fracture energy for 1000 h-aged condition is different from the other aged conditions at certain temperatures. It may result from the change of crystalline phase content in a longer aging treatment. For the 1000 h-aged specimen, interfacial fracture energy is smaller at 650 ^{o}C due to a greater brittleness of crystalline phases. At 700 ^{o}C and 750 ^{o}C, interfacial fracture energy becomes larger for the 1000 h-aged condition as compared to the other aged conditions. This is due to a different cracking path in the interfacial oxide layers and will be discussed in next section. At 800 ^{o}C, the interfacial fracture energy for variously aged conditions is comparable because the testing temperature is higher than T_s. In this regard, the interfacial fracture energy is dominated by the residual glassy phase at 800 ^{o}C. At room temperature, the residual glassy phase becomes brittle leading to a comparable interfacial fracture energy value for all the given aged conditions.

4.1.6 Failure analysis

Formation of adhesive oxide layers is the main mechanism of interfacial joining between the glass-ceramic sealant and metallic interconnect. The bonding strength of the joint originates from a mutual Van Der Waals force of the formed oxide layers. The high-temperature joining mechanism of the GC-9 glass-ceramic sealant and Crofer 22 H alloy involves formation of two oxide layers with a chromia (Cr_2O_3) layer on the surface of Crofer 22 H and a

chromate ($BaCrO_4$) layer on the surface of GC-9 [27]. A spinel ($(Cr,Mn)_3O_4$) layer is formed between these two oxide layers. Figure 40 shows the location of each oxide layer between Crofer 22 H and GC-9 glass-ceramic.

Figure 41 shows the failure patterns in the non-aged metallic interconnect/glass-ceramic/notched metallic interconnect specimens tested at various temperatures. Due to symmetry of failure pattern, only an half specimen with both sides of fracture surface is shown for all cases, and the notch is at the right side of each micrograph. In other words, the interfacial crack propagates from the right side toward the left side during test. As a fast breaking action is taken to separate the unbroken portion after test for observing the fracture surfaces, the surface near the left edge is not uniform and will not be discussed. It is found that delamination occurs uniformly at the cracking region in each optical micrograph, and some of the delaminated regions are further observed and analyzed by SEM and EDS. For the non-aged specimen tested at room temperature, Fig. 42 shows the SEM micrographs of a selected area in the upper and lower micrograph of Fig. 42(a), respectively. The protrusions in Fig. 42(a) are the counterparts of the indentations in Fig. 42(b). For the non-aged specimen tested at 650 ^oC, the microstructure in Fig. 43 is similar to that in Fig. 42. By means of EDS analysis, the detected chemical elements in Fig. 43(a) and 43(b) are listed in Tables 9 and 10, respectively. The Cr, Ba, and O elements are detected in both Fig. 43(a) and 43(b) such that the interfacial crack propagates within a chromate layer. Note that the existence of Mn element indicates a thin chromate layer adhered on the upper Crofer 22 H side.

Fig. 44 shows the SEM micrographs corresponding to the OM micrographs of Fig. 41(c) for non-aged specimens tested at 700 ^oC. There is amorphous phase in Fig. 44(a). In addition to the amorphous phase, needle-shape crystalline phases (alpha-Ba($Al_2Si_2O_8$)) are observed in Fig. 44(b). The amorphous phase is likely associated with the bridging phenomenon at 700 ^oC (Fig. 39). As Cr, Ba, and O elements are detected by EDS analysis, the amorphous phase is mixed with chromate. For the oxide layers formed between GC-9 and Crofer 22 H, the chromate layer is adjacent to GC-9. Because the needle-shape crystalline phases are found in the lower micrograph and there is no crystalline phase on the corresponding upper fracture surface, it implies the crack propagation is along the interface between GC-9 and chromate layer. For the non-aged specimen tested at 750 ^oC, SEM micrograph of the upper micrograph in Fig. 41(d) is shown in Fig. 45. At region 1, needle-shape crystalline phases and microstructural features of GC-9 are observed (Fig. 45(b)). At region 2, it shows microstructure of chromate with needle-shape imprints (Fig. 45(c)). In the SEM micrograph (Fig. 46(a)) of the lower micrograph of Fig. 41(d), the amorphous phase is not as intact as that in Fig. 44(b). For the outlined region of Fig. 46(a), a typical microstructure of alpha-Ba($Al_2Si_2O_8$) is observed, as shown in Fig. 46(b). It

indicates that the chromate with needle-shape imprints is caused by separation of alpha-Ba($Al_2Si_2O_8$) from chromate. The damaged amorphous phase (Fig. 46(a)) is a leftover from the glass-ceramic adhered on the other fracture surface (Fig. 45(a)). Therefore, the crack mostly propagates along the interface between GC-9 and chromate. Figure 47 shows the SEM micrographs for the first interface of non-aged specimen tested at 800 ^{o}C. Note that Fig. 41(e) shows failure patterns at the first interface. The microstructure at both locations of interfacial crack is similar. The amorphous phase is observed, and there are no needle-shape crystalline phases in both upper and lower fracture surfaces. Consequently, the delamination takes place within the chromate layer.

Figure 48 shows the failure patterns of the 100 h-aged metallic interconnect/glass-ceramic/notched metallic interconnect specimens tested at various temperatures. In general, the microstructure of the upper and lower micrographs for 100 h-aged specimens are similar to that for non-aged specimens at each given temperature, even though the location of interfacial crack is different at 800 ^{o}C.

Figure 49 shows the failure patterns in the 1000 h-aged metallic interconnect/glass-ceramic/notched metallic interconnect specimens tested at various temperatures. For the 1000 h-aged specimen tested at room temperature, Fig. 50 shows the SEM micrographs of a selected area in the upper and lower micrograph of Fig. 49(a), respectively. The protrusions and indentations are found in Fig. 50(a) and 50(b), respectively. The fracture site is within the chromate layer as evidenced by EDS analysis. For the other temperatures, the microstructure of fracture surfaces is similar to that of room temperature. Table 11 gives a summary of fracture site for non-aged, 100 h-aged, and 1000 h-aged specimens. As described in Section 4.1.5, interfacial fracture energy of 1000 h-aged specimens tested at 700 ^{o}C and 750 ^{o}C is higher than that of 100 h-aged ones. It may be related to a difference in the fracture site (Table 11). As shown in Table 11, interfacial cracking at 700 ^{o}C and 750 ^{o}C takes place at the GC-9/chromate interface for non-aged and 100 h-aged specimens, while it occurs within the chromate layer for 1000 h-aged specimens. However, for 100 h-aged and 1000 h-aged specimens tested at various temperatures, the feature at peripheral edges of the fracture surface is different from that in the interior (Figs. 48 and 49). It is caused by growth of oxide layer during aging treatment. At the periphery of a specimen, oxygen in air enables the oxidization to take place, while oxidization is limited by absence of oxygen at the region inside the specimen. It is also found that the thicker oxide region at periphery becomes wider for a longer aging time.

Cross-sectional microstructures of the interface between GC-9 and Crofer 22 H at variously aged conditions are shown in the SEM micrographs of Fig. 51 with a back-scattered electron (BSE) mode. The black layer on

GC-9 glass-ceramic is the chromate layer. Apparently, the chromate layer in Fig. 51(a) is much thinner, while a greater thickness of chromate is observed in Fig. 51(b) and 51(c). It indicates that the chromate layer becomes thicker after the aging treatments, and the thickness of oxide layer in 1000 h-aged condition seems slightly thicker than that in 100 h-aged condition.

4.2 Interfacial Cracking Resistance of Glass-Ceramic/PEN Joint

4.2.1 PEN/glass-ceramic/notched metallic interconnect

For both non-aged and 100 h-aged PEN/GC-9/Crofer 22 H joint specimens, crack initiates at the notch, penetrates through glass-ceramic, and propagates along the interface between the electrolyte of PEN and glass-ceramic only when test is conducted at room temperature. At 650, 700, 750, and 800 ^{o}C, crack penetrates though PEN directly resulting in specimen fracture without interfacial cracking. It seems that the fracture toughness of PEN becomes smaller than that for glass-ceramic/PEN interface at elevated temperatures. Similarly, the specimen after 1000 h-aged tested at room temperature also is fractured by penetrating glass-ceramic and PEN.

Figure 52 shows the load-displacement curves for non-aged and 100 h-aged specimens. The two curves are similar. Firstly, the load increases linearly with increasing displacement. This linear portion represents storage of strain energy for initiation of crack at the notch. Next, crack initiates and penetrates through the glass-ceramic layer, followed by propagation along the interface between glass-ceramic and PEN (Fig. 52(c)) so that load decreases and becomes constant and independent of displacement. Finally, load increases again because the interfacial crack reaches the inner loading point. The applied load in each outline region of Fig. 52 is used to calculate the interfacial fracture energy and imported into an FEA model for determining the mixity angle. The FEA model is shown in Fig. 53, and the length of interfacial crack is set to be 1 mm. The mesh configuration is similar to that shown in Fig. 37. Fracture resistance of the non-aged and 100 h-aged PEN/GC-9/Crofer 22 H joints is listed in Table 12. The mixity angles for both aged conditions are similar indicating a similar loading configuration during test. As given in Table 12, the interfacial fracture energy of glass-ceramic/PEN joint increases after a 100 h-aging treatment.

4.2.2 Failure analysis

Figure 54 shows the failure patterns of the non-aged and 100 h-aged PEN/glass-ceramic/notched metallic interconnect specimens tested at room

temperature. There is no difference between Fig. 54(a) and Fig. 54(b). Some white spots of GC-9 are left in the upper micrograph of both conditions. By means of EDS analysis, element distributions in the white spots are confirmed and shown in Fig. 55. As shown in Fig. 55(b) and 55(c), a high intensity of Ba is found in the region of GC-9, and the region having a high intensity of Zr agrees with the corresponding YSZ region. Therefore, the crack propagates along the interface between GC-9 and YSZ and also kinks into the glass-ceramic layer.

4.3 Simulation of Interfacial Crack in Glass-Ceramic/Metallic Interconnect Joint

4.3.1 Thermal stress analysis

Figure 56 shows the distributions of maximum principal stress in glass-ceramic at the interface between glass-ceramic and interconnect in an SOFC stack at room temperature and operation stage. Note that the stress distributions presented are for the elements adjacent to the interface. As shown in Fig. 56, the stress distributions show no difference between glass-ceramic sealants in each unit, and the highly stressed glass-ceramic is located between PEN and interconnect. Therefore, the following discussion is focused on the glass-ceramic between PEN and interconnect in the bottom unit cell. The maximum principal stress at room temperature (Fig. 57(a)) is greater than that at operation stage Fig. 57(b). It is attributed to the difference in temperature between stress free condition (800 ^{o}C) and the specific stage (room temperature or operation stage). A greater difference of temperature causes greater thermal stresses. As shown in Fig. 57, a symmetry of stress distribution is observed at room temperature, while that for operation stage is asymmetric. Because of an asymmetry of temperature profile at operation stage (Fig. 58), the region with a greater temperature difference from stress free condition corresponds to the highly stressed region. However, the location of highly stressed region at operation stage is the same as one of the highly stressed regions at room temperature, so a 2D circular interfacial crack with a diameter of 100 μm is placed there to calculate the stress intensity factors and energy release rate.

4.3.2 Energy release rate of glass-ceramic/metallic interconnect joint

Energy balance based on the near-tip fields leads to the following relation between energy release rate and stress intensity factors valid for bimaterials, and the formula is given as [49,51]

$$G = \frac{1-\beta^2}{E'_{\text{int}}}\left(K_I^2 + K_{II}^2\right) + \frac{1}{2\mu'_{\text{int}}} K_{III}^2 \tag{15}$$

where G is energy release rate in a plane strain condition, K_I, K_{II}, and K_{III} are stress intensity factors in Mode I, Mode II, and Mode III, respectively, and E'_{int}, μ'_{int}, and β can be calculated through the following formulas

$$\frac{1}{E'_{\text{int}}} = \frac{1}{2}\left(\frac{1}{E'_1} + \frac{1}{E'_2}\right) \tag{16}$$

$$\frac{1}{\mu'_{\text{int}}} = \frac{1}{2}\left(\frac{1}{\mu'_1} + \frac{1}{\mu'_2}\right) \tag{17}$$

$$\beta = \frac{\mu'_1(\kappa_2 - 1) - \mu'_2(\kappa_1 - 1)}{\mu'_1(\kappa_2 + 1) - \mu'_2(\kappa_1 + 1)} \tag{18}$$

where μ'_i and E'_i are the shear modulus and Young's modulus of each material in a plane strain condition (i = 1, 2), respectively, and κ_i is a function of Poisson's ratio, ν_i , and defined as

$$\kappa_i = 3 - 4\nu_i \tag{19}$$

For an isotropic and homogeneous material, the shear modulus in a plane strain condition is given as

$$\mu'_i = \frac{E'_i}{2(1+\nu_i)} \tag{20}$$

In the present study, because the failure of Mode III is not considered for the four-point bending test, the K_{III} term in Eq. (15) is neglected for calculating the energy release rate. The stress intensity factors K_I and K_{II} determined in the simulation are thus used to calculate the energy release rate for each node at the crack front through Eq. (15). Note there are 400 nodes along the circular crack front. Figure 59(a) shows the calculated energy release rate at various positions of the 100-μm circular crack front at various stages in the given 3-cell SOFC stack model. Note that the position of the circular crack front is represented by the node number at the crack front. As shown in Fig. 59(a), the interfacial fracture energy at room temperature is obviously greater than that at operation stage because of greater stresses at room temperature. If the calculated energy release rate is greater than the interfacial fracture energy determined by experiment, crack is expected to

propagate spontaneously. The interfacial fracture energy determined by experiment in the previous sections is just a critical value for a certain mixity angle (Tables 5 and 8).

Because the temperature at the area where the interfacial crack is placed is around 700 ^{o}C at operation stage, the calculated energy release rate at operation stage is compared with the interfacial fracture energy at 700 ^{o}C in Table 5. As the entire FEA model has a uniform distribution of room temperature after assembling such that the calculated energy release rate at room temperature is compared with the interfacial fracture energy at 25 ^{o}C in Tables 5 and 8. In Fig. 59(a), the calculated energy release rates of mixity angles of 46.5^{o} and 47.5^{o} at room temperature are selected for comparison and listed in Table 13. Note that there are two positions corresponding to each mixity angle. In comparison with the interfacial fracture energy at room temperature (Tables 5 and 8), the interfacial circular crack of 100-μm diameter is expected to propagate spontaneously at room temperature and cause failure of the given pSOFC stack because the calculated energy release rate is greater than the interfacial fracture energy. Table 14 lists the calculated energy release rate at two positions with a mixity angle of 48^{o} at operation stage. Because the calculated energy release rate is much smaller than the interfacial fracture energy at 700 ^{o}C such that the interfacial crack will not extend at the specific crack front position with a mixity angle of 48^{o}.

The given size of interfacial circular crack was gradually reduced to find the critical size such that the calculated energy release rate is less than the experimentally determined interfacial fracture energy at both room and operating temperatures. The strategy is to reduce the diameter of the circular crack, and check whether the calculated energy release rate is smaller than the interfacial fracture energy. Accordingly, it is found that the calculated energy release rate with specific mixity angles is less than the corresponding interfacial fracture energy at both room temperature and operation stage when the crack diameter is reduced to 70 μm and below. Fig. 60(a) shows the calculated energy release rate at various positions of the 70-μm circular crack front at various stages. The locations for two specific mixity angles (46.5^{o} and 47.5^{o}) are determined in Fig. 60(b), and then the corresponding energy release rate is found at these locations in Fig. 60 (a). Note that the variation of mixity angle in Fig. 60(b) at operation stage is not continuous because K_I changes from positive to negative at node numbers of 326-386. As shown in Tables 13 and 14, the calculated energy release rates are all smaller than the interfacial fracture energy for a circular crack of 70-μm diameter. Therefore, the critical interfacial crack size is about 70 μm. Note that the critical size of 70 μm is determined for mixity angles of 46.5^{o}-48^{o}.

5. CONCLUSIONS

(1) Two types of fracture modes were observed in metallic interconnect /glass-ceramic/notched metallic interconnect joints. Firstly, crack initiates at notch, penetrates through the glass-ceramic layer, and propagates along the second interface. Secondly, crack initiates at notch and propagates along first interface, followed by penetration through the glass-ceramic layer and propagation along both the first and second interfaces, simultaneously.

(2) With regard to the effect of aging treatment at 800 ^{o}C for 100 or 1000 h, such aging treatment does not significantly influence the variation trend of interfacial fracture energy of glass-ceramic/interconnect joint with temperature, and there is no obvious change between non-aged and 100 h-aged condition at room temperature to 800 ^{o}C.

(3) The interfacial fracture energy of glass-ceramic/interconnect joint increases with increasing temperature from room temperature to 700 ^{o}C. There is a maximum value at 700 ^{o}C due to a crack bridging phenomenon, while it decreases from 700 ^{o}C to 800 ^{o}C because of softening and flowability of GC-9.

(4) For 1000 h-aged condition, the interfacial fracture energy at 650 ^{o}C is smaller than that of non-aged and 100 h-aged conditions, presumably due to a greater brittleness of crystalline phases. At 700 ^{o}C and 750 ^{o}C, the interfacial fracture energy becomes lager than that of non-aged and 100 h-aged conditions. It may be associated with a difference in the fracture site. At 800 ^{o}C, as the testing temperature is higher than T_s, the interfacial fracture energy for variously aged conditions is comparable.

(5) For non-aged and 100 h-aged glass-ceramic/metallic interconnect joints, crack propagates along the interface between the chromate layer and glass-ceramic substrate when tested at 700 ^{o}C and 750 ^{o}C, while it propagates within the chromate layer at room temperature, 650 ^{o}C, and 800 ^{o}C. For 1000 h-aged joints, crack propagates within the chromate layer at each given temperature.

(6) For non-aged and 100 h-aged PEN/glass-ceramic/notched metallic interconnect, crack propagates along the PEN/glass-ceramic interface only at room temperature. The specimens are fractured by crack penetration through both the glass-ceramic layer and PEN directly at elevated temperatures. The interfacial fracture energy increases after a

100 h-aging treatment.

(7) For non-aged and 100 h-aged PEN/glass-ceramic joints tested at room temperature, crack propagates along the interface between glass-ceramic and PEN and also kinks into the glass-ceramic layer.

(8) The calculated energy release rate for an interfacial circular crack of 70-μm diameter placed at the highly stressed region in a prototypical pSOFC stack is smaller than the corresponding interfacial fracture energy determined experimentally at the specific mixity angles of 46.5^{o}-48^{o} for the joint of GC-9/Crofer 22 H. The critical interfacial crack or defect size in the GC-9/Crofer 22 H joint of the given pSOFC stack is accordingly defined as 70 μm.

REFERENCES

1. A. Choundhury, H. Chandra, and A. Arora, "Application of Solid Oxide Fuel Cell Technology for Power Generation-A Review," *Renewable and Sustainable Energy Reviews*, Vol. 20, pp. 430-442, 2013.

2. J. Fergus, R. Hui, X. Li, D. P. Wilkinson, and J. Zhang, *Solid Oxide Fuel Cells: Materials Properties and Performance*, CRC Press, New York, USA, 2008.

3. J. Malzbender, J. Mönch, R. W. Steinbrech, T. Koppitz, S. M. Gross, and J. Remmel, "Symmetric Shear Test of Glass-Ceramic Sealants at SOFC Operation Temperature," *Journal of Materials Science*, Vol. 42, pp. 6297-6301, 2007.

4. J. W. Fergus, "Sealants for Solid Oxide Fuel Cells," *Journal of Power Sources*, Vol. 147, pp. 46-57, 2005.

5. W. Z. Zhu and S. C. Deevi, "A Review on the Status of Anode Materials for Solid Oxide Fuel Cells," *Materials Science and Engineering*, Vol. A362, pp. 228-239, 2003.

6. T. L. Wen, D. Wang, M. Chen, H. Tu, Z. Lu, Z. Zhang, H. Nie, and W. Huang, "Material Research for Planar SOFC Stack," *Solid State Ionics*, Vol. 148, pp. 513-519, 2002.

7. Y. Zhao, J. Malzbender, and S. M. Gross, "The Effect of Room Temperature and High Temperature Exposure on the Elastic Modulus, Hardness and Fracture Toughness of Glass Ceramic Sealants for Solid Oxide Fuel Cells," *Journal of the European Ceramic Society*, Vol 31, pp. 541-548, 2011.

8. P. A. Lessing, "A Review of sealing Technologies Applicable to Solid Oxide Electrolysis Cells," *Journal of Materials Science*, Vol. 42, pp. 3465-3476, 2007.

9. W. Liu, X. Sun, and M. A. Khaleel, "Predicting Young's Modulus of Glass/Ceramic Sealant for Solid Oxide Fuel Cell Considering the Combined Effects of Aging, Micro-Voids and Self-Healing," *Journal of Power Sources*, Vol. 185, pp. 1193-1200, 2008.

10. H.-T. Chang, "High-Temperature Mechanical Properties of a Glass Sealant for Solid Oxide Fuel Cell," Ph.D. Thesis, National Central University, 2010.

11. W. Xu, X. Sun, E. Stephens, I. Mastorakos, M. A. Khaleel, and H.Zbib, "A Mechanistic-Based Healing Model for Self-Healing Glass Seals Used

in Solid Oxide Fuel Cells," *Journal of Power Sources*, Vol. 218, pp. 445-454, 2012.

12. W. N. Liu, X. Sun, and M. A. Khaleel, "Study of Geometric Stability and Structural Integrity of Self-Healing Glass Seal System Used in Solid Oxide Fuel Cells," *Journal of Power Sources*, Vol. 196, pp. 1750-1761, 2011.

13. S. R. Choi and N. P. Bansal, "Mechanical Properties of SOFC Seal Glass Composites," *Ceramic Engineering and Science Proceedings*, Vol. 26, pp. 275-283, 2005.

14 V. A. Haanappel, V. Shemet, I. C. Vinke, and W. J. Quadakkers, "A Novel Method to Evaluate the Suitability of Glass Sealant-Alloy Combinations under SOFC Stack Conditions," *Journal of Power Sources*, Vol. 141, pp. 102-107, 2005.

15. P. Batfalsky, V. A. C. Haanappel, J. Malzbender, N. H. Menzler, V. Shemet, I. C. Vinke, and R. W. Steinbrech, "Chemical Interaction Between Glass-Ceramic Sealants and Interconnect Steels in SOFC Stacks," *Journal of Power Sources*, Vol. 155, pp. 128-137, 2006.

16. S. Ghosh, A. D. Sharma, P. Kundu, and R. N. Basuz, "Glass-Ceramic Sealants for Planar IT-SOFC: A Bilayered Approach for Joining Electrolyte and Metallic Interconnect," *Journal of the Electrochemical Society*, Vol. 155, pp. 473-478, 2008.

17. K. S. Weil, J. E. Deibler, J. S. Hardy, D. S. Kim, G.-G. Xia, L. A. Chick, and C. A. Coyle, "Rupture Testing as a Tool for Developing Planar Solid Oxide Fuel Cell Seals," *Journal of Materials Engineering and Performance*, Vol. 13, pp. 316-326, 2004.

18. J. Milhans, M. Khaleel, X. Sun, M. Tehrani, M. Al-Haik, and H. Garmestani, "Creep Properties of Solid Oxide Fuel Cell Glass-Ceramic Seal G18," *Journal of Power Sources*, Vol, 195, pp. 3631-3635, 2010.

19. Y.-S. Chou, J. W. Stevenson, and P. Singh, "Effect of Pre-Oxidation and Environmental Aging on the Seal Strength of a Novel High-Temperature Solid Oxide Fuel Cell (SOFC) Sealing Glass with Metallic Interconnect," *Journal of Power Sources*, Vol. 184, pp. 238-244, 2008.

20. E. V. Stephens, J. S. Vetrano, B. J. Koeppel, Y. Chou, X. Sun, and M. A. Khaleel, "Experimental Characterization of Glass-Ceramic Seal Properties and Their Constitutive Implementation in Solid Oxide Fuel Cell Stack Models," *Journal of Power Sources*, Vol. 193, pp. 625-631, 2009.

21. C.-K. Lin, T.-T. Chen, Y.-P. Chyou, and L.-K. Chiang, “Thermal Stress Analysis of a Planar SOFC Stack,” *Journal of Power Sources*, Vol. 164, pp. 238-251, 2007.

22. A.-S. Chen, “Thermal Stress Analysis of a Planar SOFC Stack with Mica Sealants,” M.S. Thesis, National Central University, 2007.

23. C.-K. Lin, L.-H. Huang, L.-K. Chiang, and Y.-P. Chyou, “Thermal Stress Analysis of a Planar Solid Oxide Fuel Cell Stacks: Effects of Sealing Design,” *Journal of Power Sources*, Vol. 192, pp. 515-524, 2009.

24. J. Malzbender and Y. Zhao, “Micromechanical Testing of Glass–Ceramic Sealants for Solid Oxide Fuel Cells,” *Journal of Materials Science*, Vol. 47, pp. 4342-4347, 2012.

25. K. S. Weil, J. E. Deibler, J. S. Hardy, D. S. Kim, G.-G. Xia, L. A. Chick, and C. A. Coyle, “Rupture Testing as a Tool for Developing Planar Solid Oxide Fuel Cell Seals,” *Journal of Materials Engineering and Performance*, Vol. 13, pp. 316-326, 2004.

26. E. V. Stephens, J. S. Vetrano, B. J. Koeppel, Y. Chou, X. Sun, and M. A. Khaleel, “Experimental Characterization of Glass-Ceramic Seal Properties and their Constitutive Implementation in Solid Oxide Fuel Cell Stack Models,” *Journal of Power Sources*, Vol. 193, pp. 625-631, 2009.

27. J.-Y. Chen, “Analysis of Mechanical Properties for the Joint of Metallic Interconnect and Glass Ceramic in Solid Oxide Fuel Cell,” M.S. Thesis, National Central University, 2010.

28. J.-H. Yeh, “Analysis of High-Temperature Mechanical Durability for the Joint of Glass Ceramic Sealant and Metallic Interconnect for Solid Oxide Fuel Cell,” M.S. Thesis, National Central University, 2011.

29. J. Malzbender, R. W. Steinbrech, and L. Singheiser, “Determination of the Interfacial Fracture Energies of Cathodes and Glass Ceramic Sealants in a Planar Solid-Oxide Fuel Cell Design,” *Materials Research Society*, Vol. 18, pp. 929-934, 2003.

30. X. Sun, W. N. Stephens, and M. A. Khaleel, “Determination of Interfacial Adhesion Strength Between Oxide Scale and Substrate for Metallic SOFC Interconnects,” *Materials Research Society*, Vol. 176, pp. 167-176, 2008.

31. K. Hbaieb, “Measurement of Fracture Toughness of Anode Used in Solid Oxide Fuel Cell,” *Thin Solid Films*, Vol. 517, pp. 4892-4894, 2009.

32. A. N. Kumar and B. F. Sørensen, “Fracture Energy and Crack Growth in Surface Treated Yttria Stabilized Zirconia for SOFC Applications,” *Materials Science and Engineering*, Vol. A333, pp. 380-389, 2001.

33. J. Johnson and J. Qu, “Three-Dimensional Numerical Simulation Tools for Fracture Analysis in Planar Solid Oxide Fuel Cells (SOFCs),” pp. 393-405 in *Proceedings of the 30th International Conference on Advanced Ceramics and Composites*, Cocoa Beach, Florida, January 22-27, 2006.

34. B. N. Nguyen, B. J. Koeppel, S. Ahzi, M. A. Khaleel, and P. Singh, “Crack Growth in Solid Oxide Fuel Cell Materialas: From Discrete to Continuum Modeling,” *Journal of the American Ceramic Society*, Vol. 89, pp. 1358-1368, 2006.

35. S. J. Howard, A. J. Phillipps, and T. W. Clyne, “The Interpretation of Data From the Four-Point Bend Delamination Test to Measure Interfacial Fracture Toughness,” *Composites*, Vol. 24, pp. 103-112, 1993.

36. P. G. Charalambides, J. Lund, A. G. Evans, and R. M. McMeeking, “A Test Specimen for Determining the Fracture Resistance of Bimaterial Interfaces,” *Journal of Applied Mechanics*, Vol. 56, pp. 77-82, 1989.

37. L. R. Katipelli, A. Agarwal, and N. B. Dahotre, “Interfacial Strength of Laser Surface Engineered TiC Coating on 6061 Al Using Four-Point Bend Test,” *Materials Science and Engineering*, Vol. A289, pp. 34-40, 2000.

38. H. Hirakata, T. Yamada, Y. Nobuhara, A. Yonezu, and K. Minoshima, “Hydrogen Effect on Fracture Toughness of Thin Film/Substrate Interfaces,” *Engineering Fracture Mechanics*, Vol. 77, pp. 803-818, 2010.

39. L. Zou, Y. Huang, and C. Wang, “The Characterization and Measurement of Interfacial Toughness for Si_3N_4/BN Composites by the Four-Point Bend Test,” *Journal of the European Ceramic Society*, Vol. 24, pp. 2861-2868, 2004.

40. “Continuum Elements,” Chapter 27 in *ABAQUS 6.11-1 Analysis User’s Manual*, *Vol. IV*, ABAQUS, Inc., Providence, RI, USA, 2011.

41. “Special-Purpose Techniques,” Chapter 11 in *ABAQUS 6.11-1 Analysis User’s Manual*, *Vol. IV*, ABAQUS, Inc., Providence, RI, USA, 2011.

42. Y.-T. Chiu, “Creep and Thermo-Mechanical Fatigue Properties of Ferritic Stainless Steels for Use in Solid Oxide Fuel Cell Interconnect,” Ph.D. Thesis, National Central University, 2012.

43. Metals Handbook, 10th Ed., Vol. 2, *ASM International*, Materials Park, OH, 1990, pp. 437-441.

44. W. Koster, "The Temperature Dependence of the Elasticity Modulus of Pure Metals," *Zeitschrift fur Metallkunde*, Vol. 39, 1948, pp. 1-9. (in German)

45. Material Data Sheet No. 4050: Crofer 22 H, http://www.thyssenkruppvdm.com/en/downloads/data-sheets/?no cache=1 (accessed 11.10.12).

46. T.-T. Chen, "Thermal Stress Analysis of a Planar SOFC Stack," M.S. Thesis, National Central University, 2006.

47. Y.-P. Chyou, T.-D. Chung, J.-S. Chen, and R.-F. Shie, "Integrated Thermal Engineering Analyses with Heat Transfer at Periphery of Planar Solid Oxide Fuel Cell," *Journal of Power Sources*, Vol. 139, 2005, pp. 126-140.

48. V. T. Do, H. Hirakata, T. Kitamura, V. T. Vuong, and V. L. Le, "Evaluation of Interfacial Toughness Curve of Bimaterial in Submicron Scale," *International Journal of Solids and Structures*, Vol. 49, pp. 1676-1684, 2012.

49. "Fracture Mechanics," Chapter 31 in *ABAQUS 6.11-1 User's Manual, Vol. IV*, ABAQUS, Inc., Providence, RI, USA, 2011.

50. H. C. Cao and A. G. Evans, "An Experimental Study of the Fracture Resistance of Bimaterial Interfaces," *Mechanics of Materials*, Vol. 7, pp. 295-304, 1989.

51. G. Delette, J. Laurencin, S. Murer, and D. Leguillon, "Effect of Residual Stresses on the Propagation of Interface Cracks Between Dissimilar Brittle Materials: Contribution of Two and Three-Dimensional Analyses," *European Journal of Mechanics A/Solids*, Vol. 35, pp. 97-110, 2012.

Table 1 Elastic properties of PEN [25]

Temperature (^{o}C)	Poisson's ratio	Elastic modulus (GPa)
25	0.32	120
100	0.32	116
200	0.32	110
300	0.32	105
400	0.32	99
500	0.32	94
600	0.32	89
700	0.32	83
800	0.32	78
850	0.32	75

Table 2 Tensile properties of Crofer 22 H [42]

Temperature (^{o}C)	Poisson's ratio	Elastic modulus (GPa)	Yield strength (MPa)	Tensile strength (MPa)
25	0.3	205	406	567
300	0.3	186	375	522
400	0.3	185	364	499
500	0.3	183	343	451
600	0.3	181	286	359
650	0.3	161	241	295
700	0.3	142	204	219
750	0.3	88	140	147
800	0.3	86	120	123

Table 3 Young's modulus for variously aged GC-9 glass at different temperatures [28]

		Temperature				
	Aged condition	25 °C	650 °C	700 °C	750 °C	800 °C
Young's modulus (GPa)	Non-aged	18	19	9.4	4.9	2.1
	100 h-aged	19	24	31	17	6.5
	1000 h-aged	16	21	22	15	6

Table 4 Elastic properties of nickel mesh [43,44]

Temperature (°C)	Poisson's ratio	Elastic modulus (GPa)
25	0.3	9.9
800	0.3	7.1

Table 5 Fracture resistance of non-aged metallic interconnect/glass-ceramic /notched metallic interconnect at various temperatures

Temperature (°C)	25	650	700	750	800	
Location of interfacial crack	Second interface	Second interface	Second interface	Second interface	First interface	second interface
Average interfacial fracture energy, G_{int}, (J/m^2)	3.01±0.22	46.27±2.02	55.53±3.06	42.97±1.32	34.15±2.60	29.98±2.22
Average critical stress intensity factor, K_{int}, (MPa m$^{0.5}$)	0.33±0.01	1.31±0.03	1.04±0.03	0.66±0.01	0.39±0.02	0.37±0.01
Mixity angle (°)	47.46	46.72	48.04	48.33	-32.14	48.86

Table 6 Fracture resistance of 100 h-aged metallic interconnect/glass-ceramic /notched metallic interconnect at various temperatures

Temperature (^{o}C)	25	650	700	750	800
Location of interfacial crack	Second interface	Second interface	Second interface	Second interface	Second interface
Average interfacial fracture energy, G_{int}, (J/m^2)	2.93±0.19	44.38±10.55	54.69±1.48	39.02±2.77	29.63±1.05
Average critical stress intensity factor, K_{int}, (MPa m$^{0.5}$)	0.33±0.01	1.42±0.17	1.75±0.02	1.10±0.04	0.63±0.01
Mixity angle (^{o})	47.33	46.05	44.81	45.23	47.78

Table 7 Fracture resistance of 1000 h-aged metallic interconnect/glass-ceramic /notched metallic interconnect at various temperatures

Temperature (^{o}C)	25	650	700	750	800
Location of interfacial crack	Second interface	Second interface	Second interface	Second interface	Second interface
Average interfacial fracture energy, G_{int}, (J/m^2)	3.07±0.26	33.80±5.14	62.01±3.14	55.99±0.70	36.94±2.28
Average critical stress intensity factor, K_{int}, (MPa m$^{0.5}$)	0.32±0.01	1.17±0.09	1.61±0.04	1.26±0.01	0.67±0.02
Mixity angle (^{o})	47.72	46.44	45.93	45.63	47.94

Table 8 Fracture resistance of metallic interconnect/glass-ceramic/notched PEN at room temperature

Average interfacial fracture energy, G_{int}, (J/m^2)	Average critical stress intensity factor, K_{int}, (MPa m$^{0.5}$)	Mixity angle (^{o})
1.70±0.21	0.25±0.02	46.43

Table 9 Chemical composition of elements detected in Fig. 43(a)

Element	O	Al	Si	Ba	Cr	Mn
Weight percent (%)	21.34	3.78	15.19	36.72	19.93	3.03

Table 10 Chemical composition of elements detected in Fig. 43(b)

Element	O	Al	Si	Ba	Cr
Weight percent (%)	19.71	4.62	5.15	66.12	4.4

Table 11 Fracture site of non-aged, 100 h-aged, and 1000 h-aged metallic interconnect /glass-ceramic/notched metallic interconnect

	25 ^{o}C	650 ^{o}C	700 ^{o}C	750 ^{o}C	800 ^{o}C
Non-aged	A	A	B	B	A
100 h-aged	A	A	B	B	A
1000 h-aged	A	A	A	A	A

*A: within the chromate layer; B: at the interface between GC-9 and chromate layer.

Table 12 Fracture resistance of PEN/glass-ceramic/notched metallic interconnect tested at room temperature

Aged condition	Average interfacial fracture energy, G_{int}, (J/m^2)	Average critical stress intensity factor, K_{int}, (MPa m$^{0.5}$)	Mixity angle (^{o})
Non-aged	0.75±0.24	0.16±0.03	39.33
100 h-aged	5.48±0.79	0.46±0.03	39.48

Table 13 Calculated energy release rate at selected positions in 100-μm and 70-μm interfacial crack front of glass-ceramic/metallic interconnect joint at room temperature

Interfacial crack size (μm)	Mixity angle (^{o})	Energy release rate (J/m^2)	
100	46.4	6.08	7.37
	47.5	6.26	7.53
70	46.4	1.1	1.12
	47.5	1.15	1.18

Table 14 Calculated energy release rate at selected positions in 100-μm and 70-μm interfacial crack front of glass-ceramic/metallic interconnect joint at operation stage

Interfacial crack size (μm)	Mixity angle (^{o})	Energy release rate (J/m^2)	
100	48	0.15	0.16
70	48	0.03	0.04

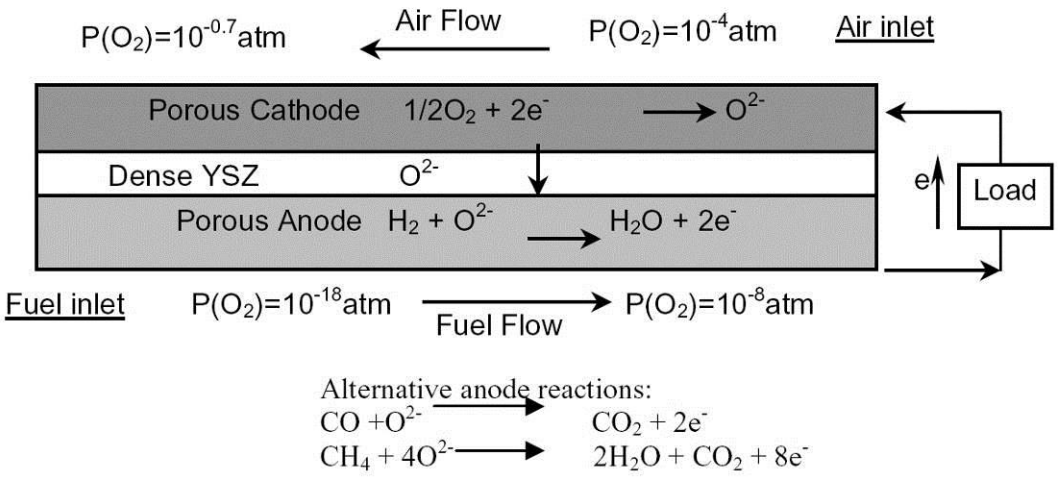

Fig. 1 Operating principle of a single SOFC unit using hydrogen as fuel. [5]

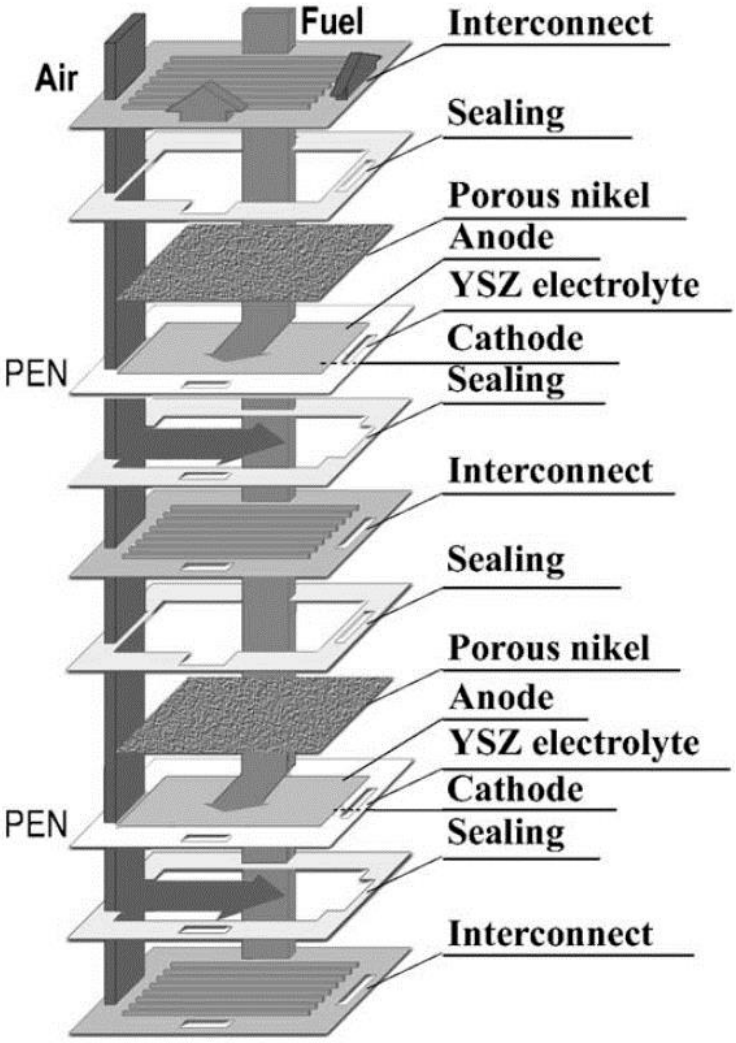

Fig. 2 Structural scheme of a planar SOFC stack. [6]

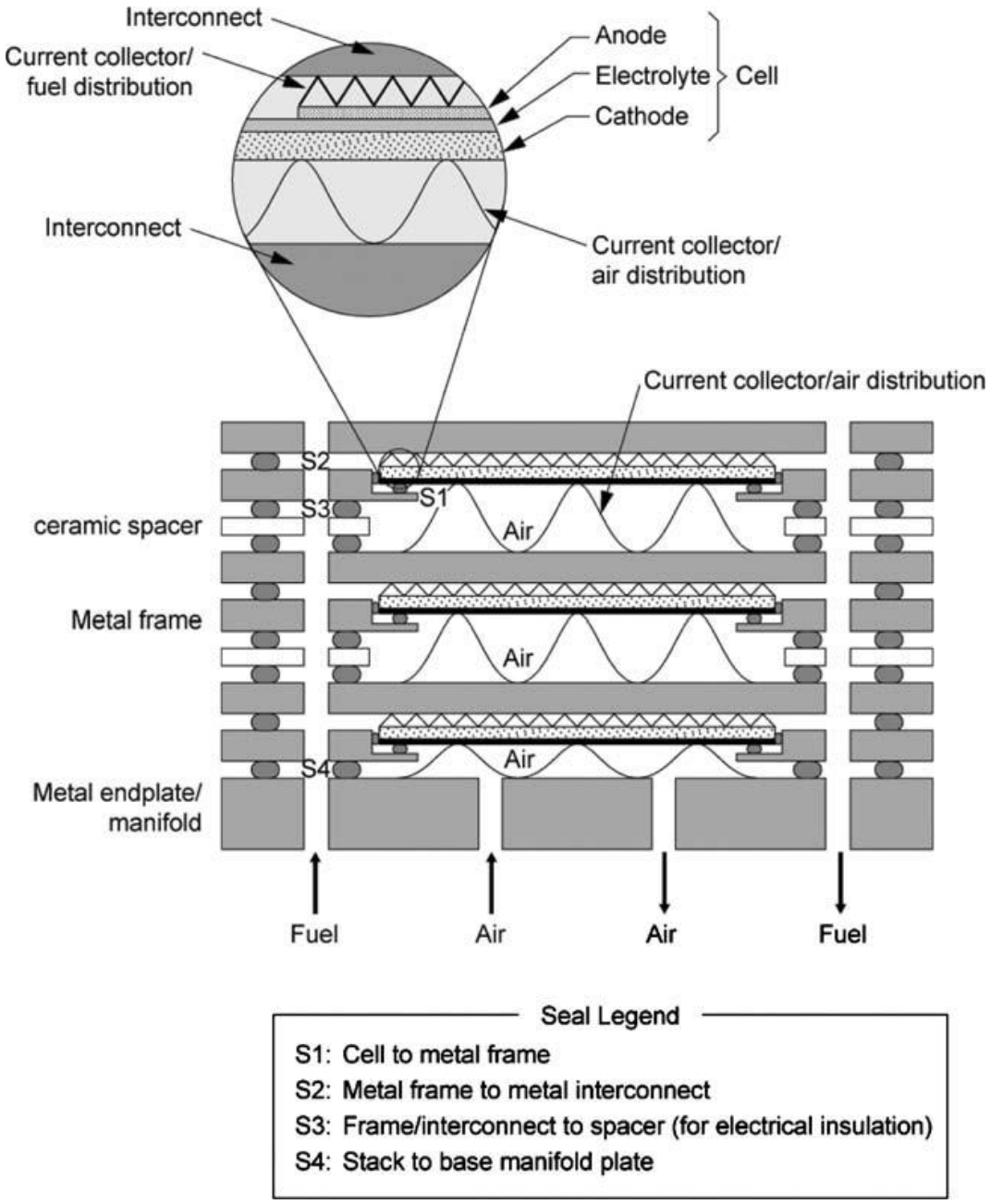

Fig. 3 Scheme of seals used in a planar SOFC stack with metallic interconnects and metallic internal gas manifold channels. [8]

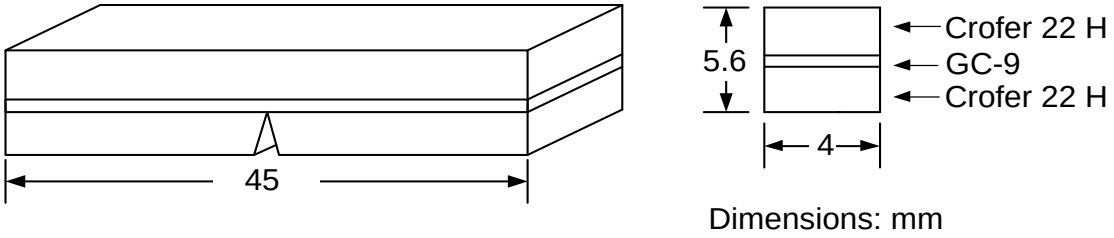

(a)

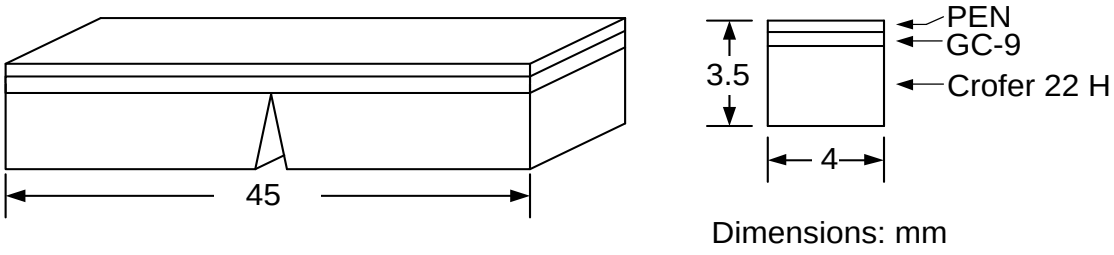

(b)

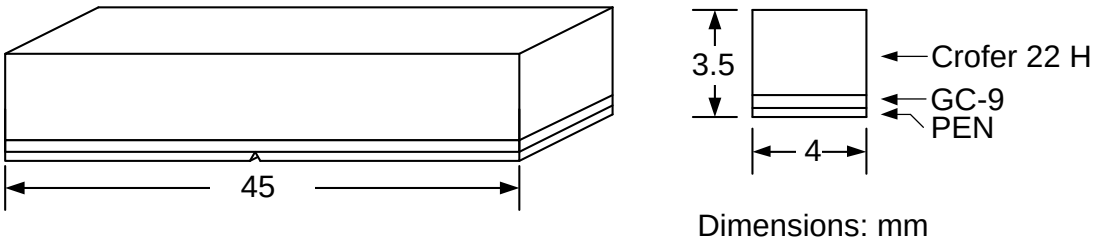

(c)

Fig. 4 Geometry of three types of four-point bending test specimens: (a) metallic interconnect/glass-ceramic/notched metallic interconnect; (b) PEN/glass-ceramic/notched metallic interconnect; (c) metallic interconnect/glass-ceramic/notched PEN.

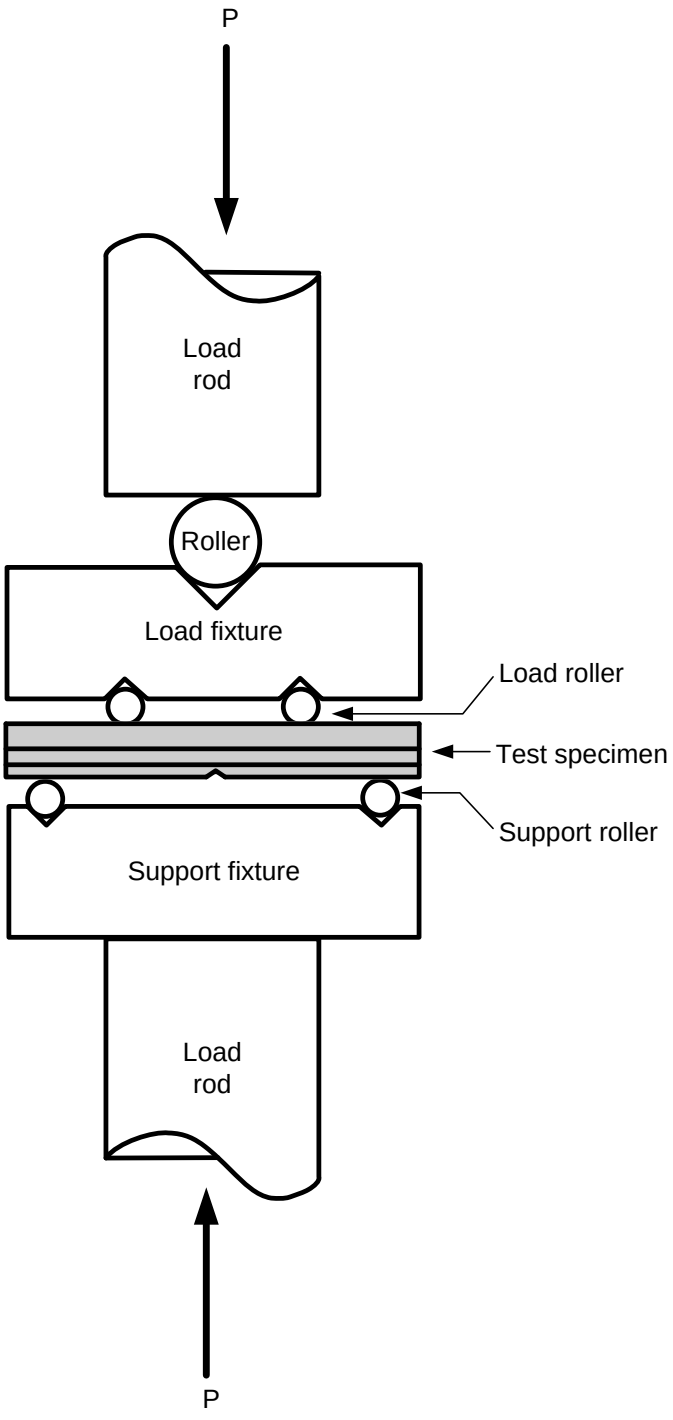

Fig. 5 Schematic of four-point bending test fixture.

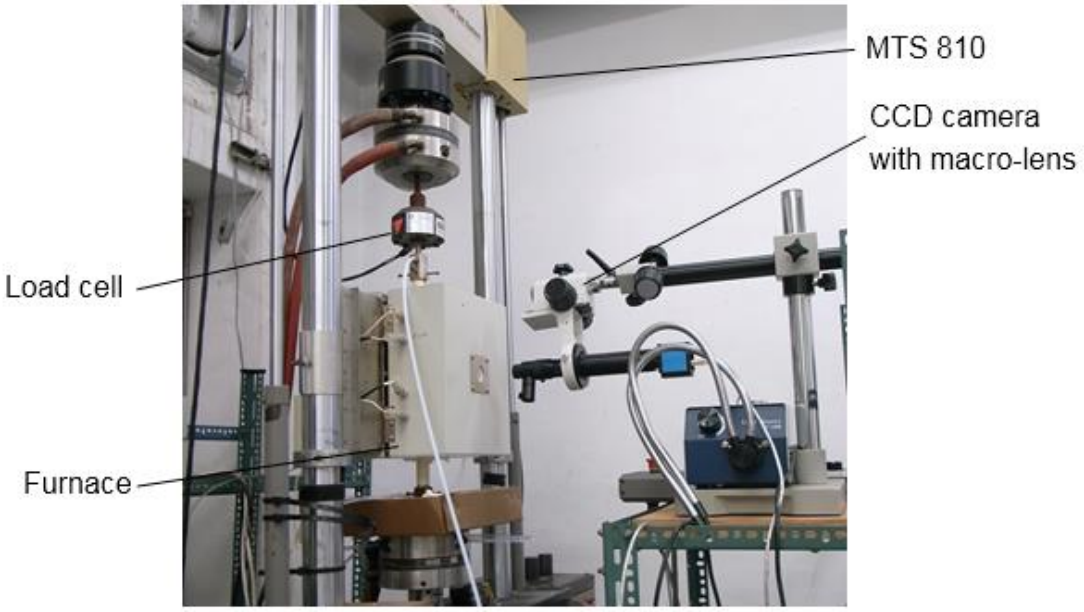

(a)

(b)

Fig. 6 Photographs of experimental set-up for four-point bending tests: (a) overall set-up; (b) cracking observation set-up.

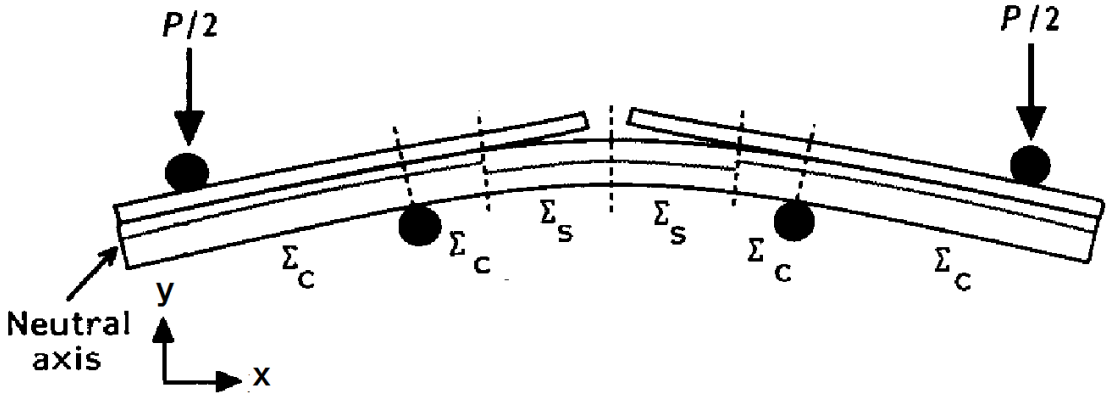

Fig. 7 A four point bending specimen with symmetrical interface cracks. [35]

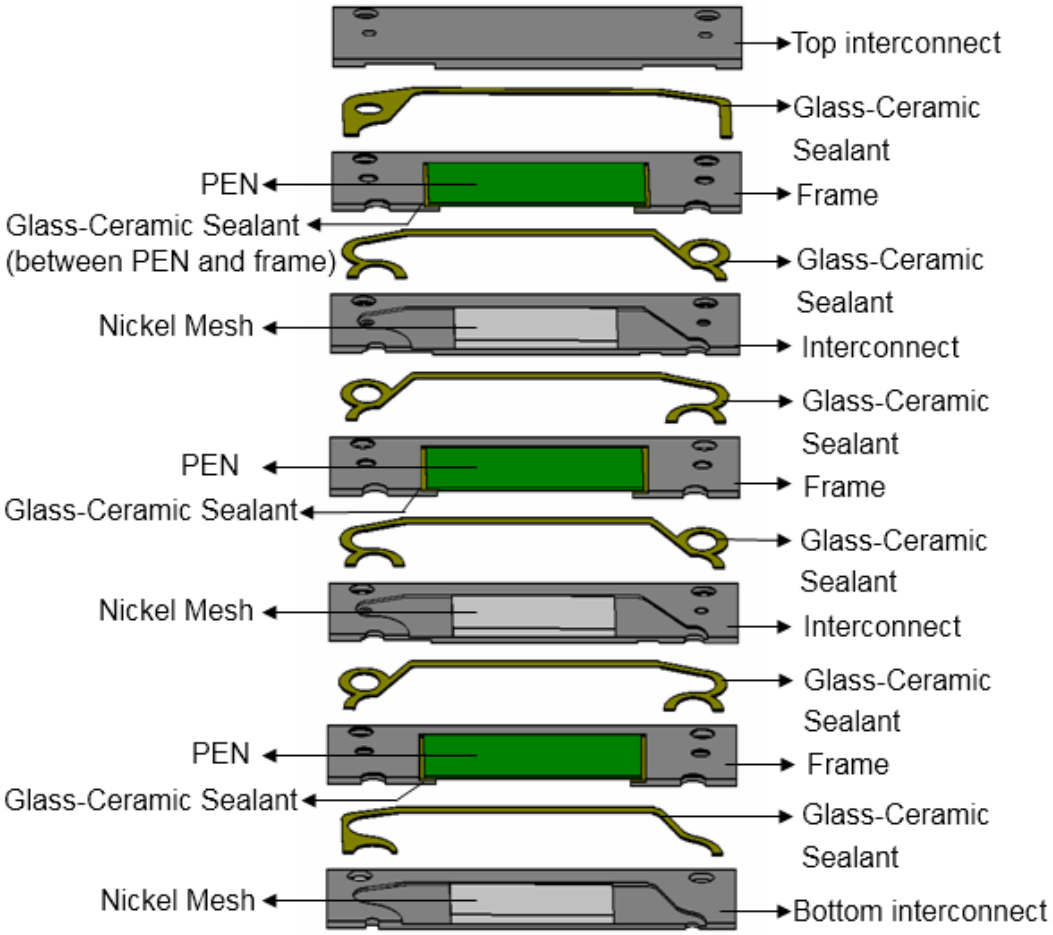

Fig. 8 Schematic of a planar SOFC stack consisting of three unit cells.

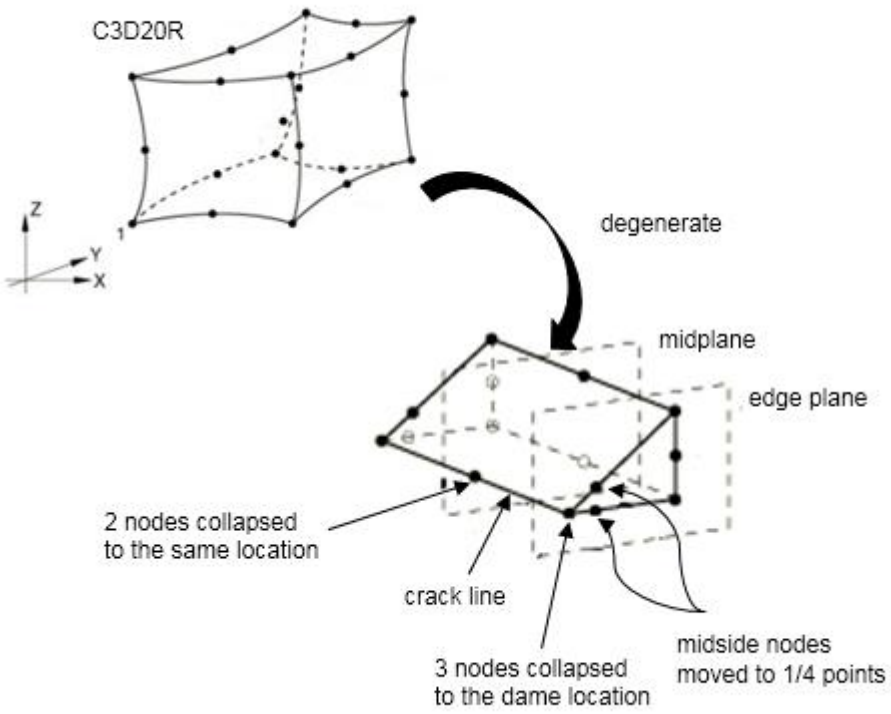

Fig. 9 A 3D collapsed element. [41]

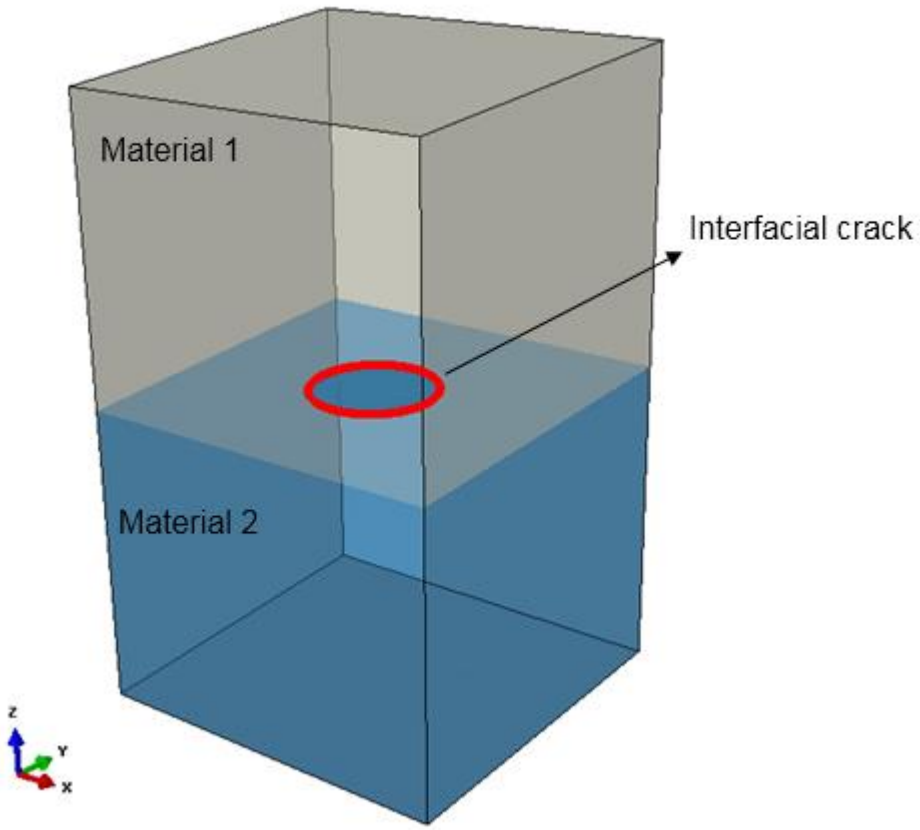

Fig. 10 The local region where an interfacial circular crack is located.

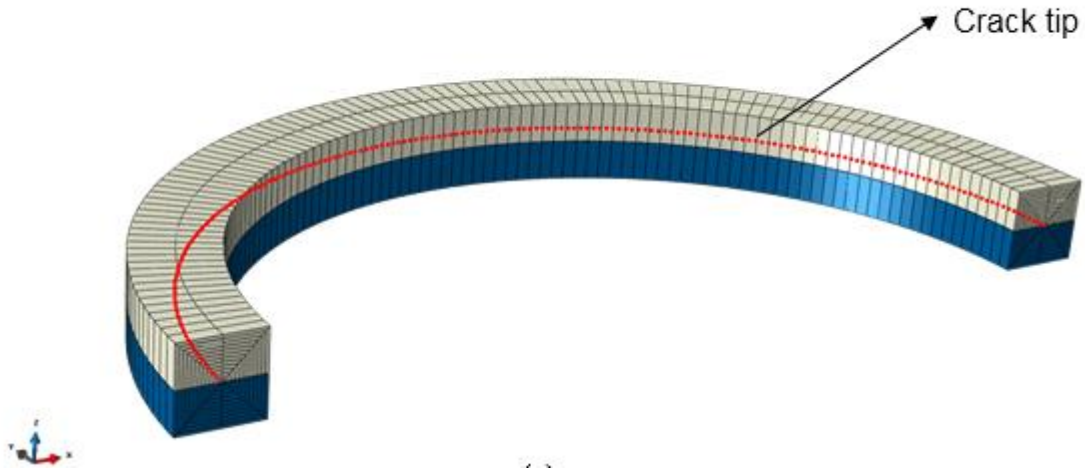

(a)

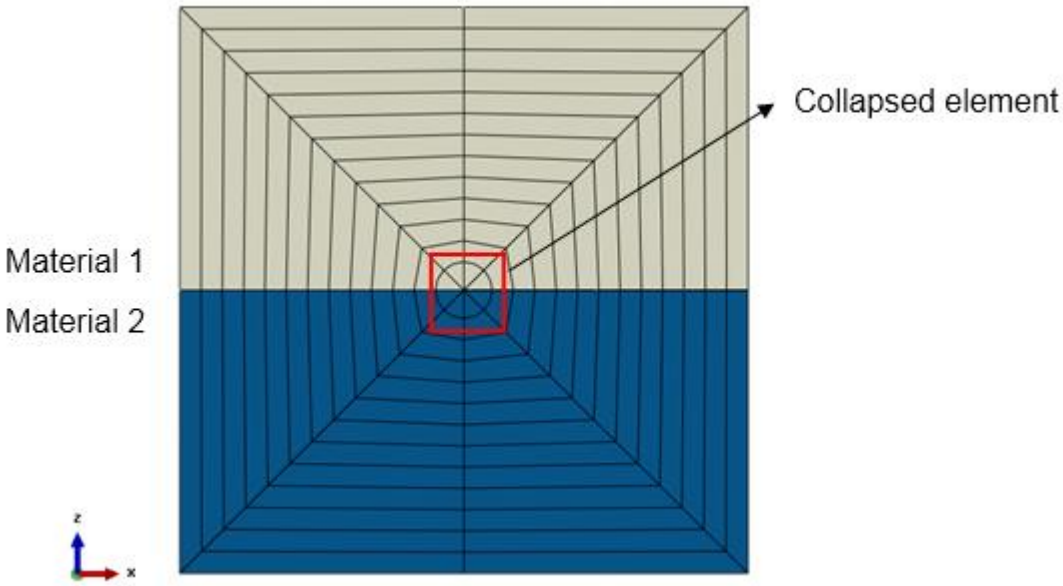

(b)

Fig. 11 Mesh configuration around a circular crack tip: (a) 3D mesh configuration; (b) detail of focused mesh.

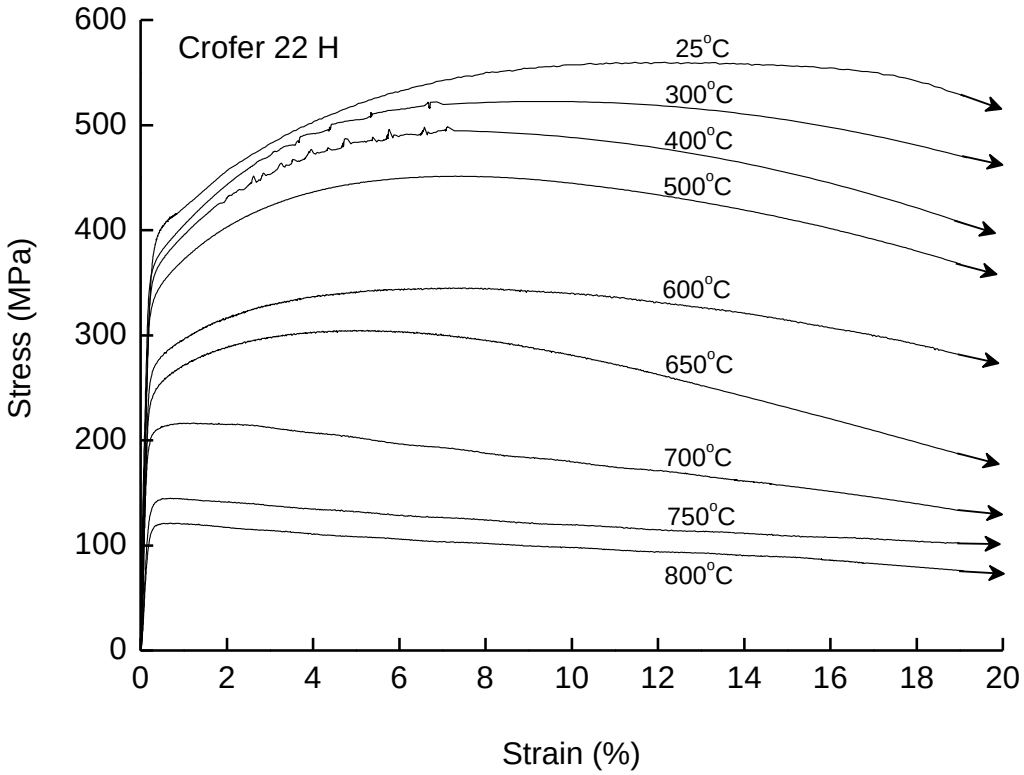

Fig. 12 Engineering stress-strain curves of Crofer 22 H at different temperatures. [42]

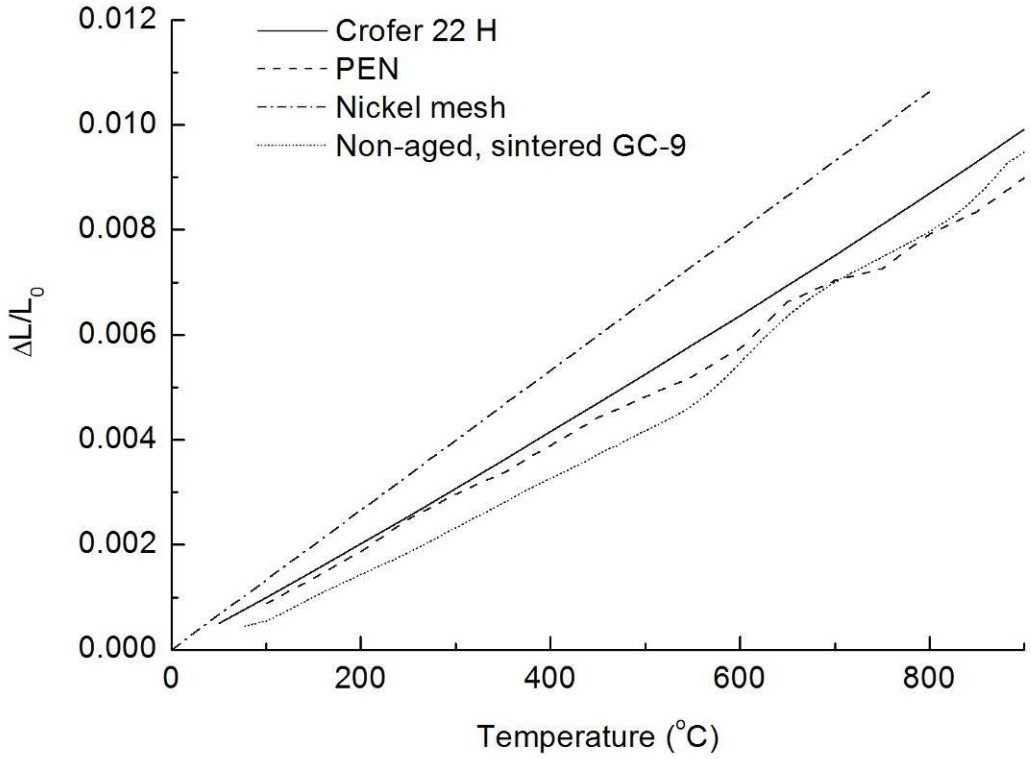

Fig. 13 Thermal expansion behavior of planar SOFC components. [10,43,45,46]

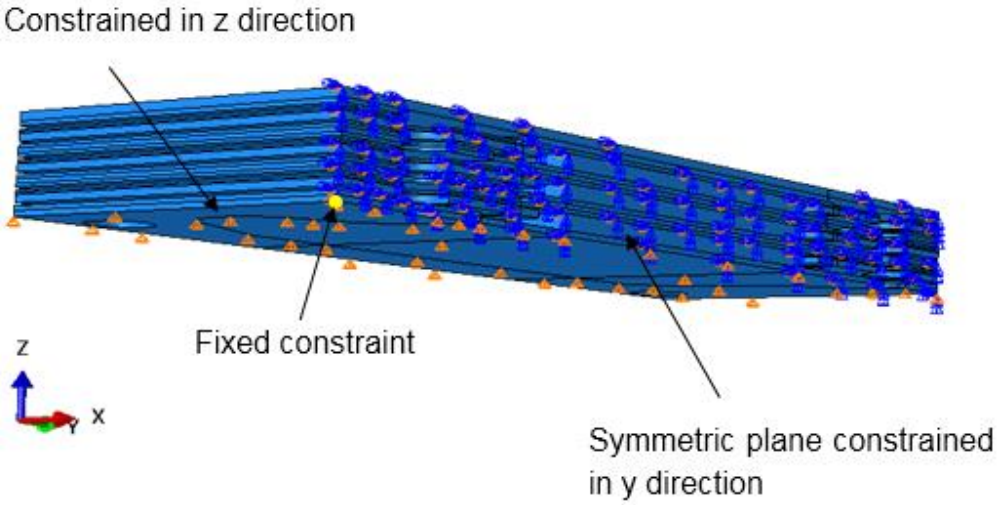

Fig. 14 Boundary conditions applied in the FEA model.

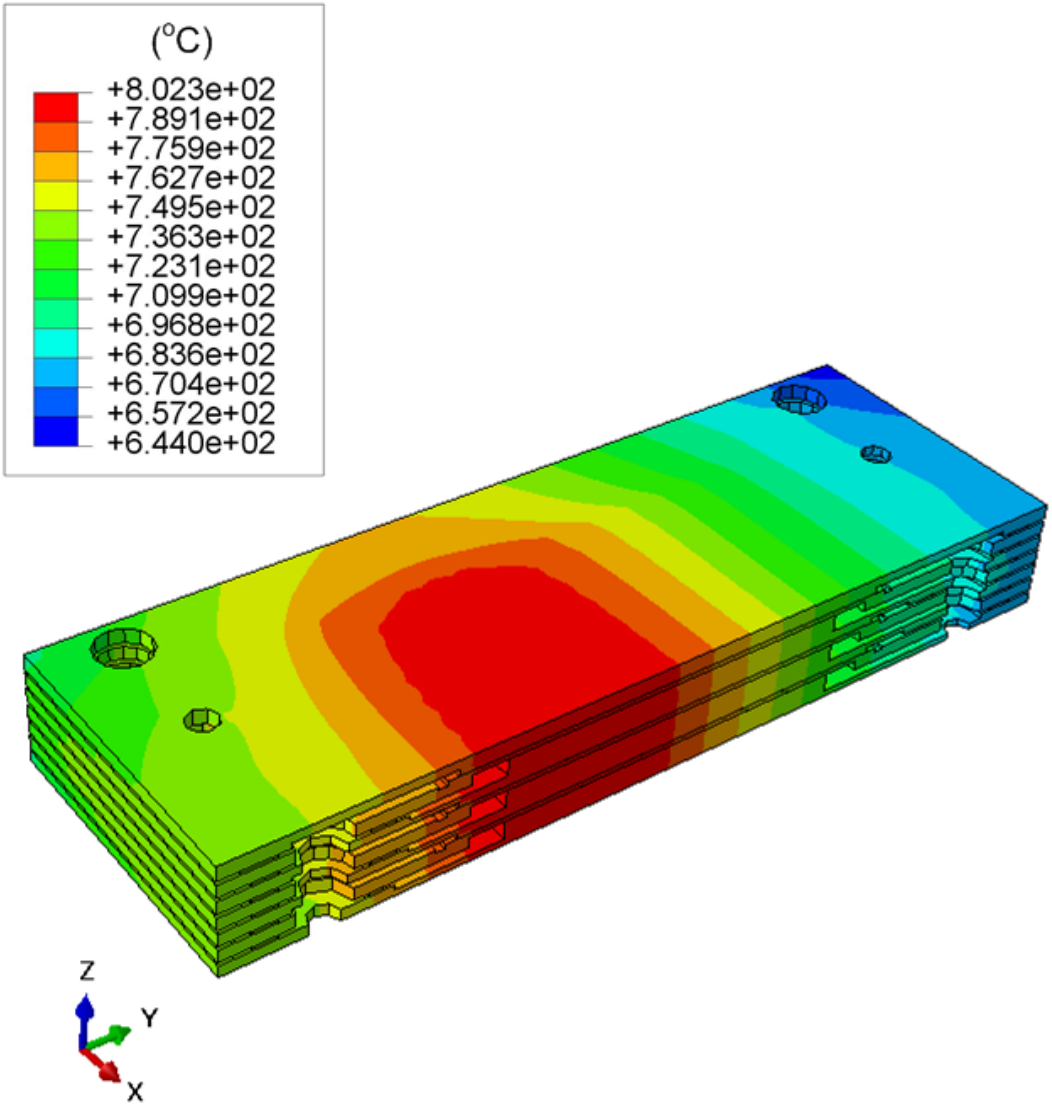

Fig. 15 Temperature profile at operation stage in a 3-cell planar SOFC stack model.

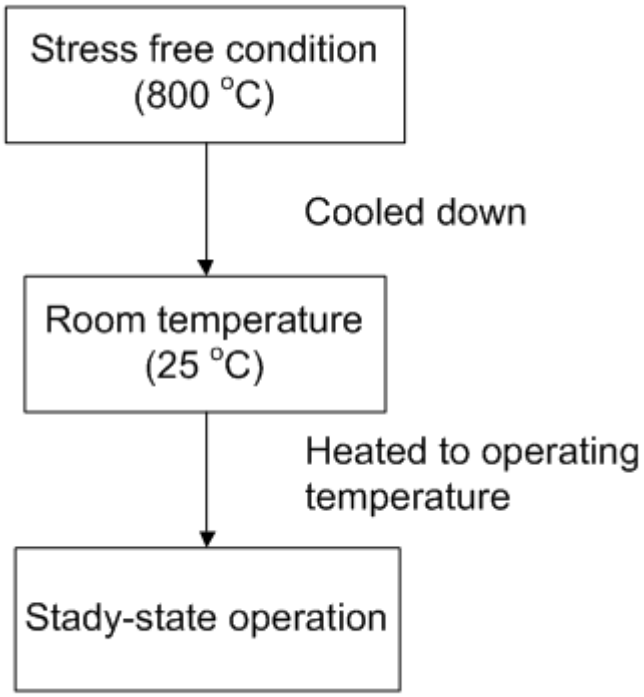

Fig. 16 Analysis procedure for a prototypical planar SOFC.

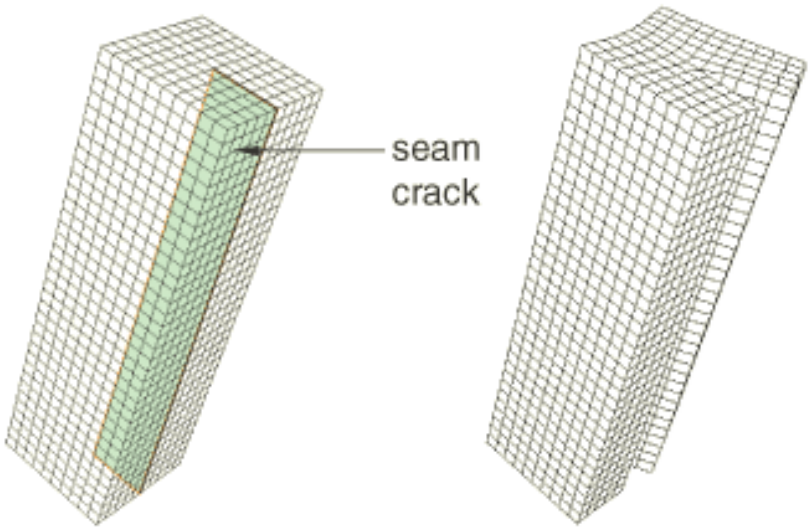

Fig. 17 A face seam embedded in a cell. [49]

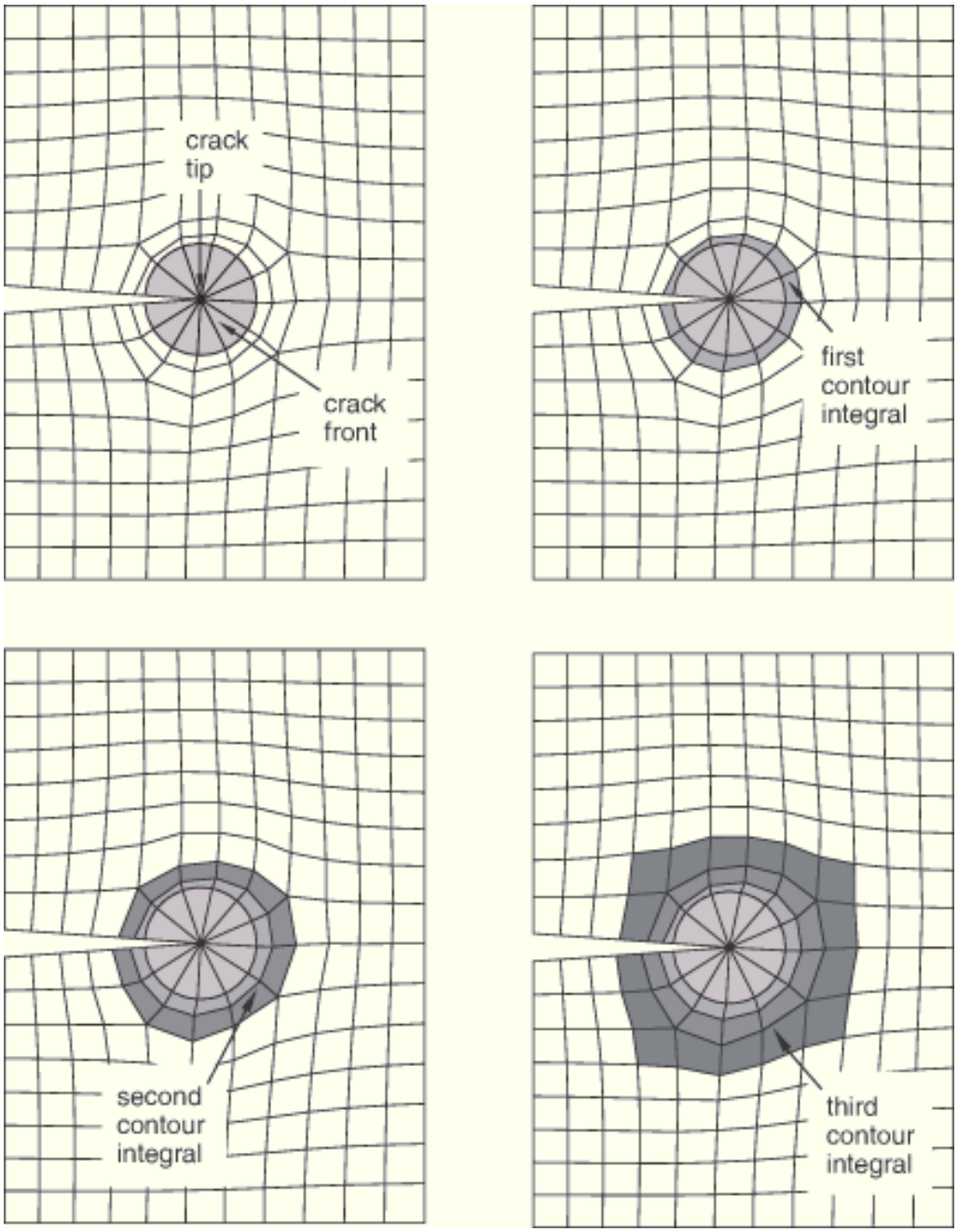

Fig. 18 Contours of material surrounding a crack tip in 2D model. [49]

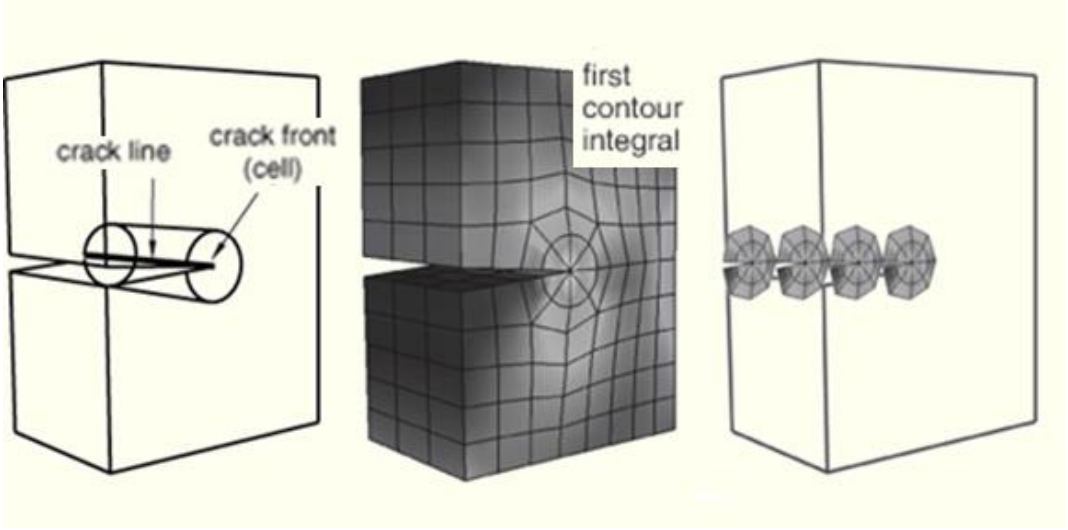

Fig. 19 Contours of material surrounding a crack tip (3D). [49]

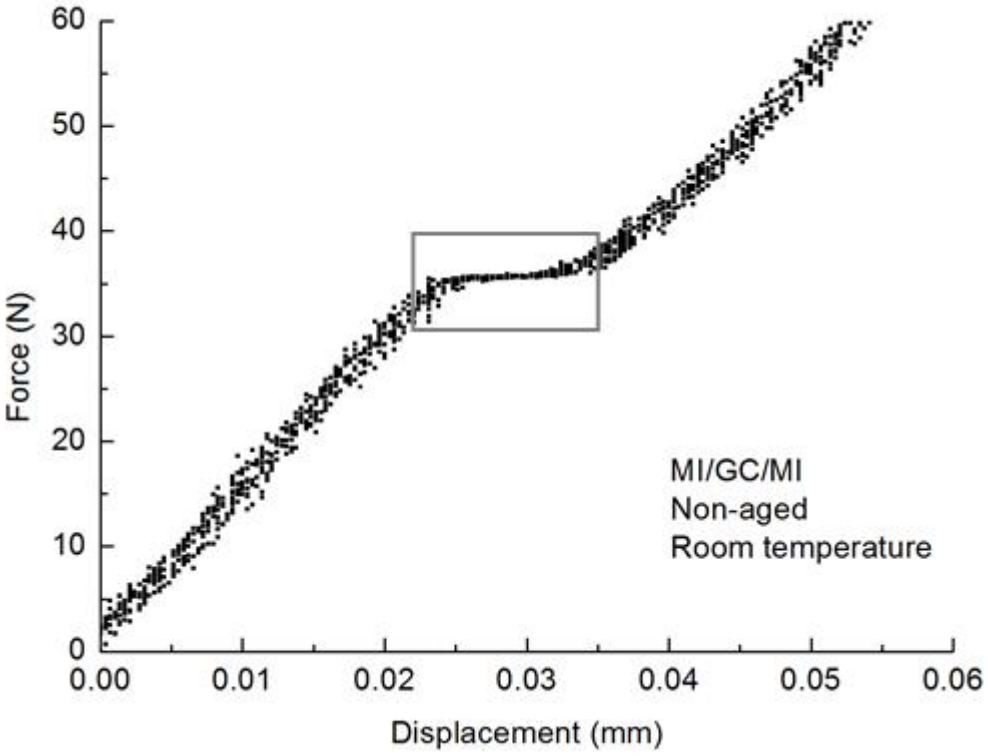

(a)

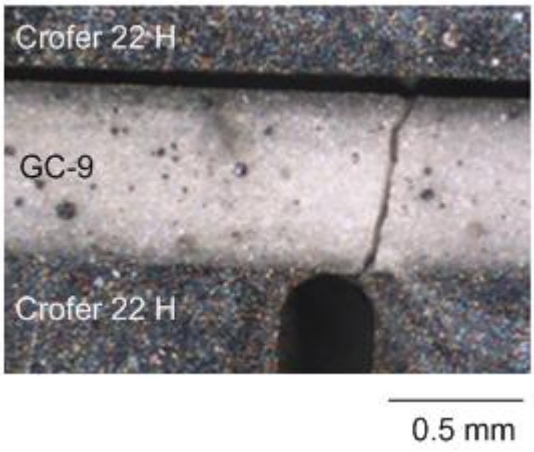

(b)

Fig. 20 Representative results of non-aged metallic interconnect/glass-ceramic/notched metallic interconnect joint tested at room temperature: (a) load-displacement relationship; (b) side view of specimen during test.

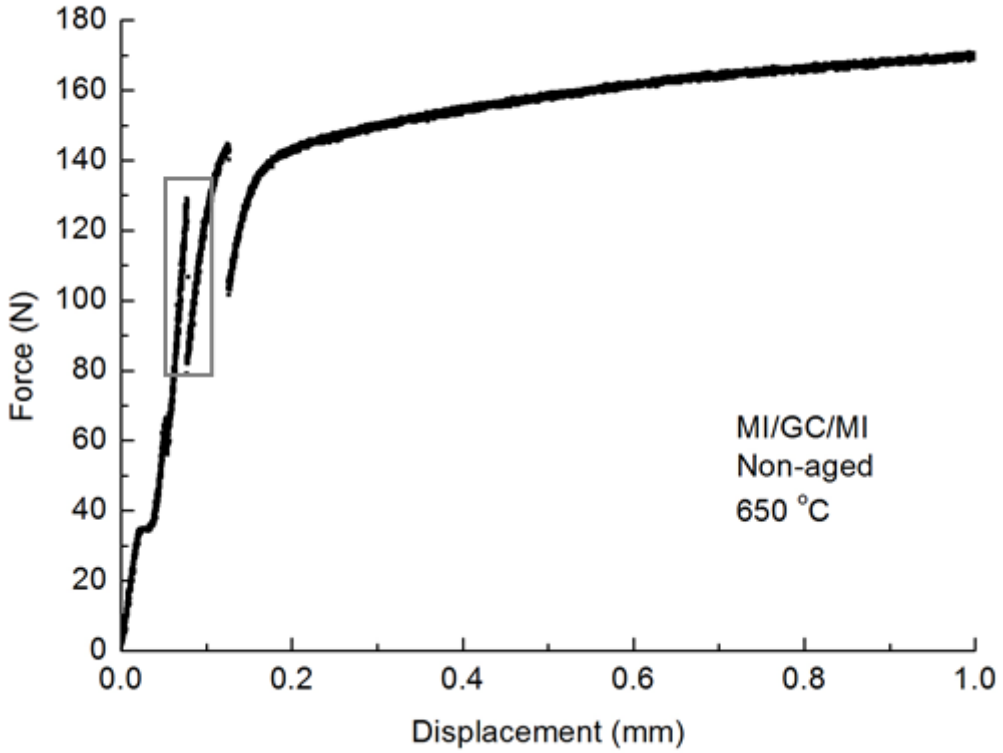

(a)

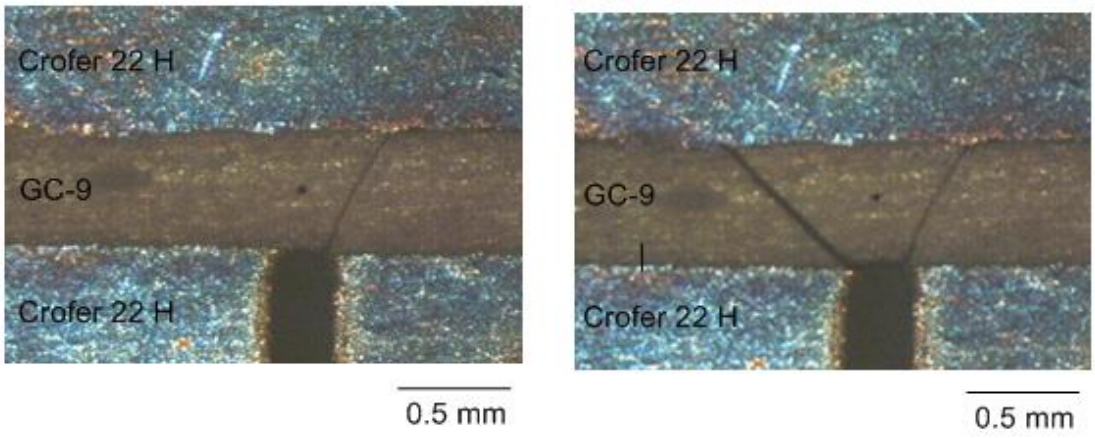

(b) (c)

Fig. 21 Representative results of non-aged metallic interconnect/glass-ceramic/notched metallic interconnect joint tested at 650 °C: (a) load-displacement relationship; (b) side view of specimen at the first load drop; (c) side view of specimen at the second load drop.

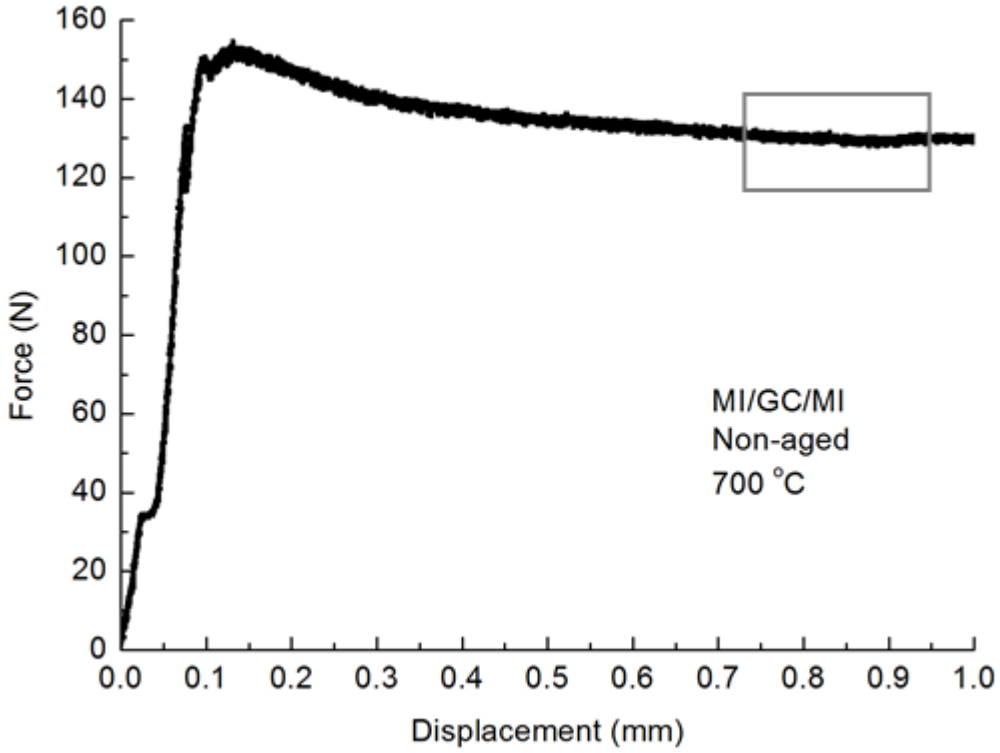

(a)

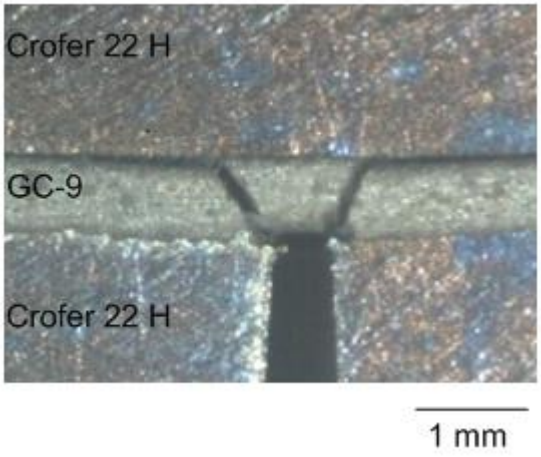

(b)

Fig. 22 Representative results of non-aged metallic interconnect/glass-ceramic/notched metallic interconnect joint tested at 700 ^{o}C: (a) load-displacement relationship; (b) side view of specimen at outlined region.

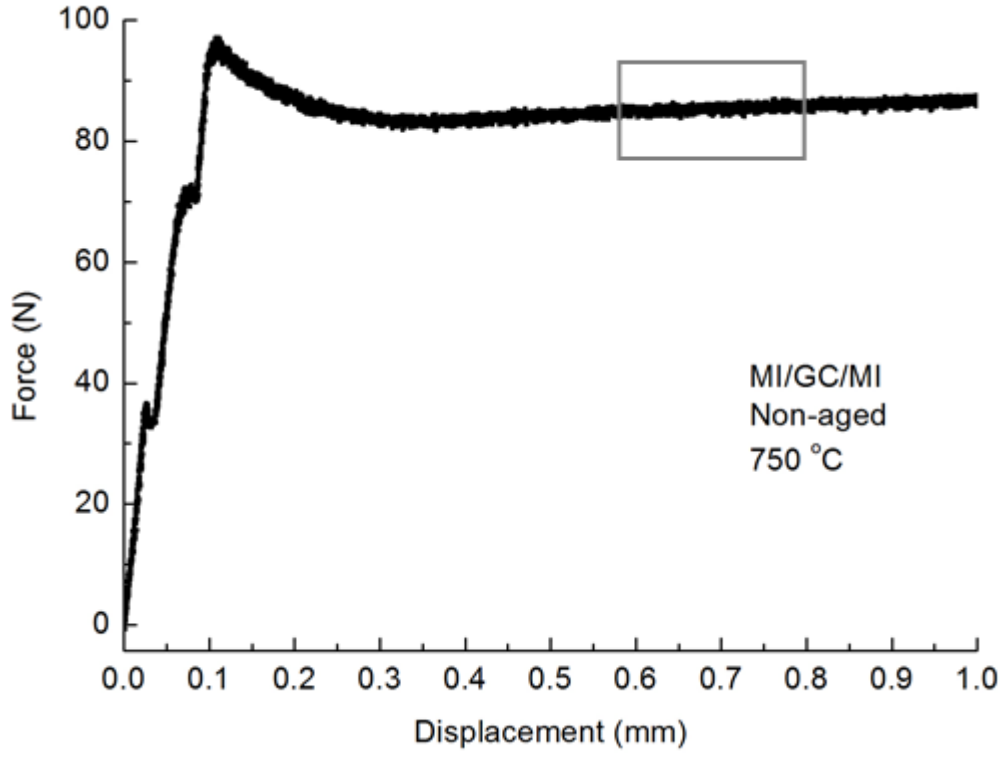

(a)

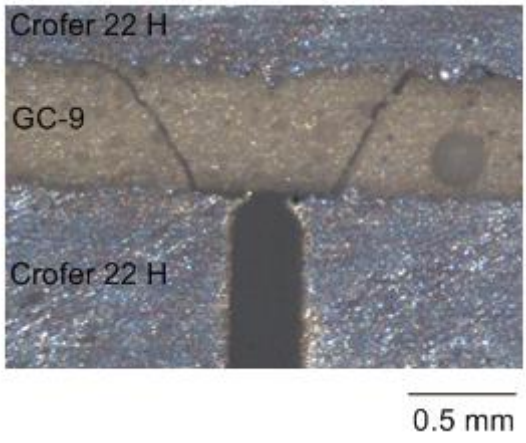

(b)

Fig. 23 Representative results of non-aged metallic interconnect/glass-ceramic/notched metallic interconnect joint tested at 750 °C: (a) load-displacement relationship; (b) side view of specimen at outlined region.

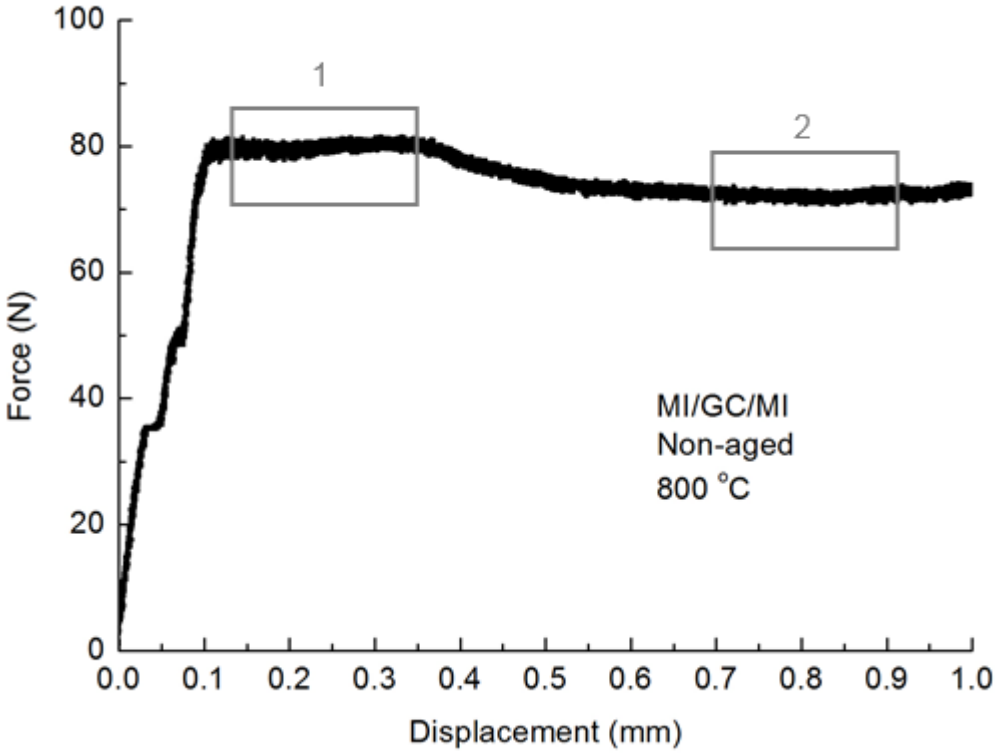

(a)

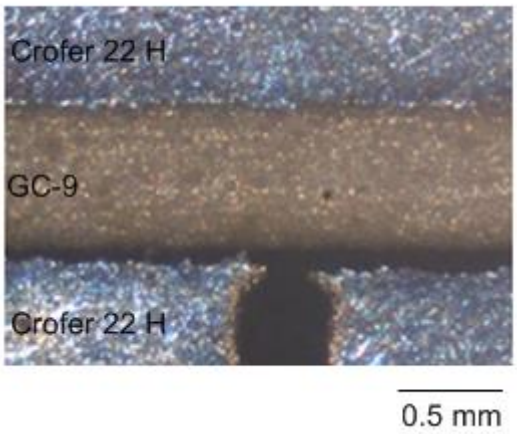

(b)

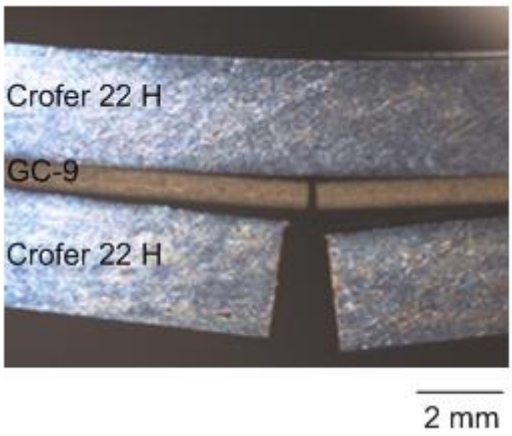

(c)

Fig. 24 Representative results of non-aged metallic interconnect/glass-ceramic/notched metallic interconnect joint tested at 800 °C: (a) load-displacement relationship; (b) side view of specimen at outlined region 1; (c) side view of specimen at outlined region 2.

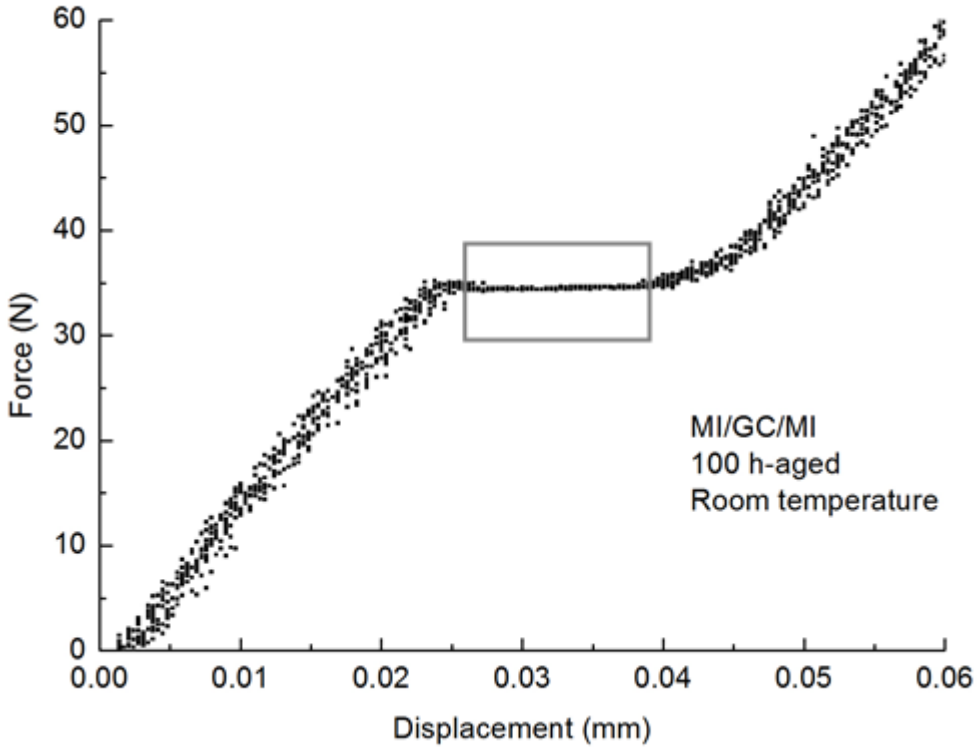

(a)

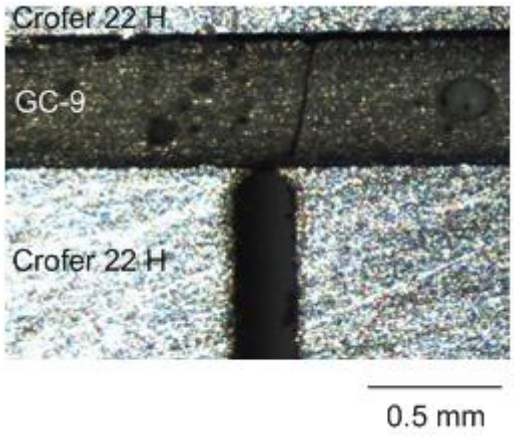

(b)

Fig. 25 Representative results of 100 h-aged metallic interconnect/glass-ceramic/notched metallic interconnect joint tested at room temperature: (a) load-displacement relationship; (b) side view of specimen during test.

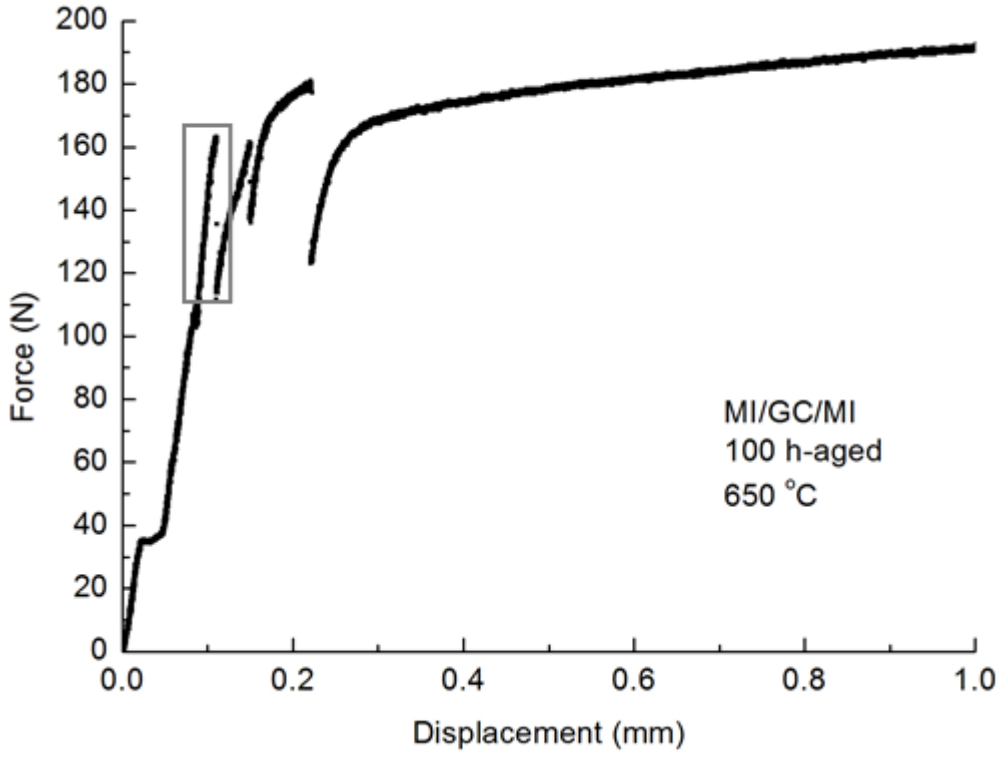

(a)

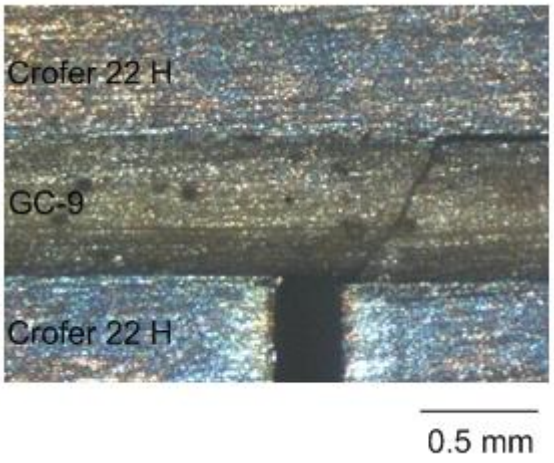

(b)

Fig. 26 Representative results of 100 h-aged metallic interconnect/glass-ceramic/notched metallic interconnect joint tested at 650 °C: (a) load-displacement relationship; (b) side view of specimen at the first load drop; (c) side view of specimen at the second load drop; (d) side view of specimen at the third load drop.

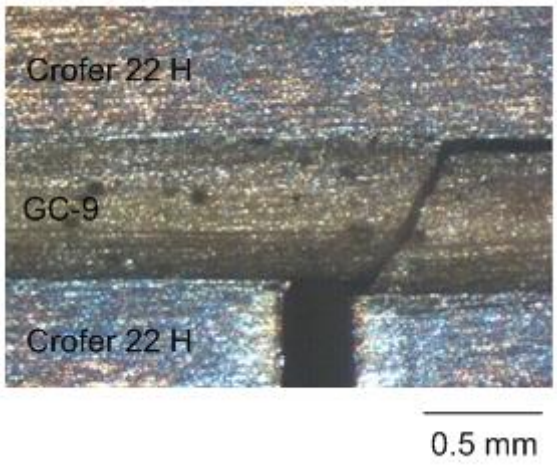

(c)

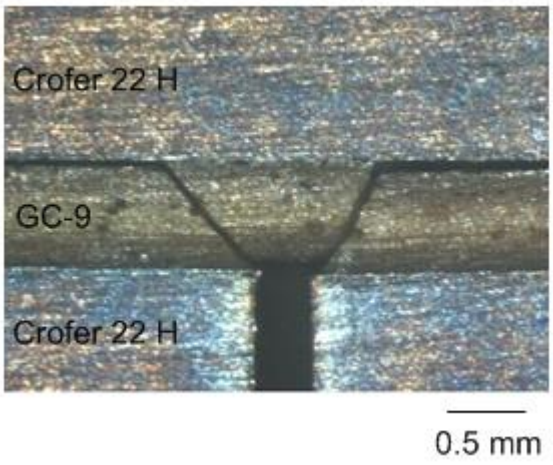

(d)

Fig. 26 (continued)

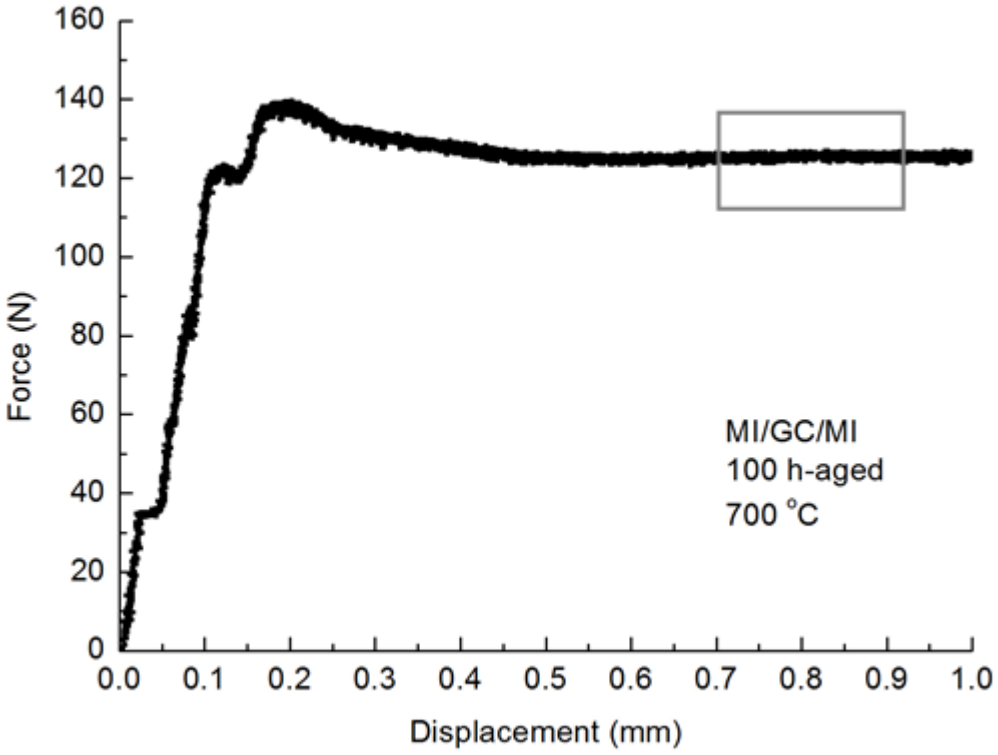

(a)

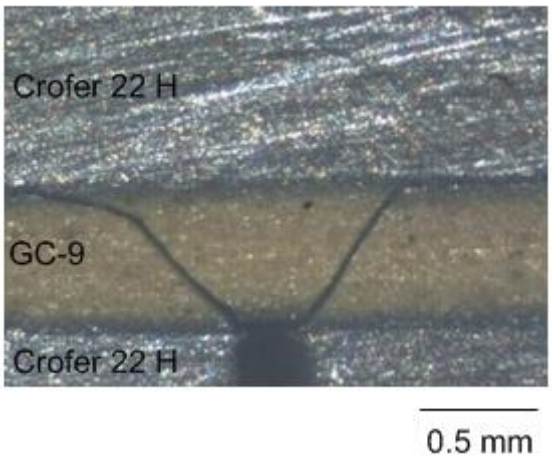

(b)

Fig. 27 Representative results of 100 h-aged metallic interconnect/glass-ceramic/notched metallic interconnect joint tested at 700 °C: (a) load-displacement relationship; (b) side view of specimen at outlined region.

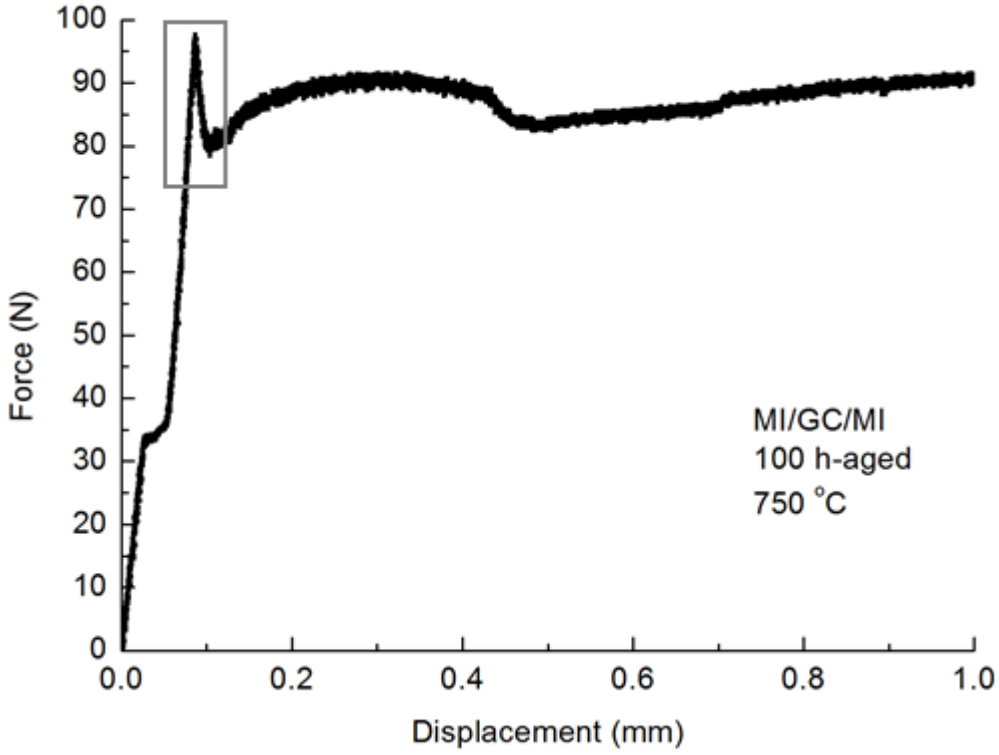

(a)

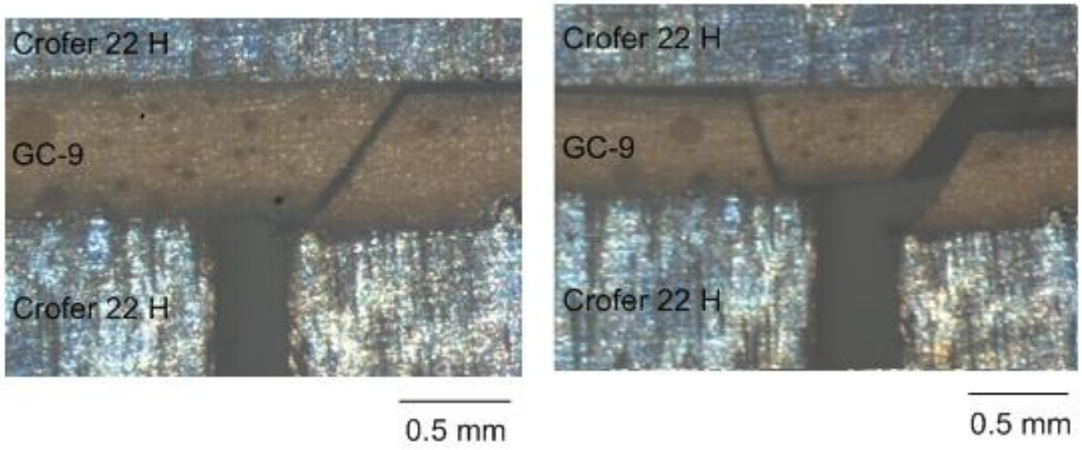

(b) (c)

Fig. 28 Representative results of 100 h-aged metallic interconnect/glass-ceramic/notched metallic interconnect joint tested at 750 °C: (a) load-displacement relationship; (b) side view of specimen at the first load drop; (c) side view of specimen at the second load drop.

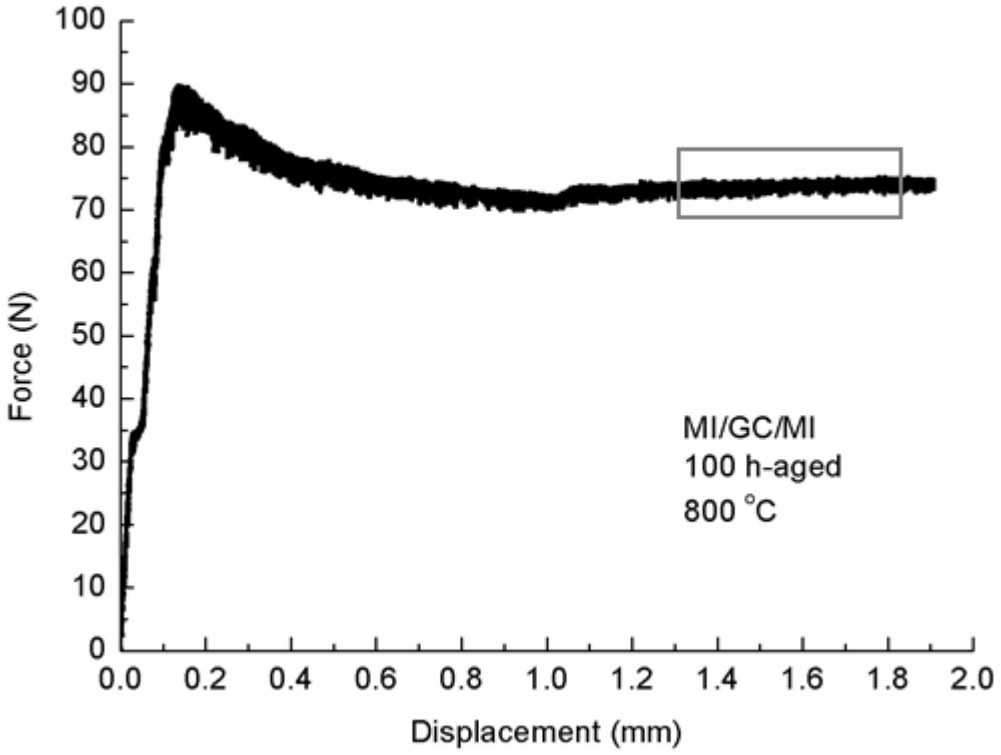

(a)

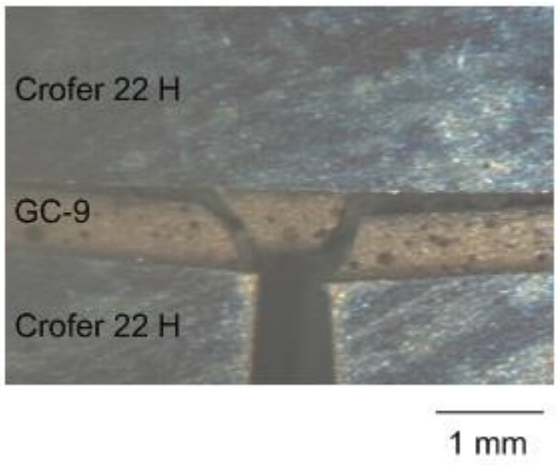

(b)

Fig. 29 Representative results of 100 h-aged metallic interconnect/glass-ceramic/notched metallic interconnect joint tested at 800 ^{o}C: (a) load-displacement relationship; (b) side view of specimen at outlined region.

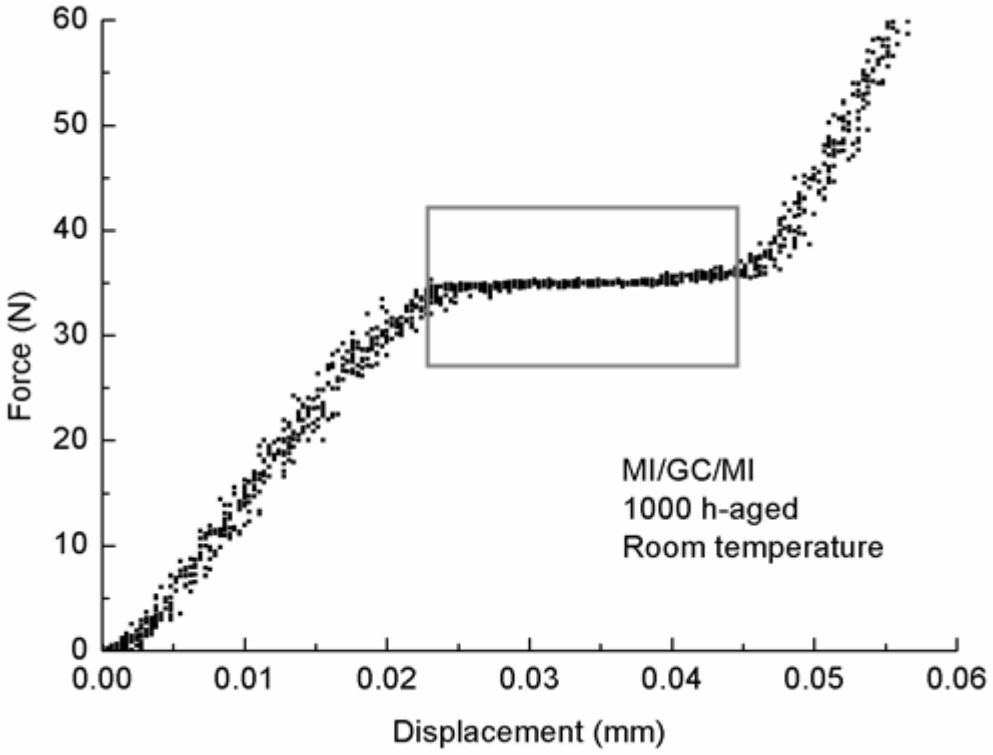

(a)

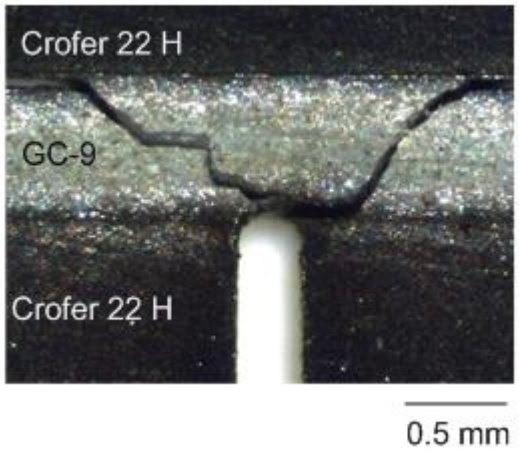

(b)

Fig. 30 Representative results of 1000 h-aged metallic interconnect/glass-ceramic/notched metallic interconnect joint tested at room temperature: (a) load-displacement relationship; (b) side view of specimen at outlined region.

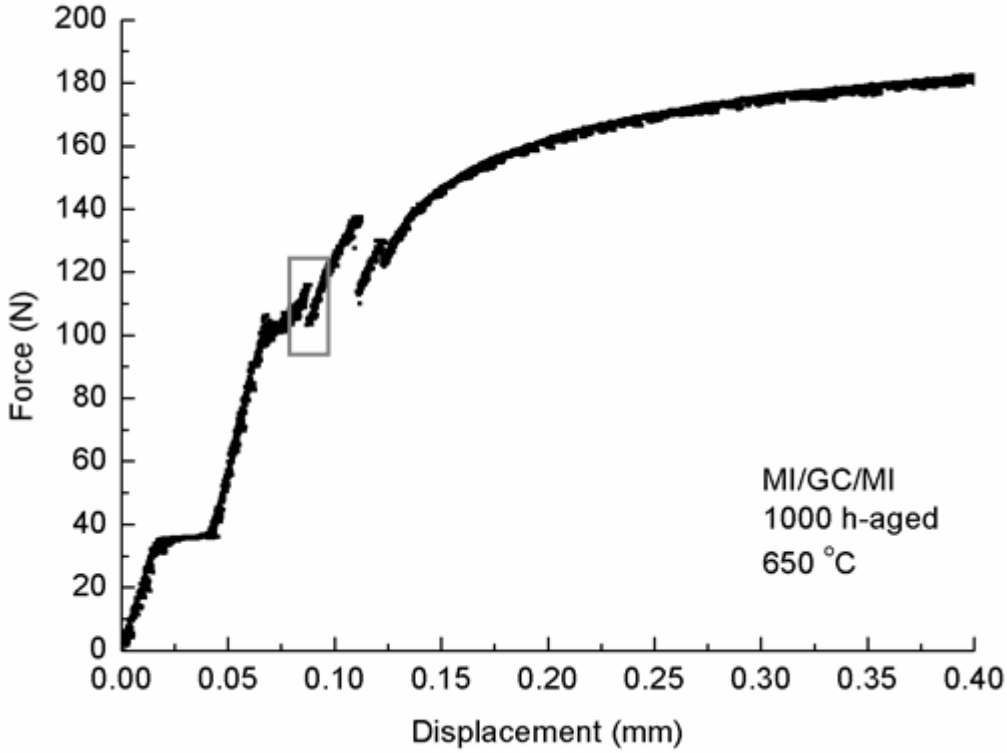

(a)

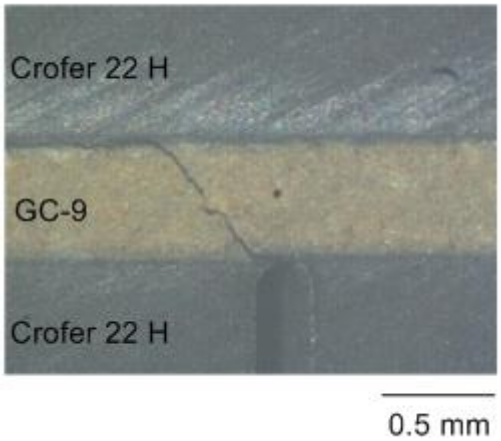

(b)

Fig. 31 Representative results of 1000 h-aged metallic interconnect/glass-ceramic/notched metallic interconnect joint tested at 650 °C: (a) load-displacement relationship; (b) side view of specimen at the first load drop; (c) side view of specimen at the second load drop; (d) side view of specimen at the third load drop.

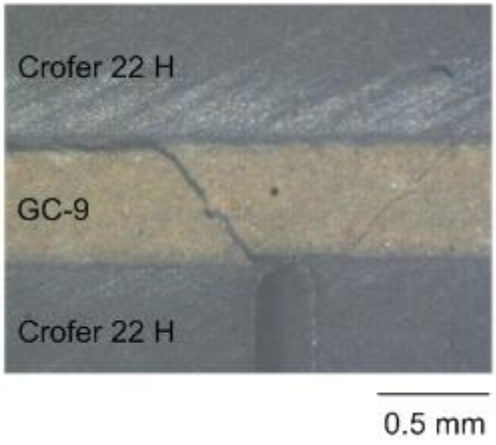

(c)

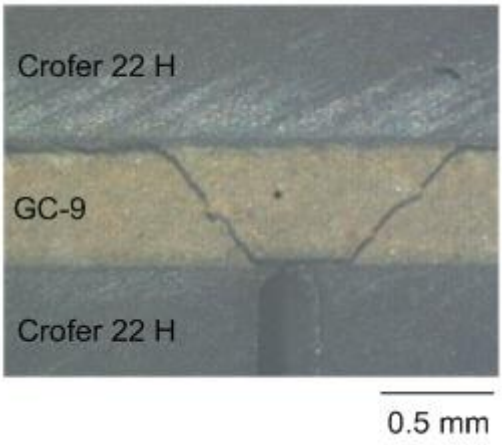

(d)

Fig. 31 (continued)

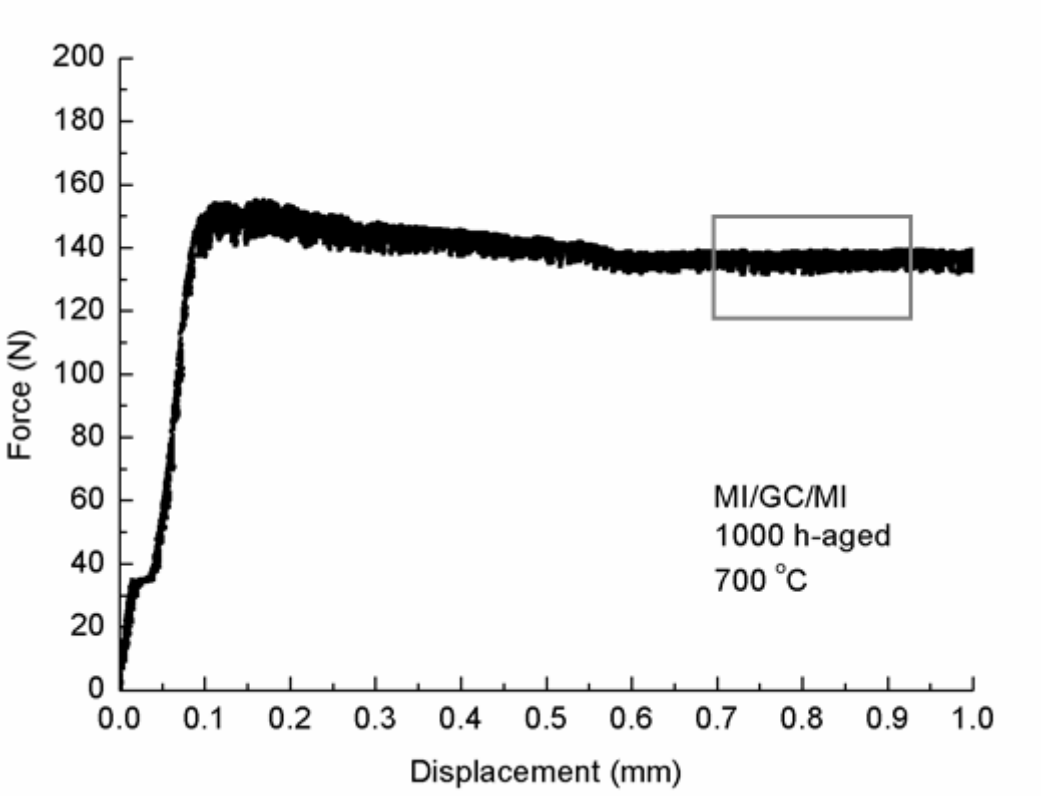

(a)

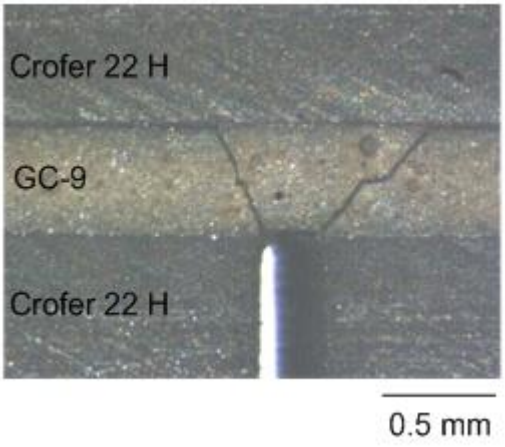

(b)

Fig. 32 Representative results of 1000 h-aged metallic interconnect/glass-ceramic/notched metallic interconnect joint tested at 700 °C: (a) load-displacement relationship; (b) side view of specimen at outlined region.

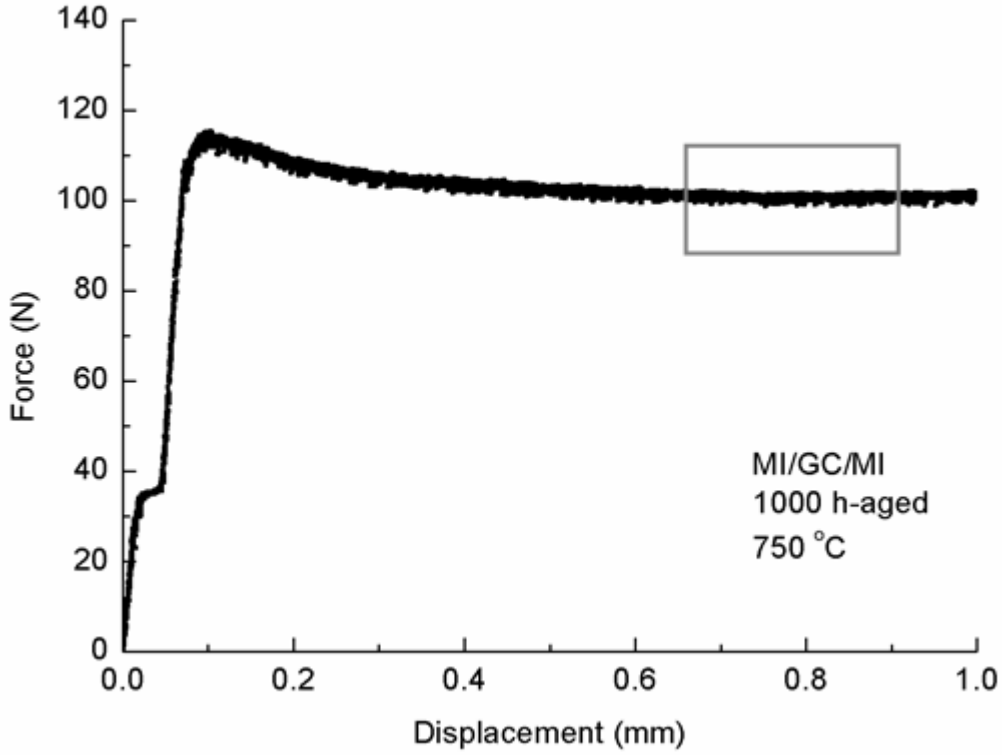

(a)

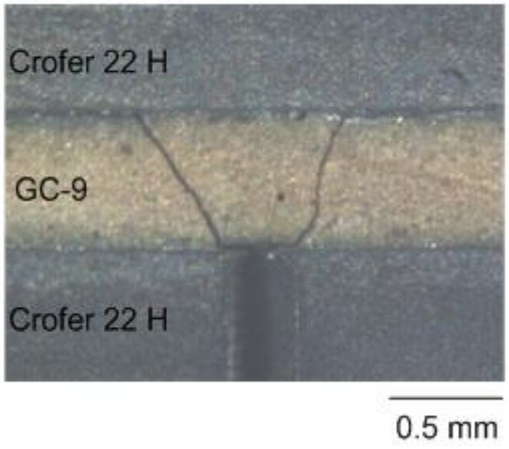

(b)

Fig. 33 Representative results of 1000 h-aged metallic interconnect/glass-ceramic/notched metallic interconnect joint tested at 750 °C: (a) load-displacement relationship; (b) side view of specimen at outlined region.

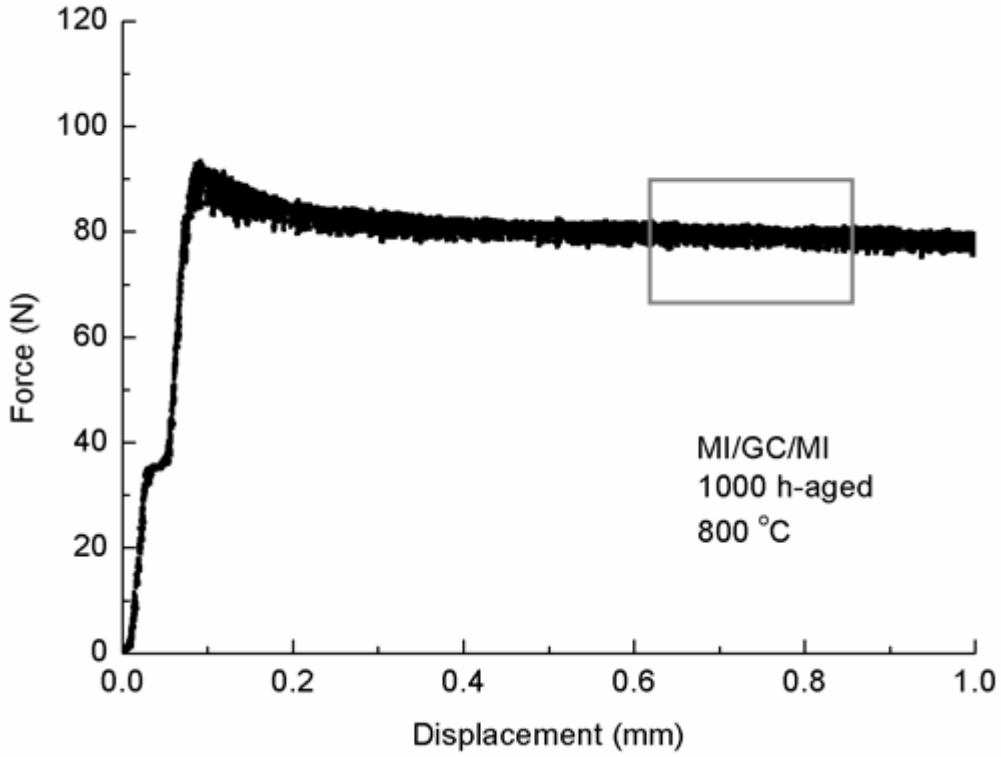

(a)

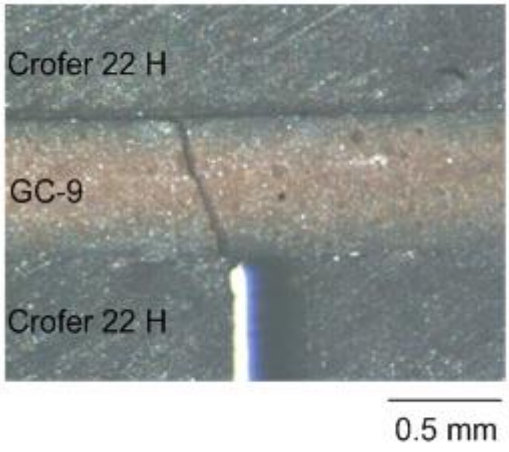

(b)

Fig. 34 Representative results of 1000 h-aged metallic interconnect/glass-ceramic/notched metallic interconnect joint tested at 800 °C: (a) load-displacement relationship; (b) side view of specimen at outlined region.

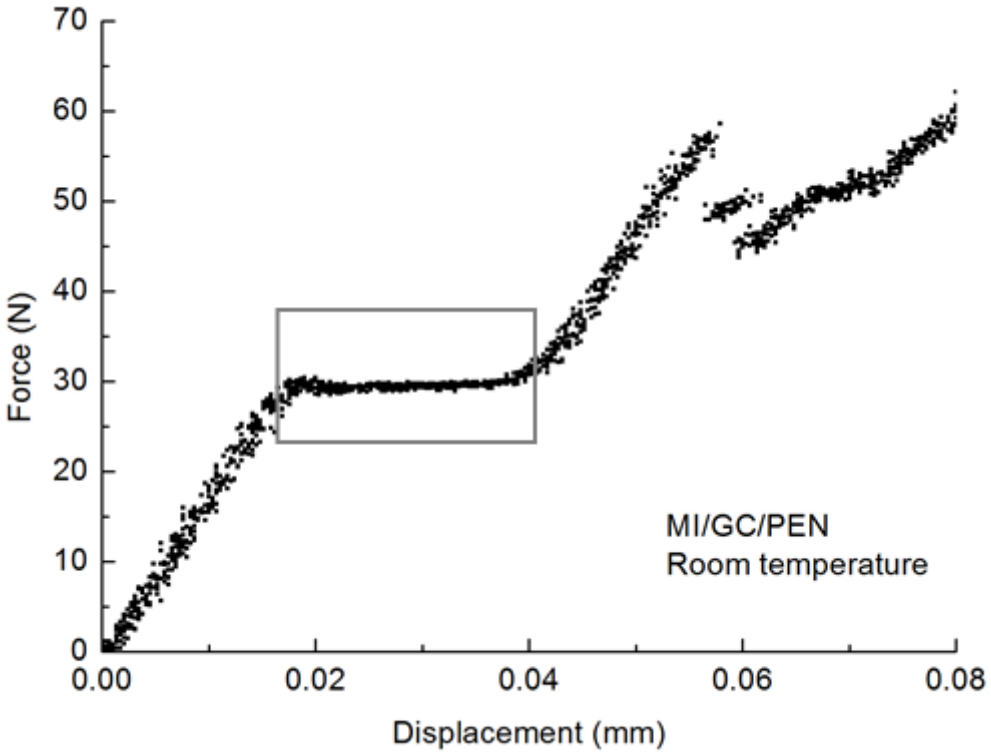

(a)

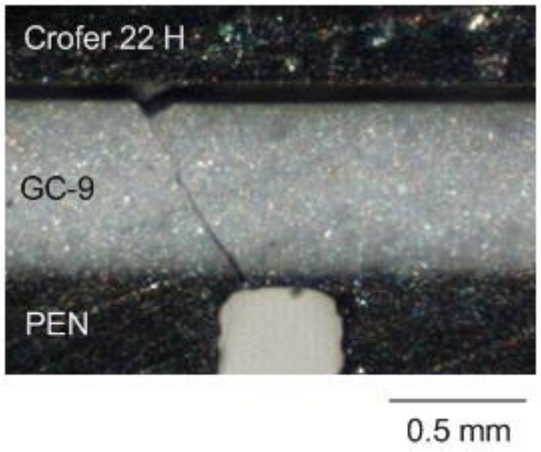

(b)

Fig. 35 Representative results of metallic interconnect/glass-ceramic/notched PEN joint tested at room temperature: (a) load-displacement relationship; (b) side view of specimen during test.

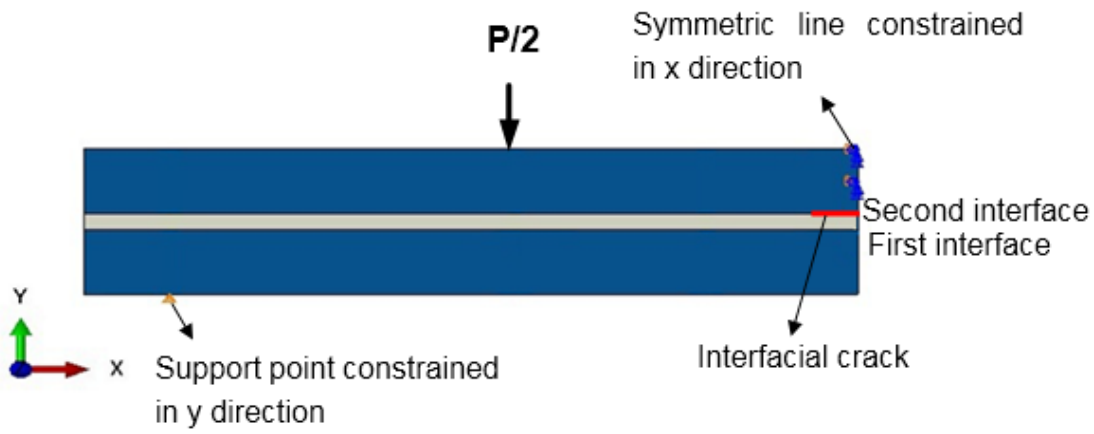

(a)

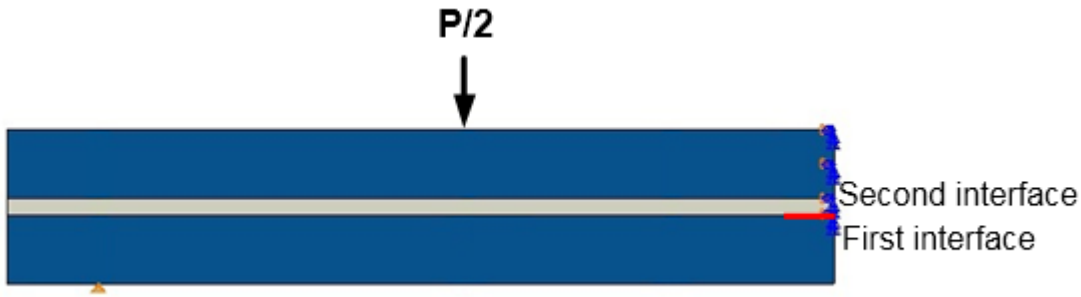

(b)

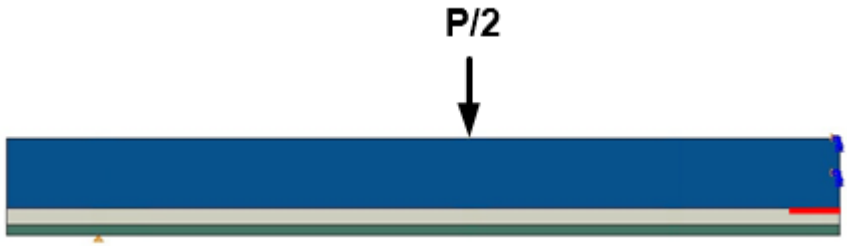

(c)

Fig. 36 FEA models of interfacial cracking in various four-point bending specimens: (a) metallic interconnect/glass-ceramic/metallic interconnect with a crack at the second interface; (b) metallic interconnect/glass-ceramic/metallic interconnect with a crack at the first interface; (c) metallic interconnect/glass-ceramic/PEN with a crack at the metallic interconnect/glass-ceramic interface.

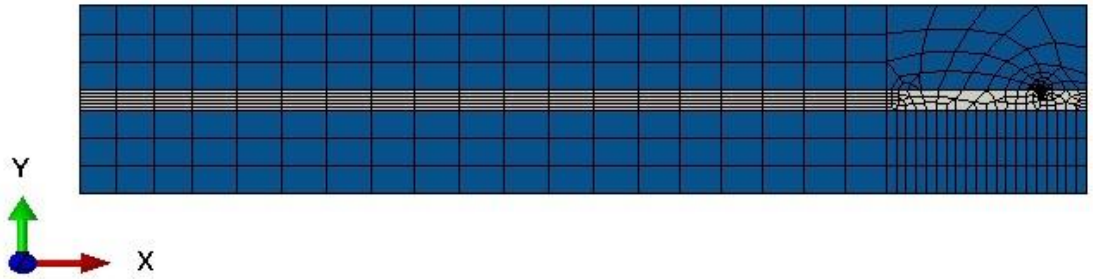

(a)

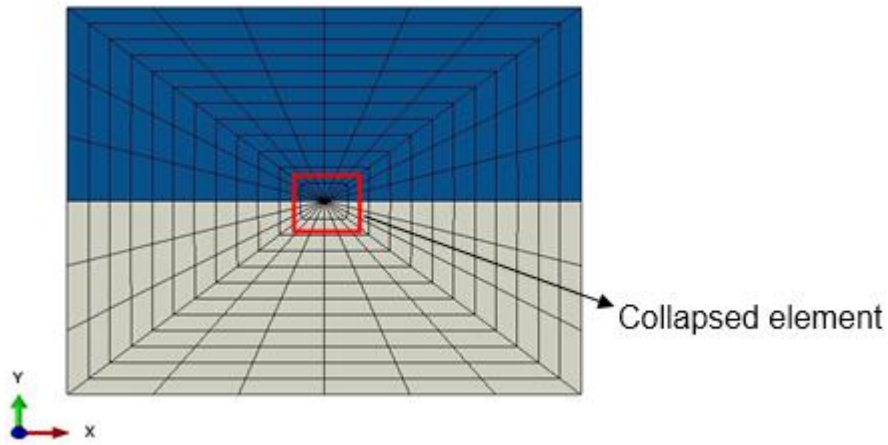

(b)

Fig. 37 Mesh configuration for the model of Fig. 36(a): (a) overall mesh configuration; (b) detail of focused mesh around a crack tip.

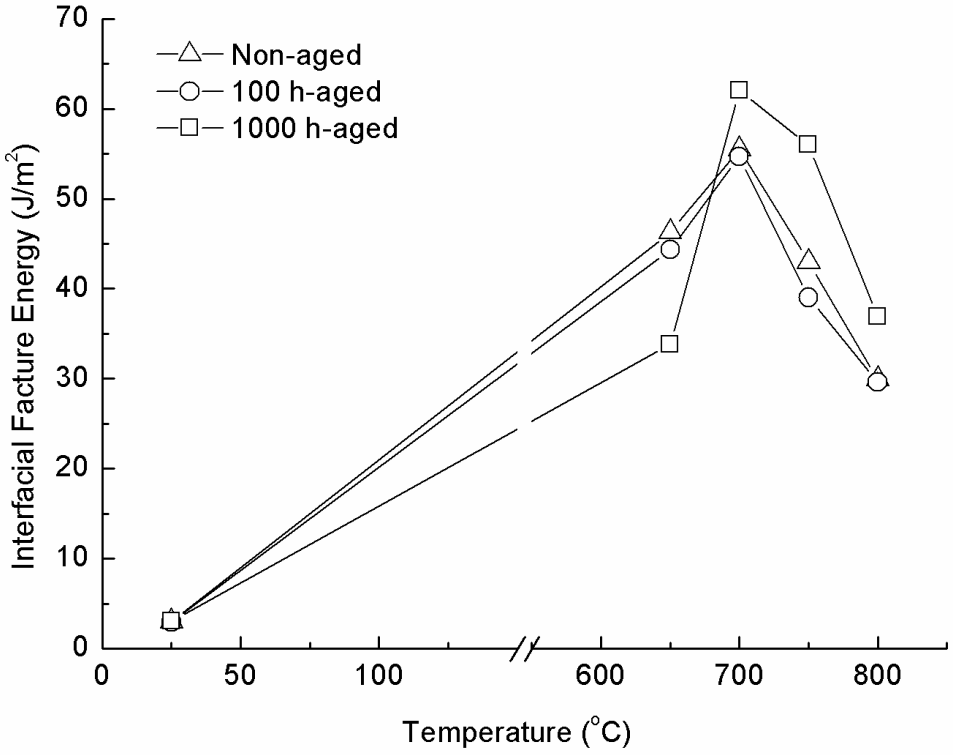

Fig. 38 Variation of average interfacial fracture energy with temperature for non-aged, 100 h-aged, and 1000 h-aged glass-ceramic/metallic interconnect joints.

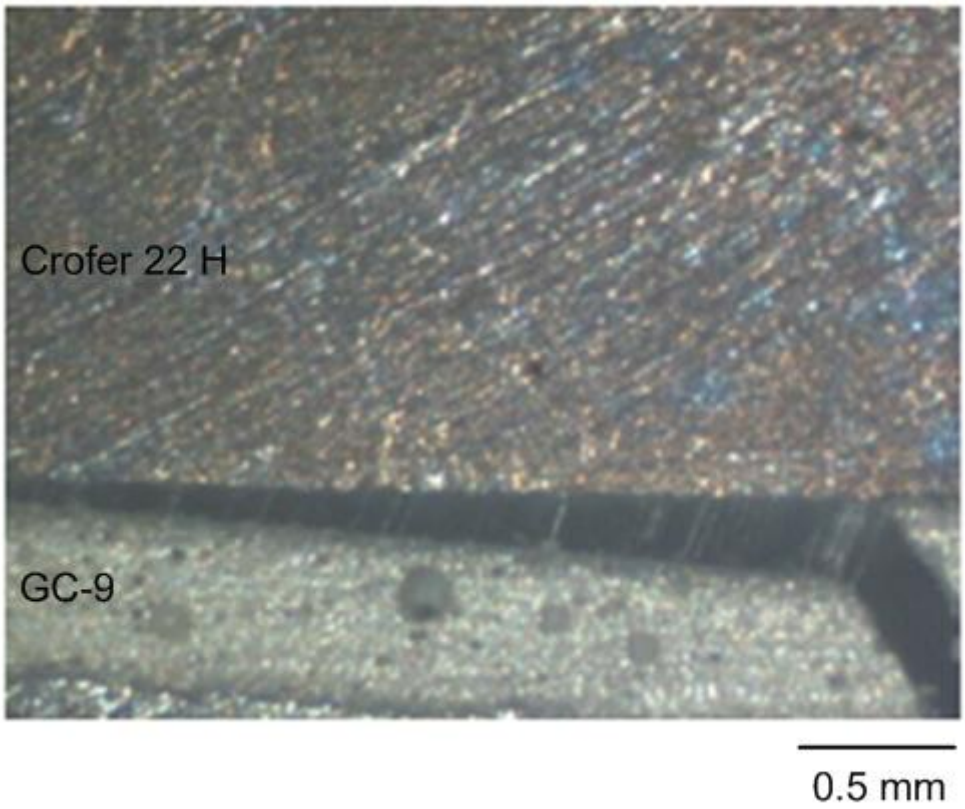

Fig. 39 Bridging phenomenon in a crack at the interface of a metallic interconnect/glass-ceramic/notched metallic interconnect specimen tested at 700 ^{o}C.

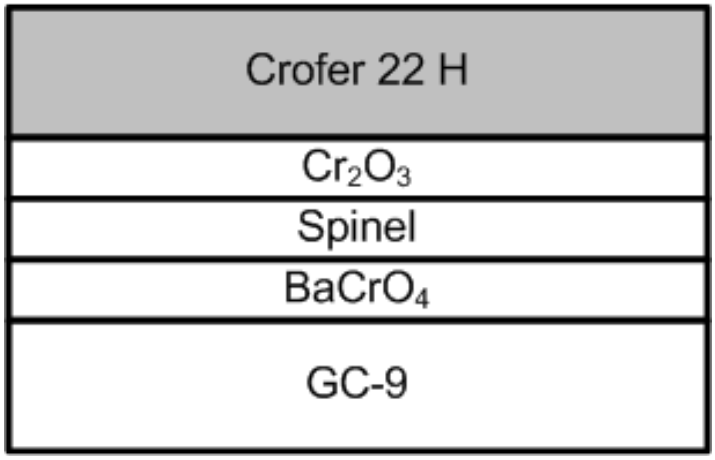

Fig. 40 Schematic of oxide layers between Crofer 22 H and GC-9 glass-ceramic.

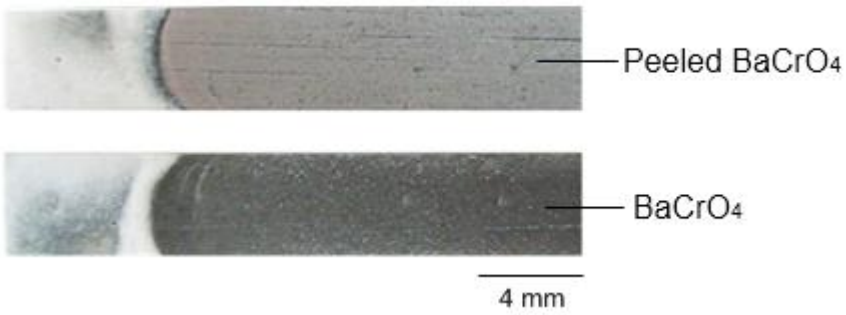

(a)

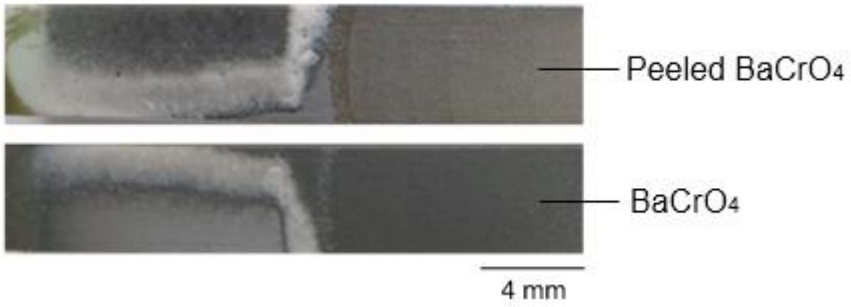

(b)

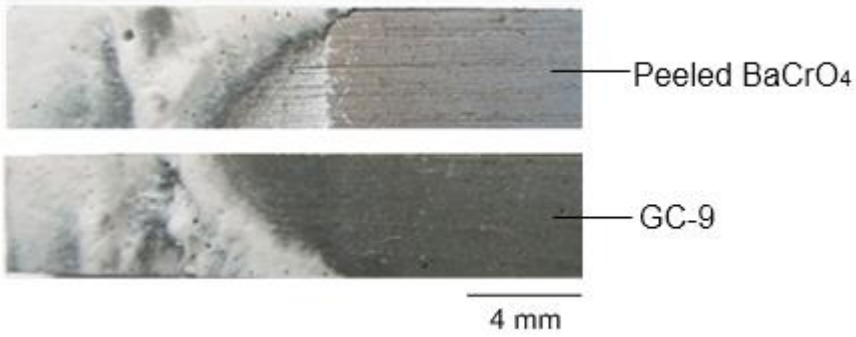

(e)

Fig. 41 Failure patterns of non-aged metallic interconnect/glass-ceramic/notched metallic interconnect specimens tested at: (a) room temperature; (b) 650 ^{o}C; (c) 700 ^{o}C; (d) 750 ^{o}C; (e) 800 ^{o}C.

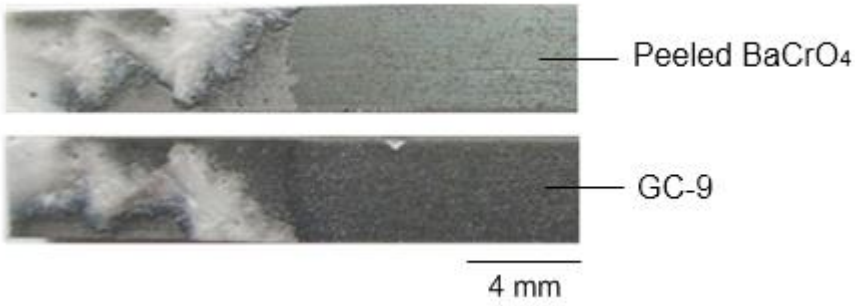

(d)

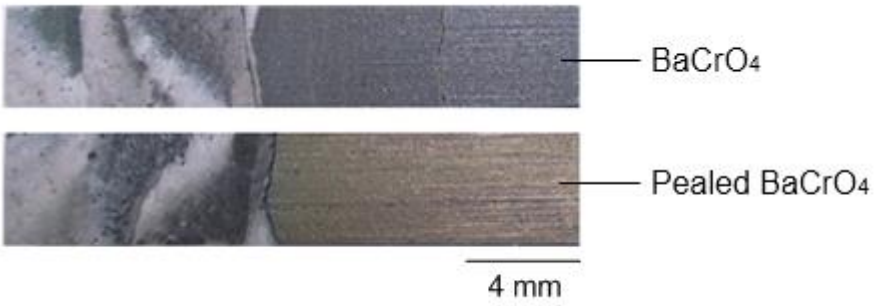

(e)

Fig. 41 (continued)

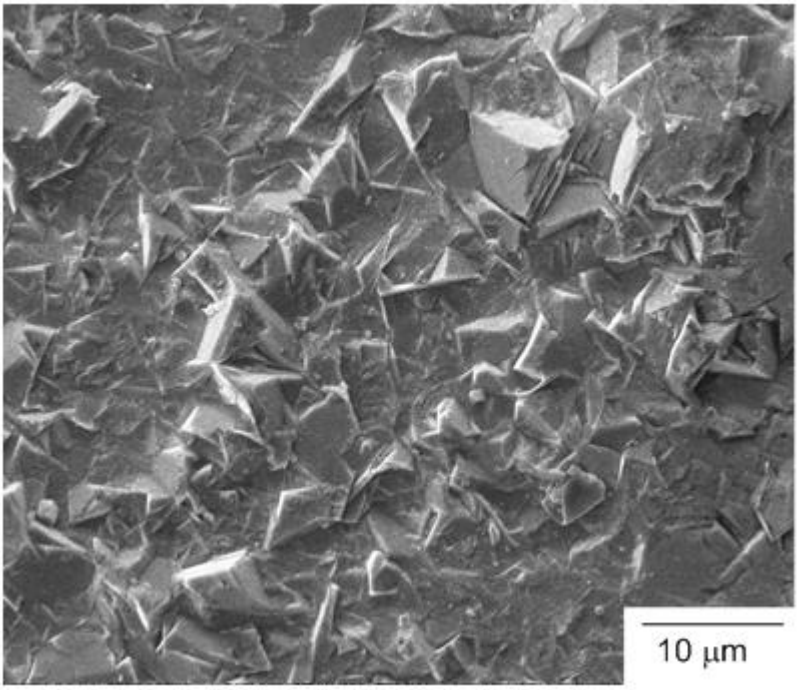

(a)

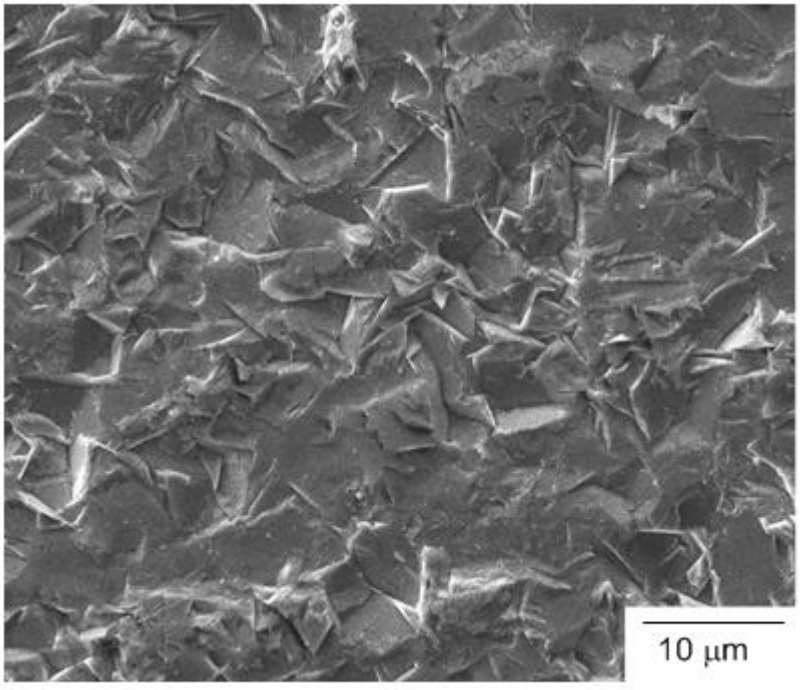

(b)

Fig. 42 Fracture surfaces of non-aged specimen shown in Fig. 41(a): (a) SEM micrograph of the upper micrograph in Fig. 41(a); (b) SEM micrograph of the lower micrograph in Fig. 41(a).

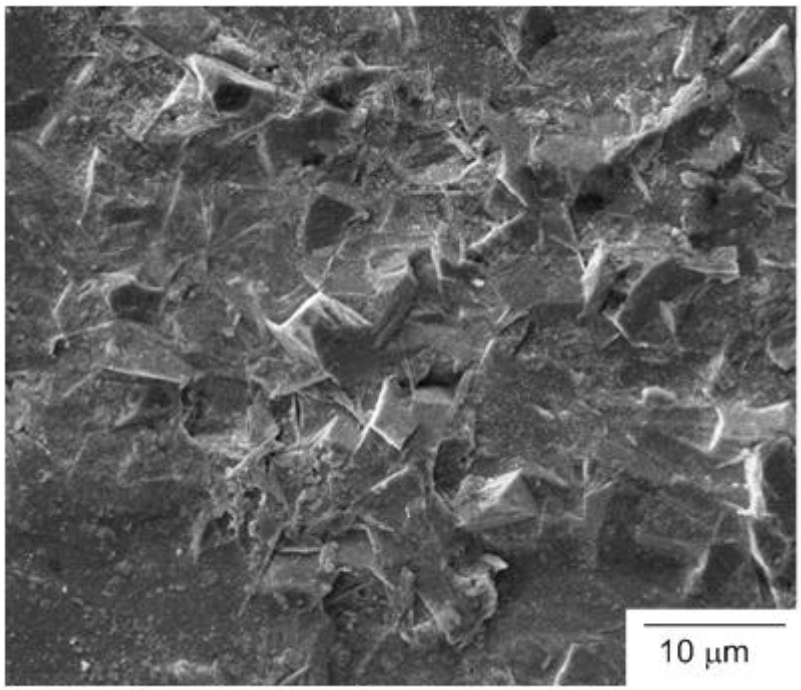

(a)

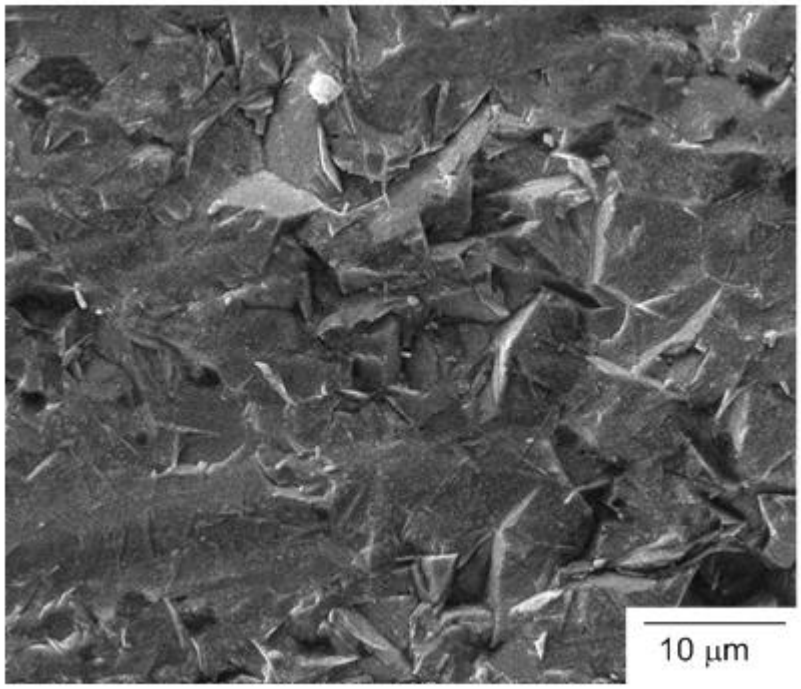

(b)

Fig. 43 Fracture surfaces of non-aged specimen shown in Fig. 41(b): (a) SEM micrograph of the upper micrograph in Fig. 41(b); (b) SEM micrograph of the lower micrograph in Fig. 41(b).

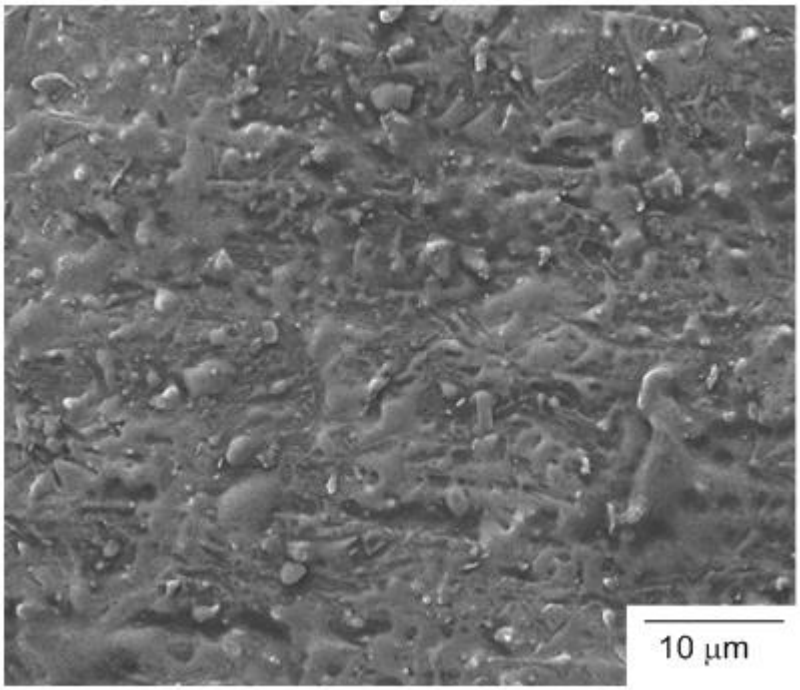

(a)

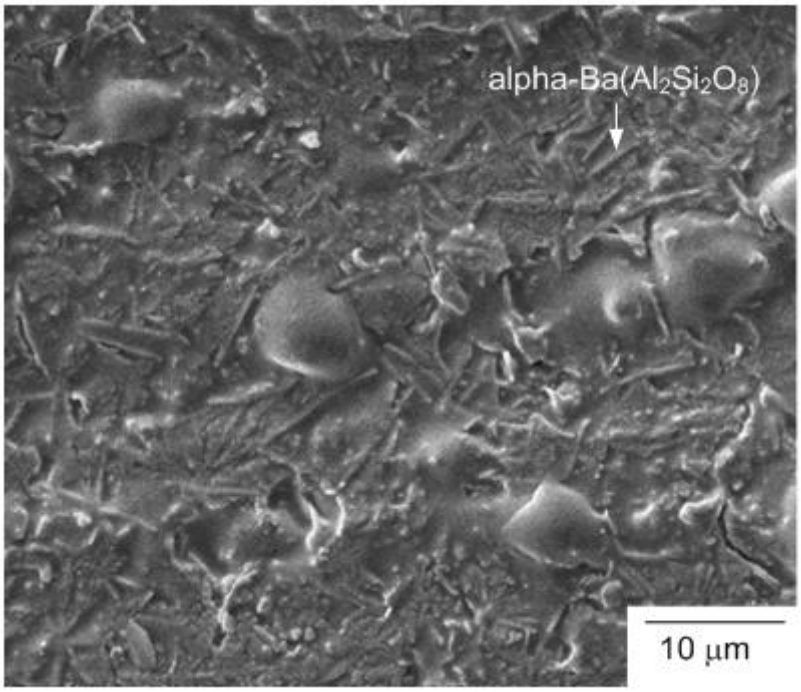

(b)

Fig. 44 Fracture surfaces of non-aged specimen shown in Fig. 41(c): (a) SEM micrograph of the upper micrograph in Fig. 41(c); (b) SEM micrograph of the lower micrograph in Fig. 41(c).

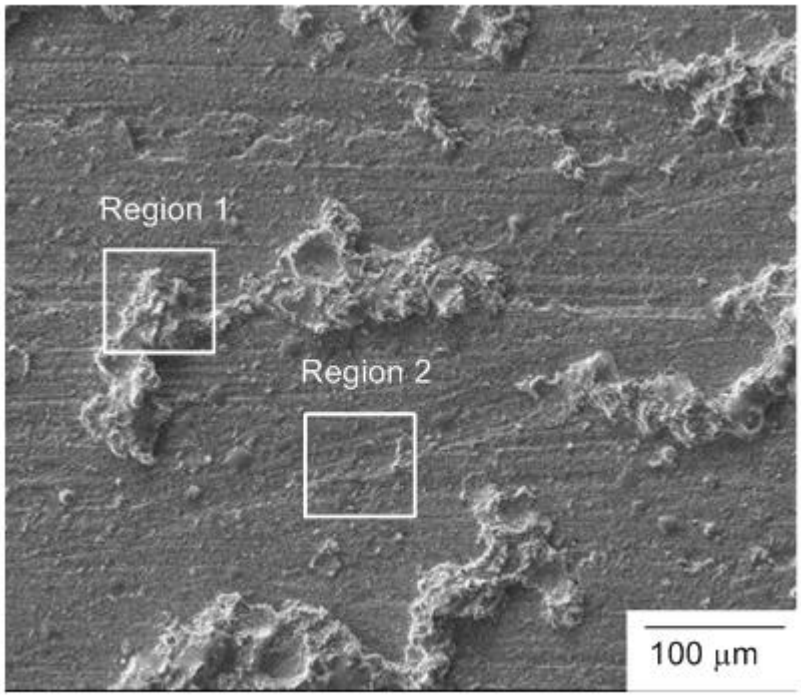

(a)

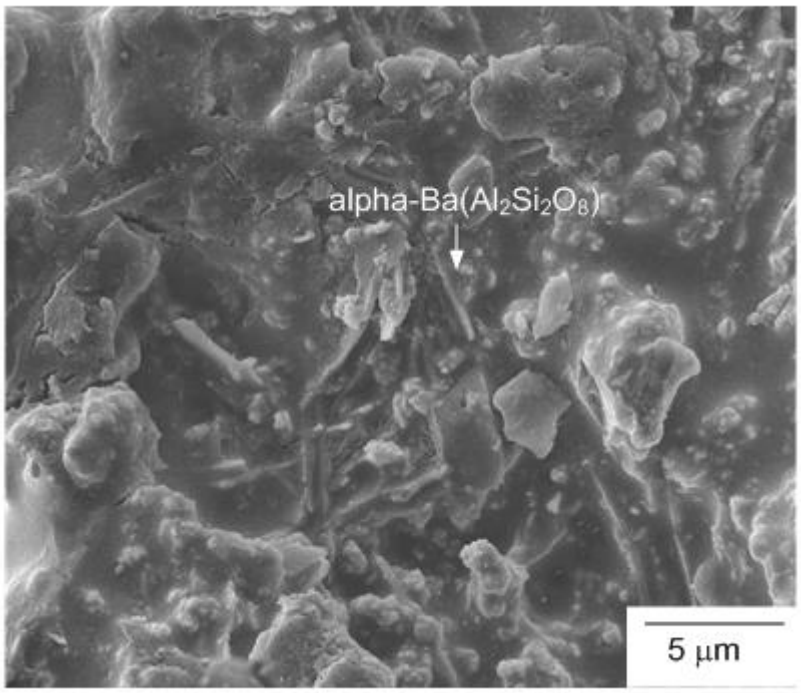

(b)

Fig. 45 Fracture surfaces of non-aged specimen shown in Fig. 41(d): (a) SEM micrograph of the upper micrograph in Fig. 41(d); (b) a high magnification view of region 1; (c) a high magnification view of region 2.

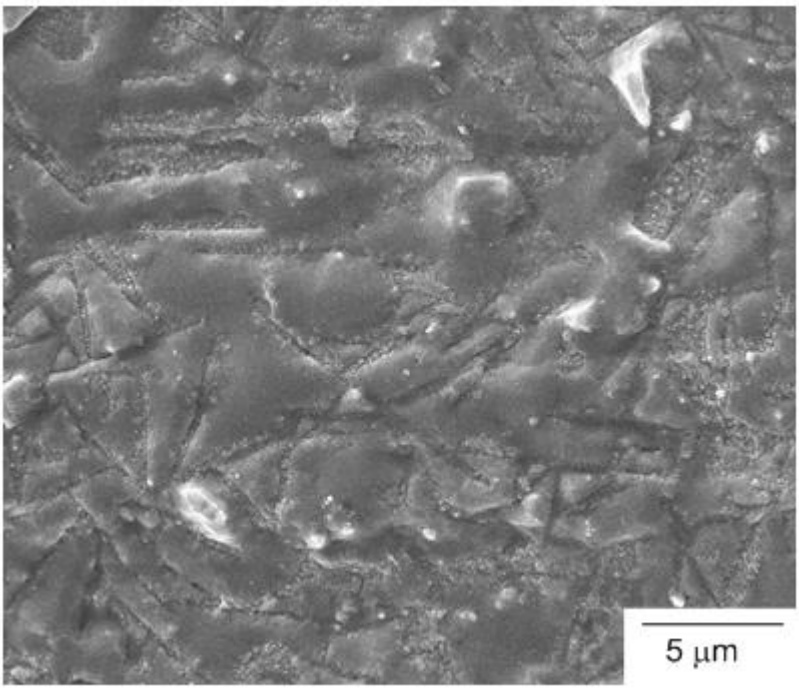

(c)

Fig. 45 (continued)

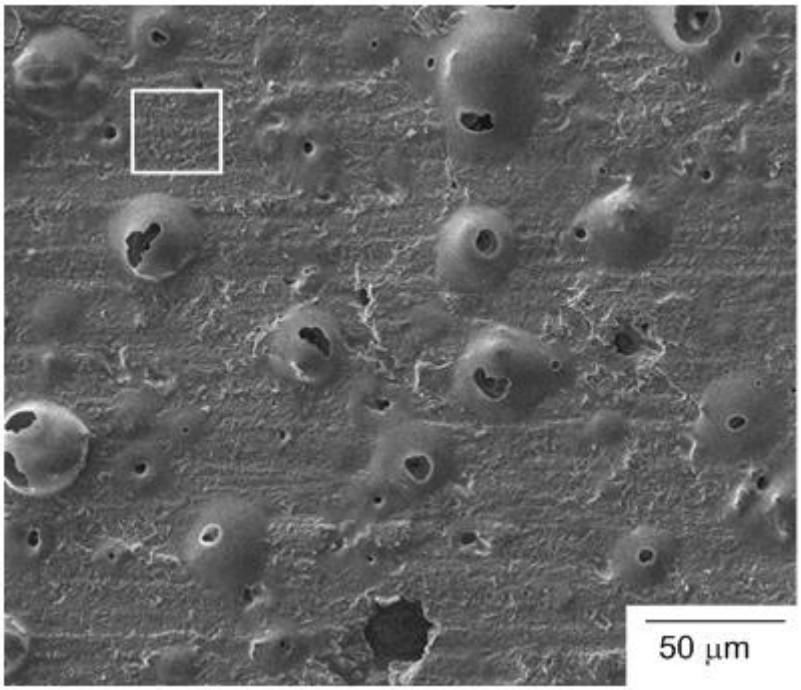

(a)

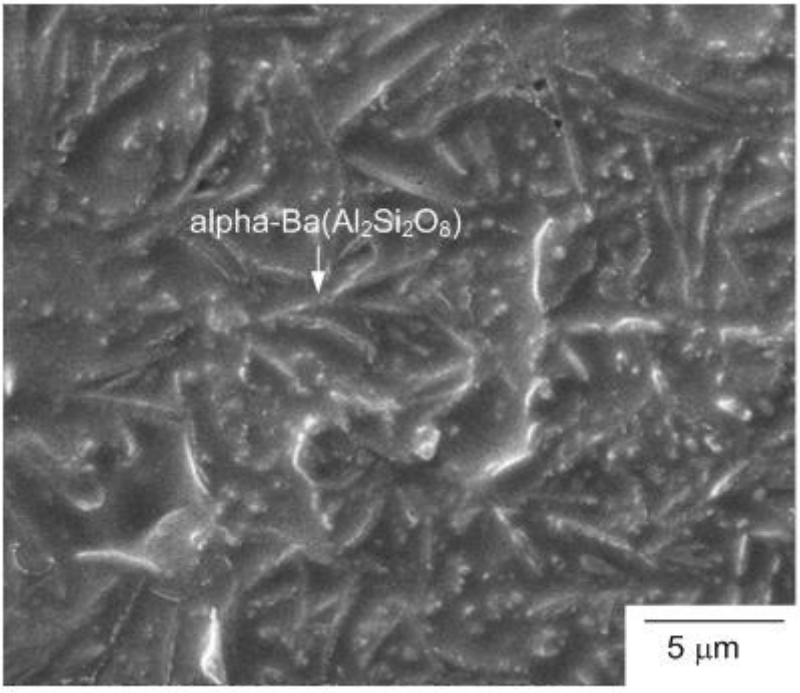

(b)

Fig. 46 Fracture surfaces of non-aged specimen shown in Fig. 41(d): (a) SEM micrograph of the lower micrograph in Fig. 41(d); (b) a high magnification view of outlined region.

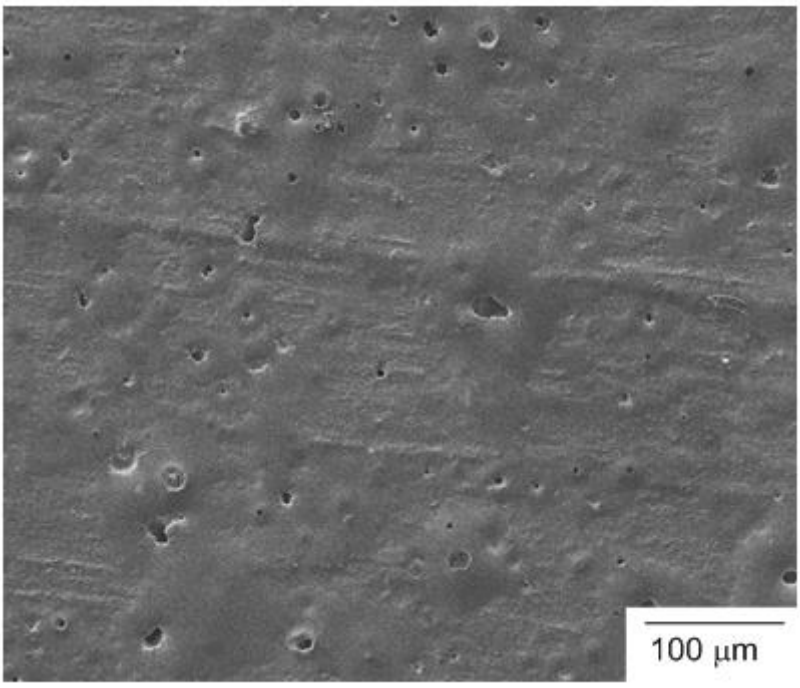

(a)

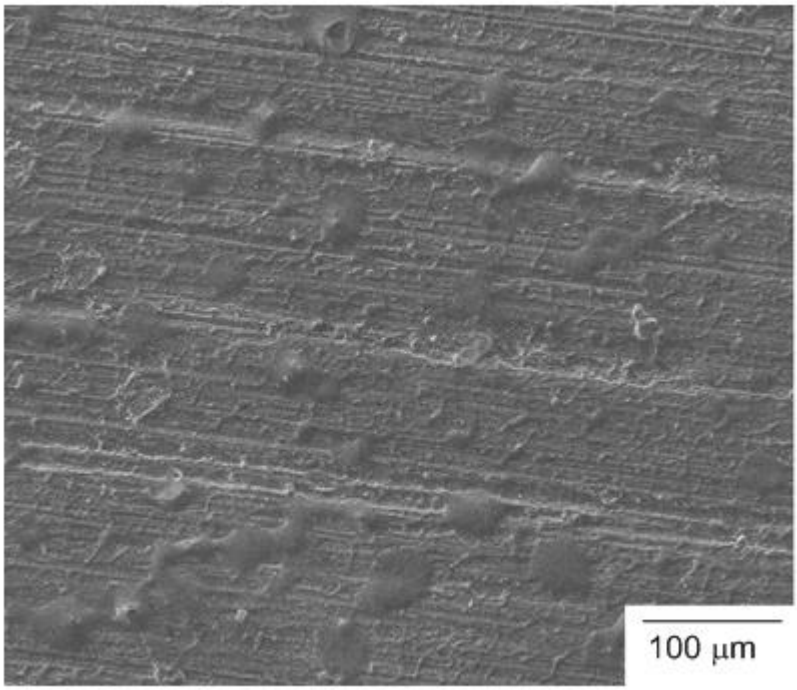

(b)

Fig. 47 Fracture surfaces of non-aged specimen shown in Fig. 41(e): (a) SEM micrograph of the upper micrograph in Fig. 41(e); (b) SEM micrograph of the lower micrograph in Fig. 41(e).

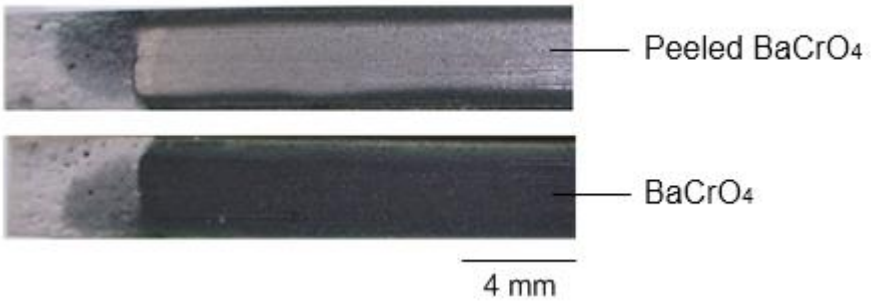

(a)

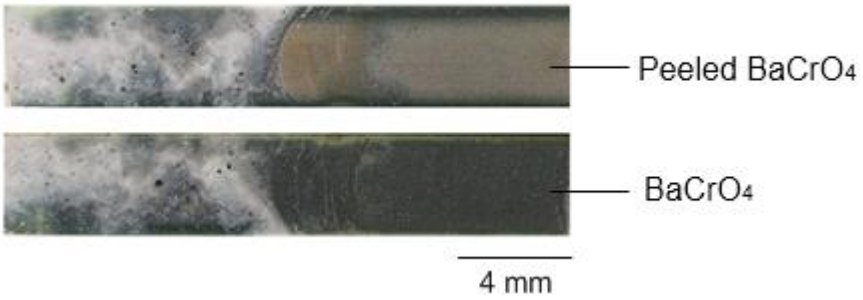

(b)

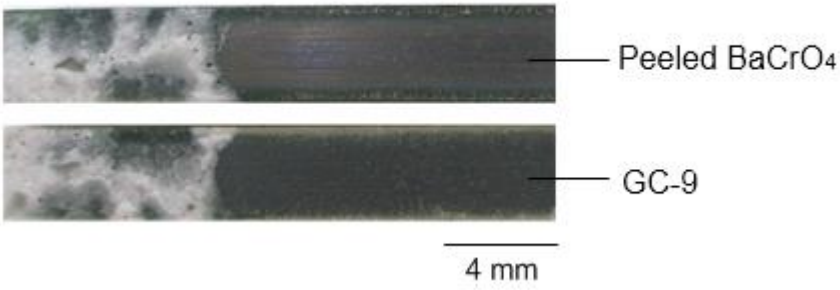

(c)

Fig. 48 Failure patterns of 100 h-aged metallic interconnect/glass-ceramic/notched metallic interconnect specimens tested at: (a) room temperature; (b) 650 ^{o}C; (c) 700 ^{o}C; (d) 750 ^{o}C; (e) 800 ^{o}C.

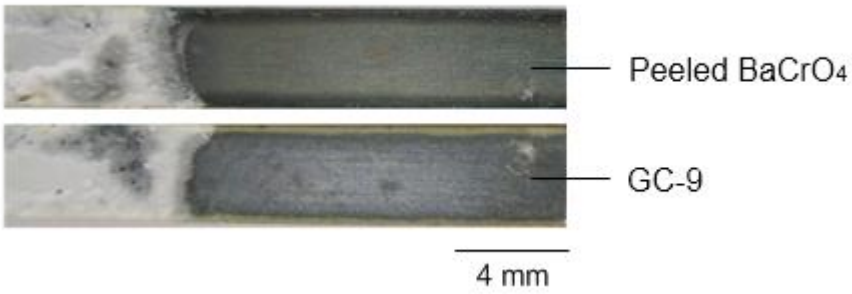

(d)

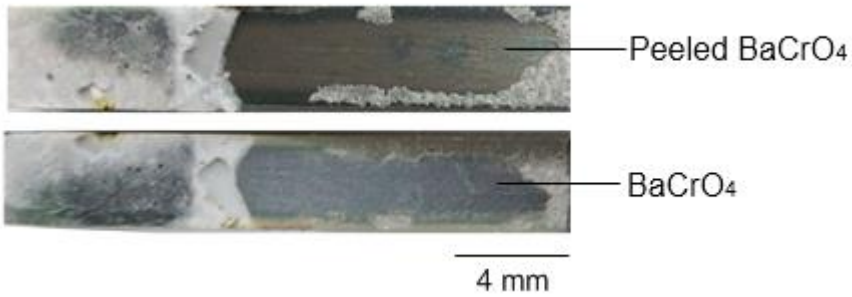

(e)

Fig. 48 (continued)

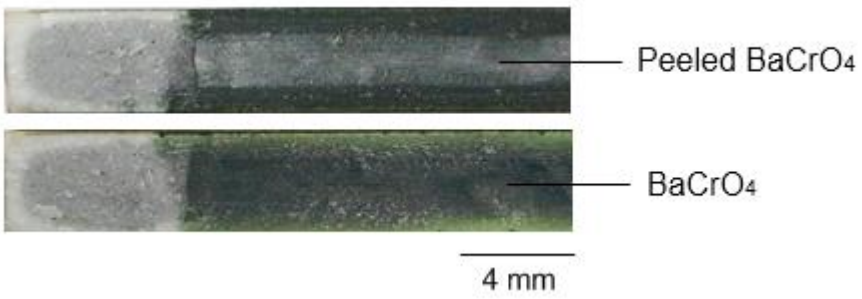

(a)

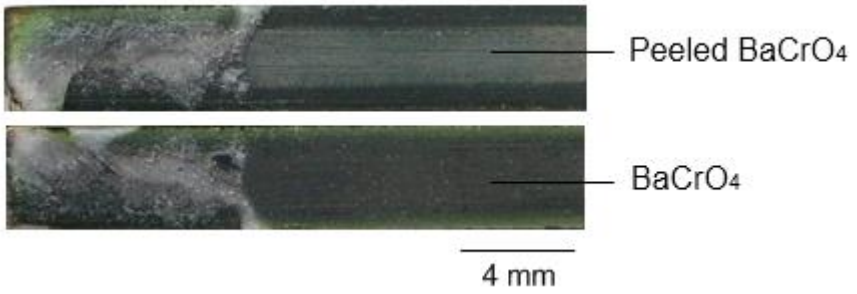

(b)

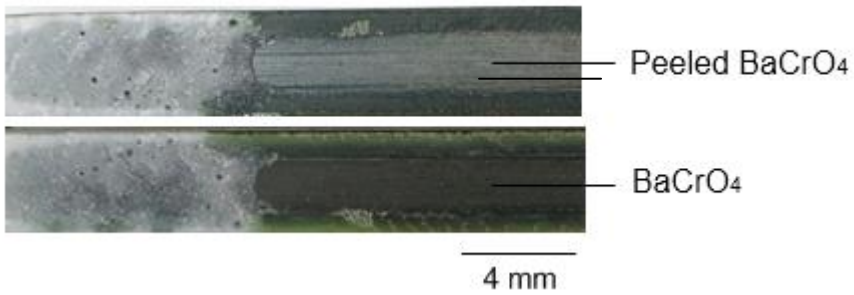

(c)

Fig. 49 Failure patterns of 1000 h-aged metallic interconnect/glass-ceramic/notched metallic interconnect specimens tested at: (a) room temperature; (b) 650 ^{o}C; (c) 700 ^{o}C; (d) 750 ^{o}C; (e) 800 ^{o}C.

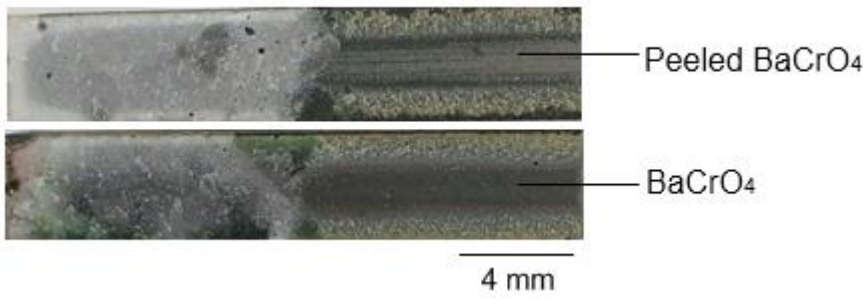

(d)

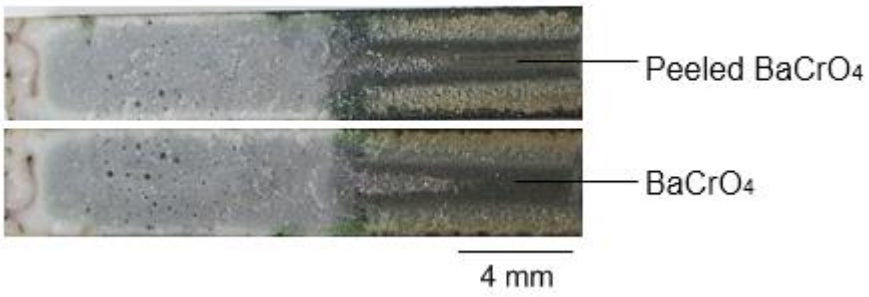

(e)

Fig. 49 (continued)

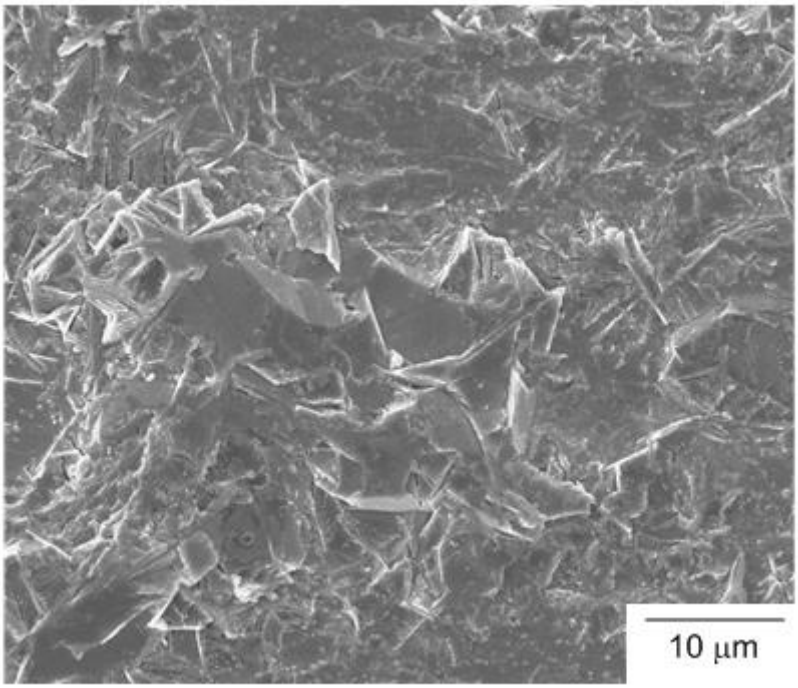

(a)

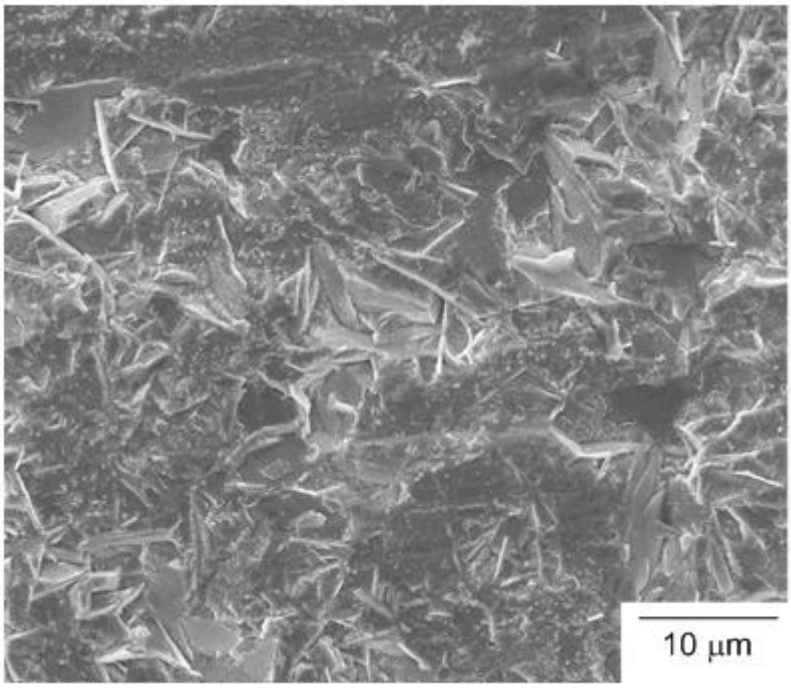

(b)

Fig. 50 Fracture surfaces of 1000 h-aged specimen shown in Fig. 49(a): (a) SEM micrograph of the upper micrograph in Fig. 49(a); (b) SEM micrograph of the lower micrograph in Fig. 49(a).

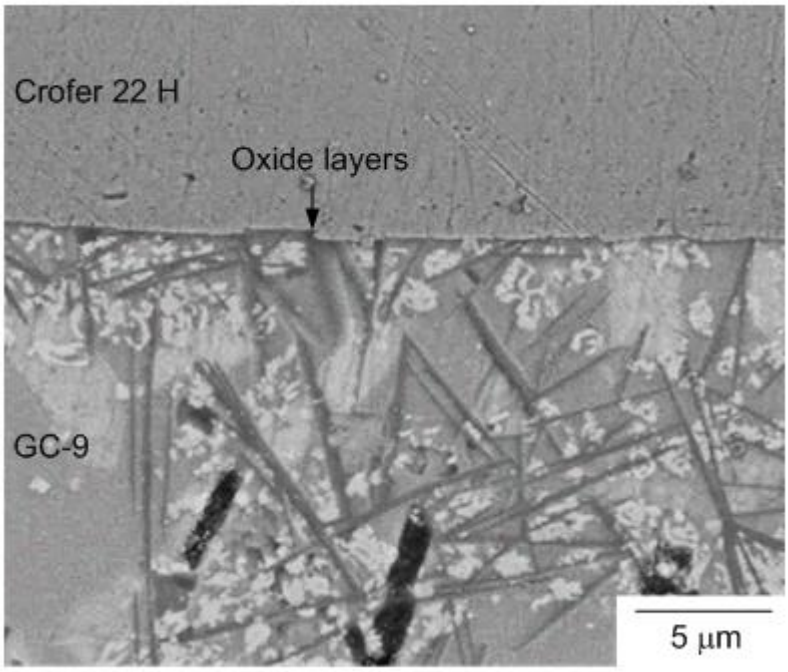

(a)

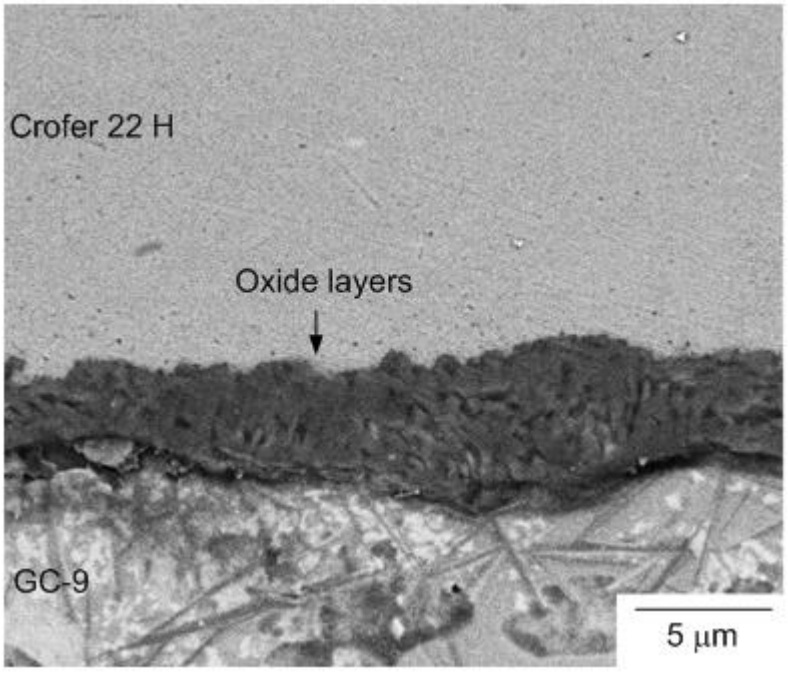

(b)

Fig. 51 SEM micrographs of a cross section of the interface between GC-9 and Crofer 22 H at variously aged conditions in BSE mode: (a) non-aged; (b) 100 h-aged; (c) 1000 h-aged.

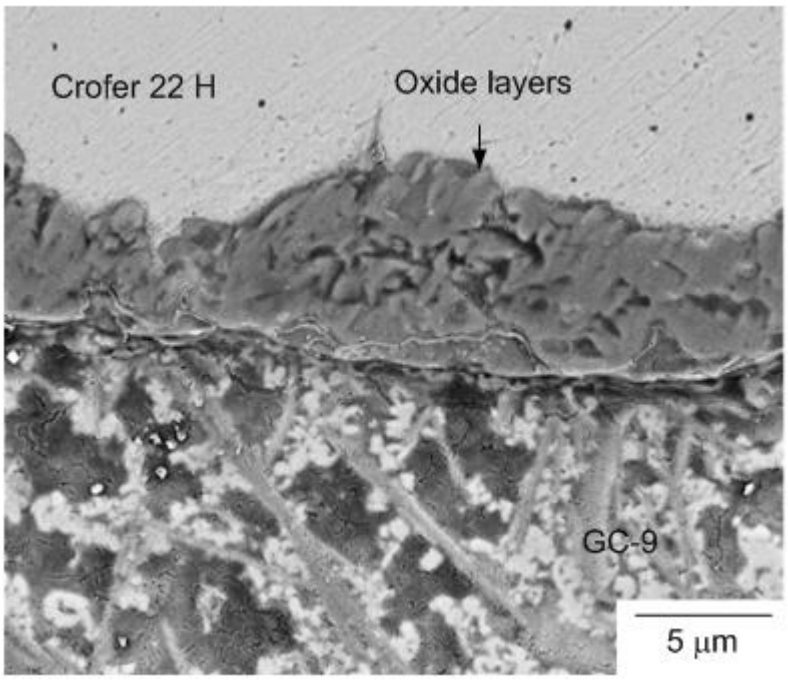

(c)

Fig. 51 (continued)

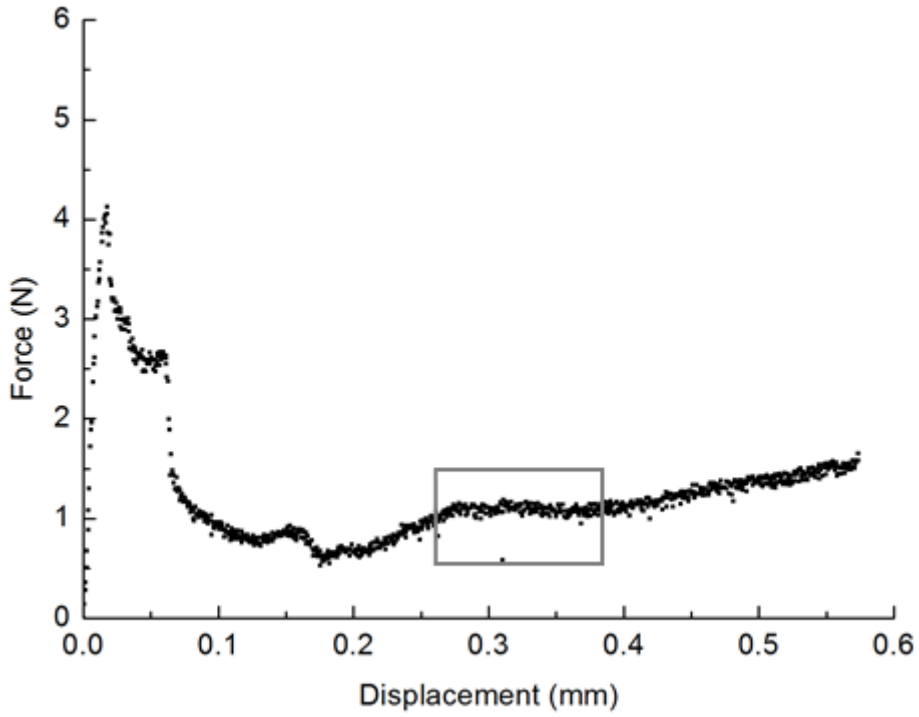

(a)

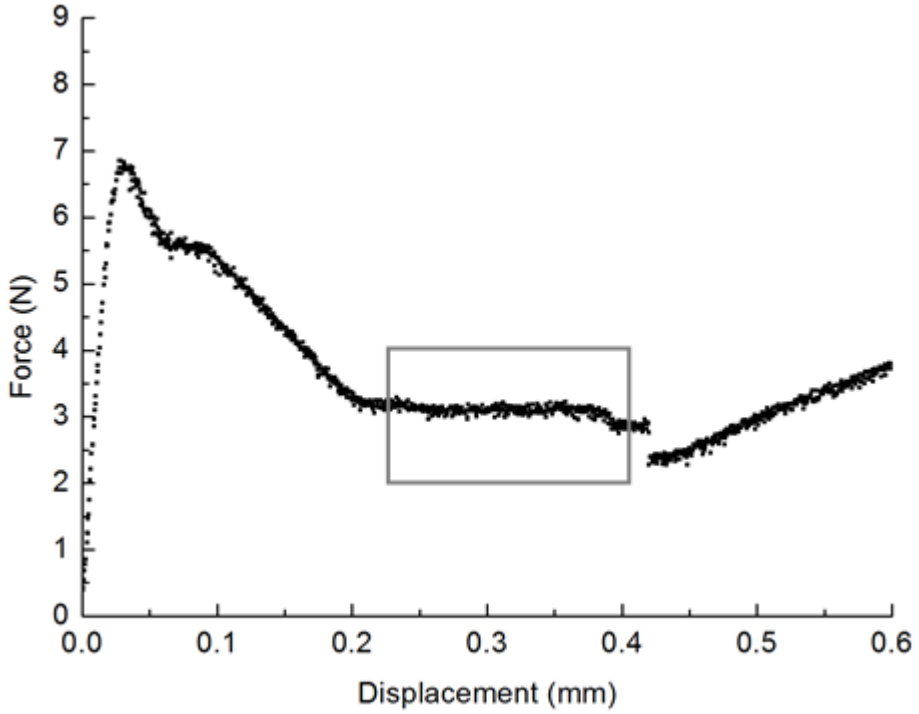

(b)

Fig. 52 Results of PEN/glass-ceramic/notched metallic interconnect specimens tested at room temperature: (a) load-displacement relationship for non-aged specimen; (b) load-displacement relationship for 100 h-aged specimen; (c) typical side view of specimen at outlined regions.

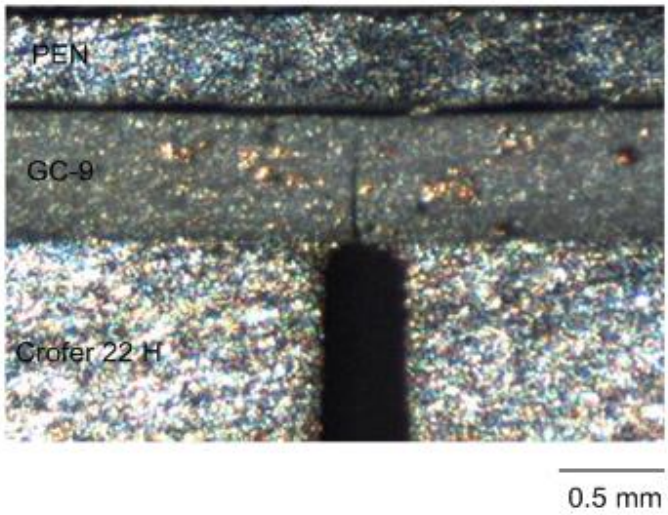

Fig. 52 (continued)

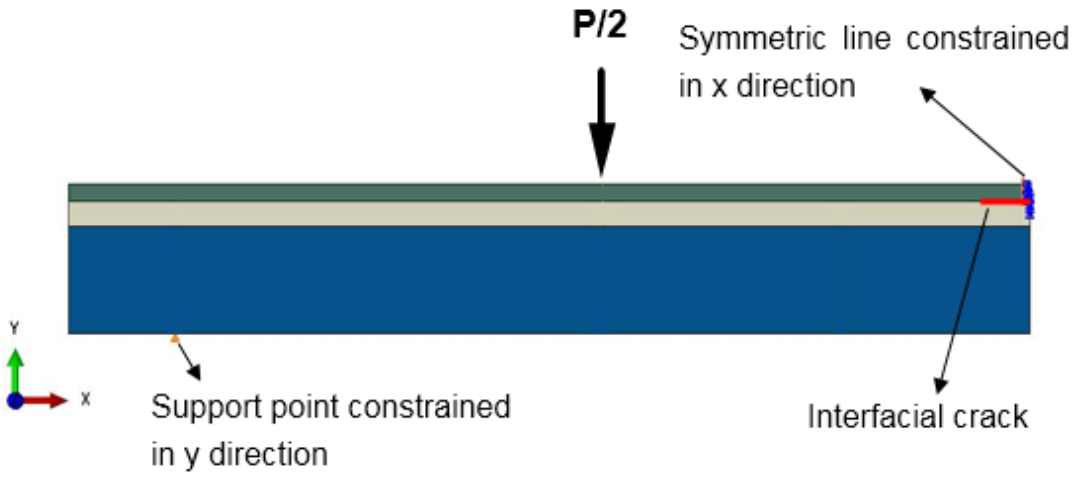

Fig. 53 FEA model for PEN/glass-ceramic/notched metallic interconnect specimen with a crack at the PEN/glass-ceramic interface.

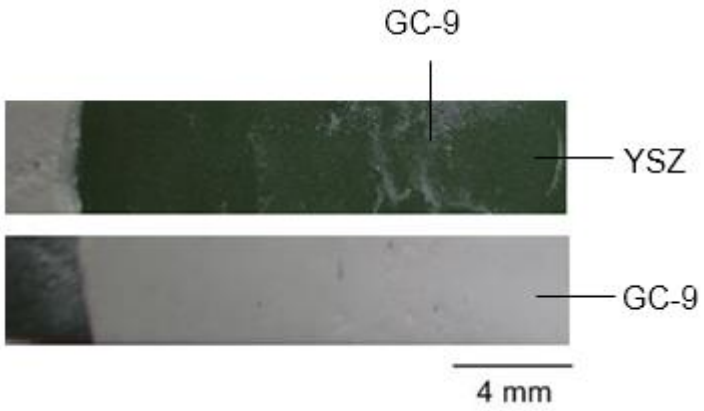

(a)

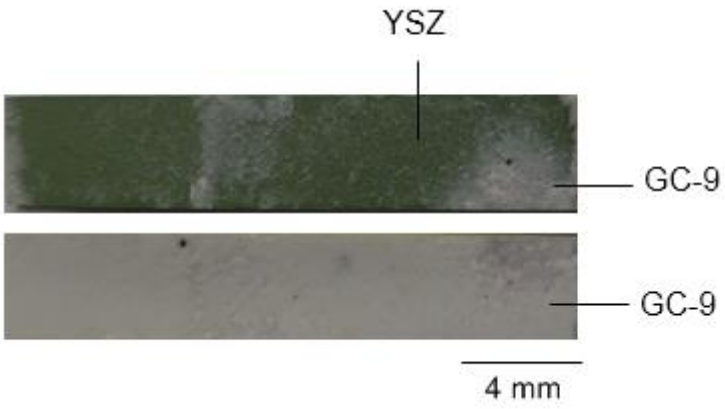

(b)

Fig. 54 Failure patterns of PEN/glass-ceramic/notched metallic interconnect specimens tested at room temperature: (a) non-aged; (b) 100 h-aged.

(a)

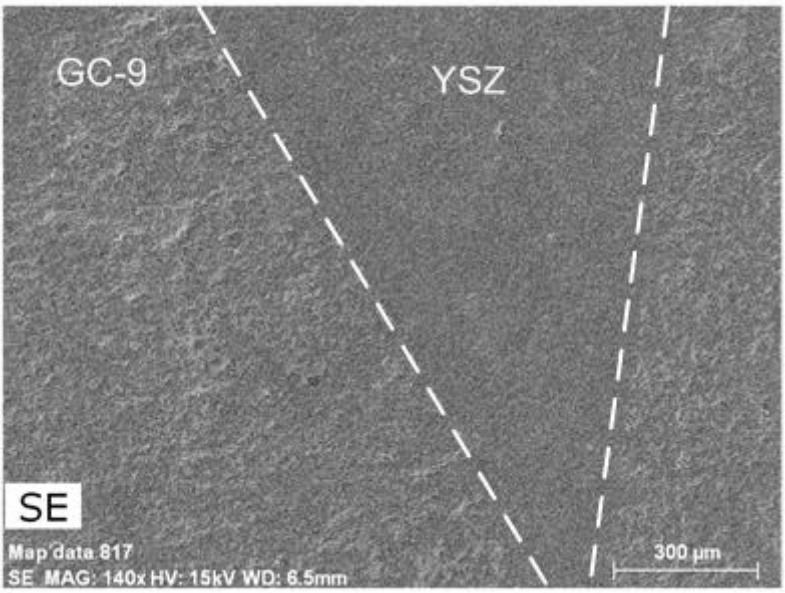

(b)

Fig. 55 A region selected in the upper micrograph of Fig. 54(a): (a) optical micrograph showing the outlined region for EDS; (b) mapping region; (c) element distribution of Ba (red) and Zr (green).

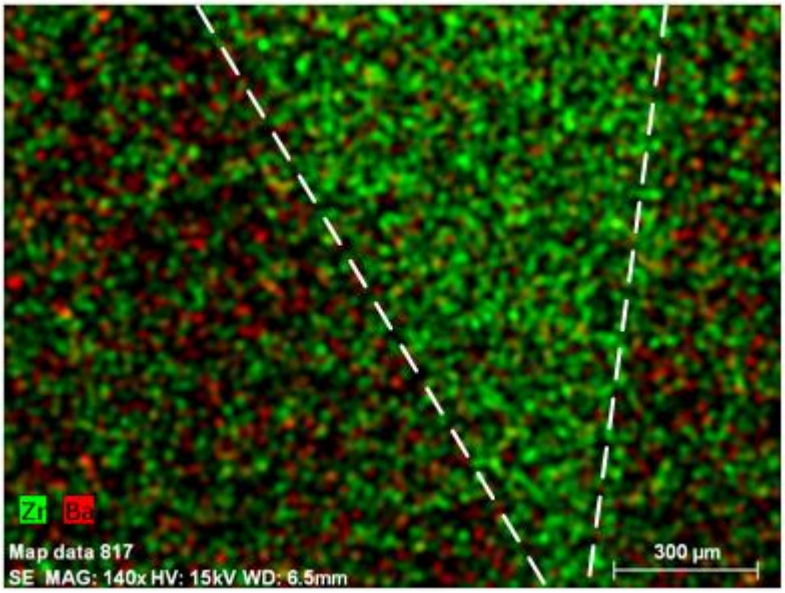

(c)

Fig. 55 (continued)

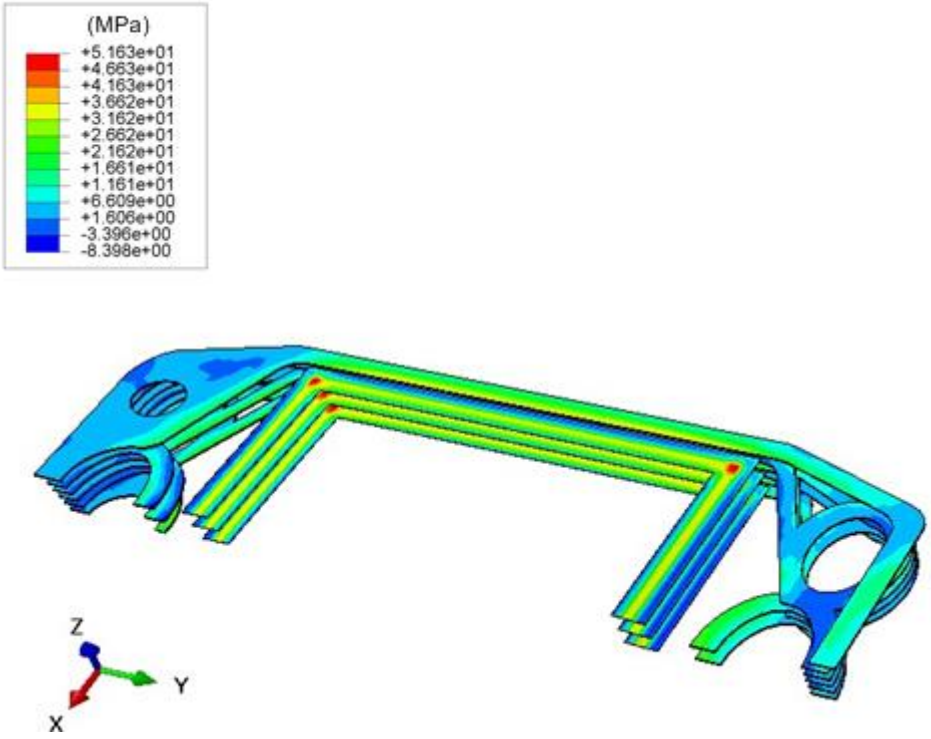

(a)

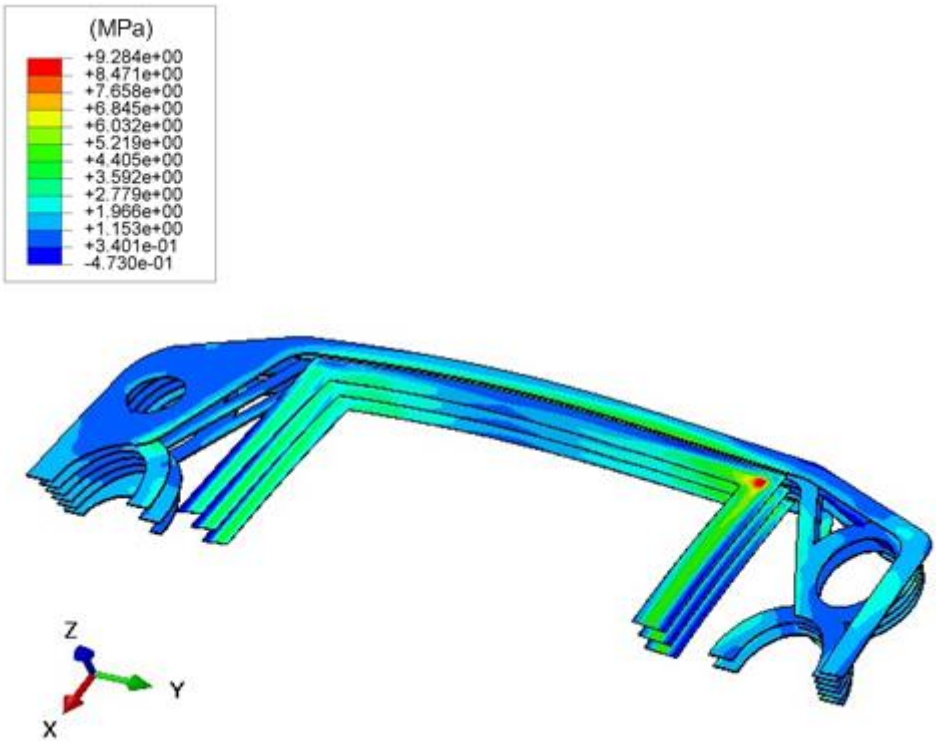

(b)

Fig. 56 Distribution of maximum principal stress for glass-ceramic sealants in an SOFC stack at various stages: (a) room temperature; (b) operation stage.

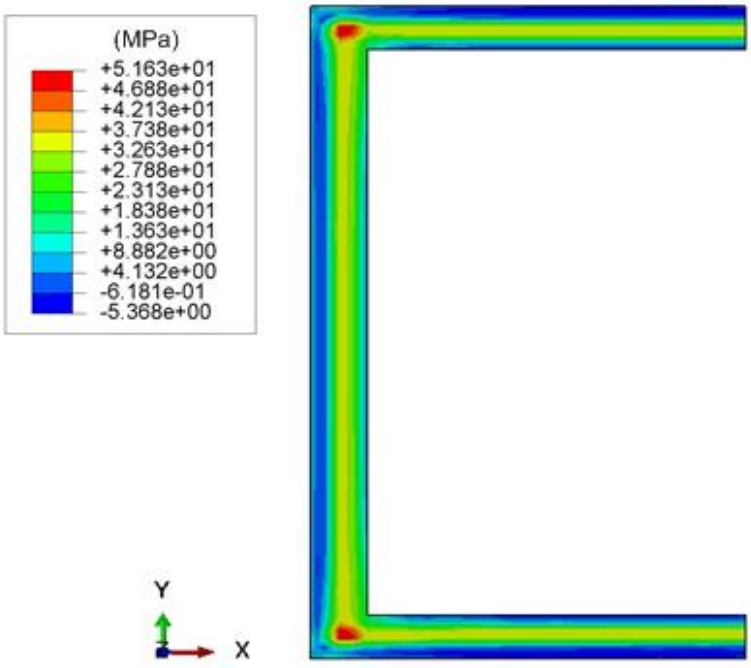

(a)

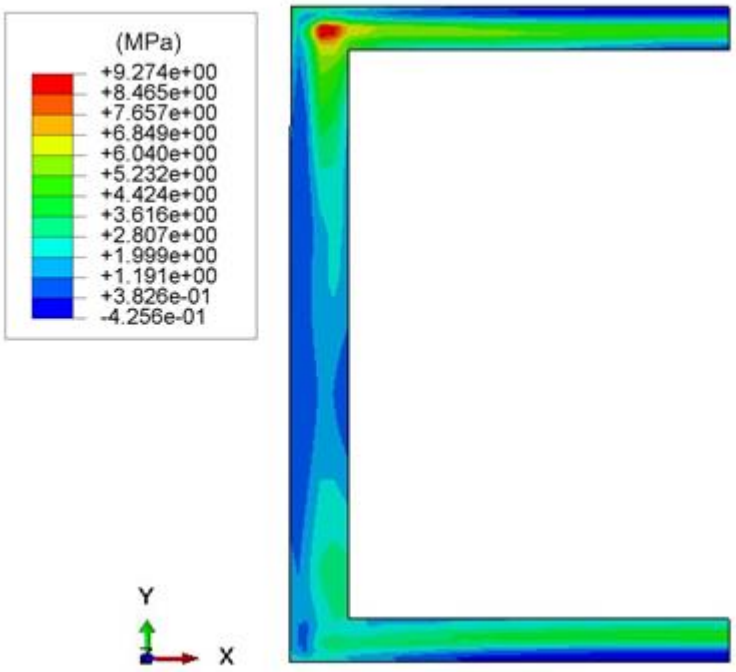

(b)

Fig. 57 Distribution of maximum principal stress for glass-ceramic sealant adjacent to the interconnect in the bottom unit cell at various stages: (a) room temperature; (b) operation stage.

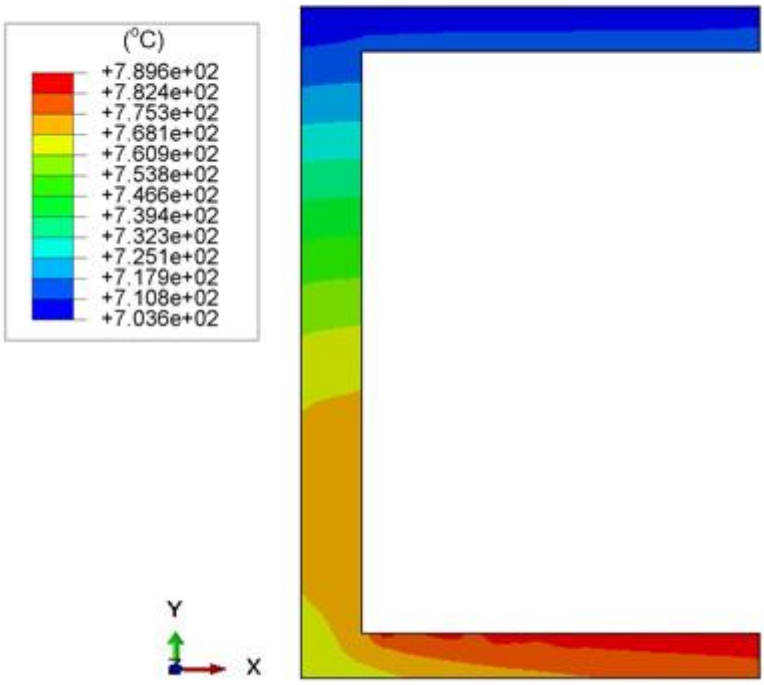

Fig. 58 Temperature distribution at operation stage for glass-ceramic sealant adjacent to the interconnect in the bottom unit cell.

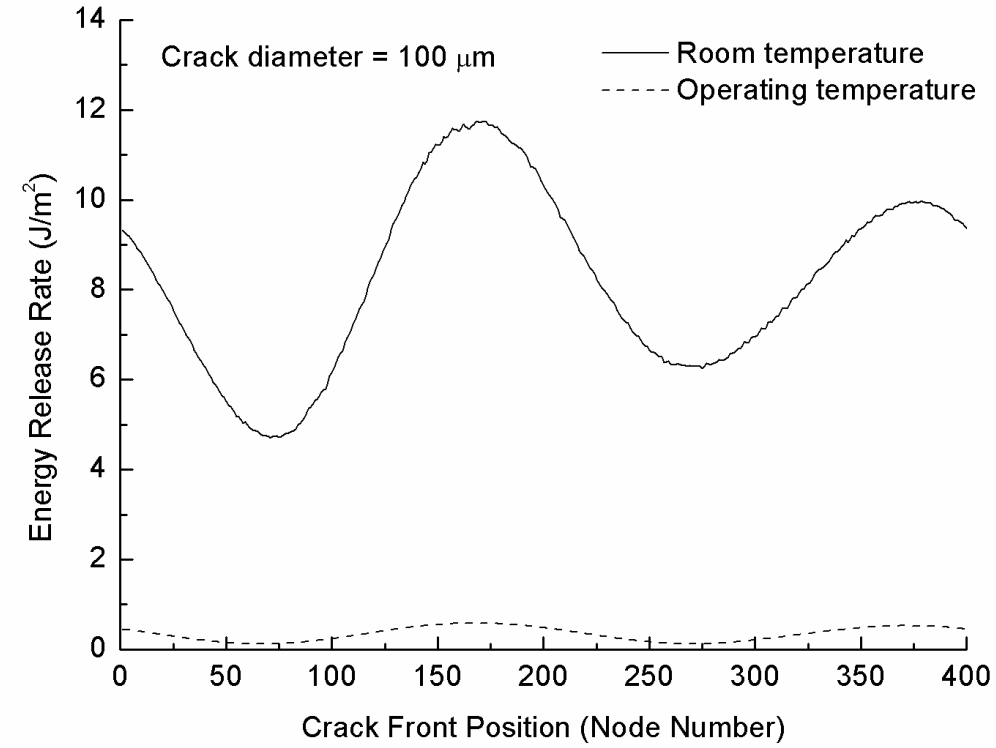

(a)

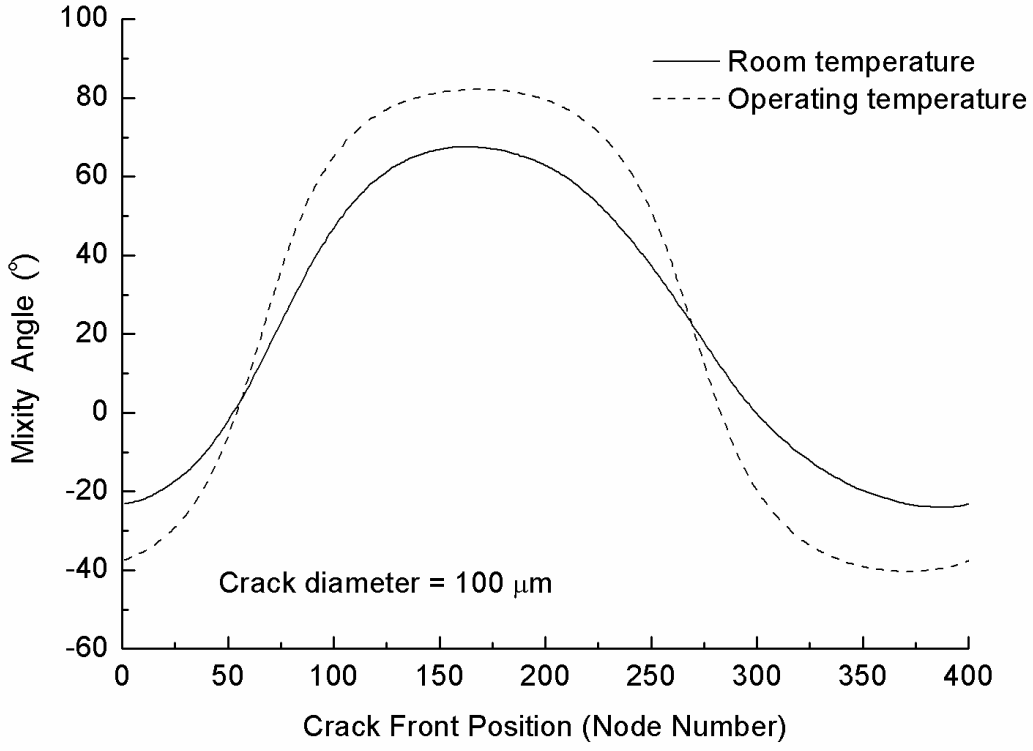

(b)

Fig. 59 (a) Calculated energy release rate along the crack front for crack diameter of 100 μm; (b) corresponding mixity angle along the crack front.

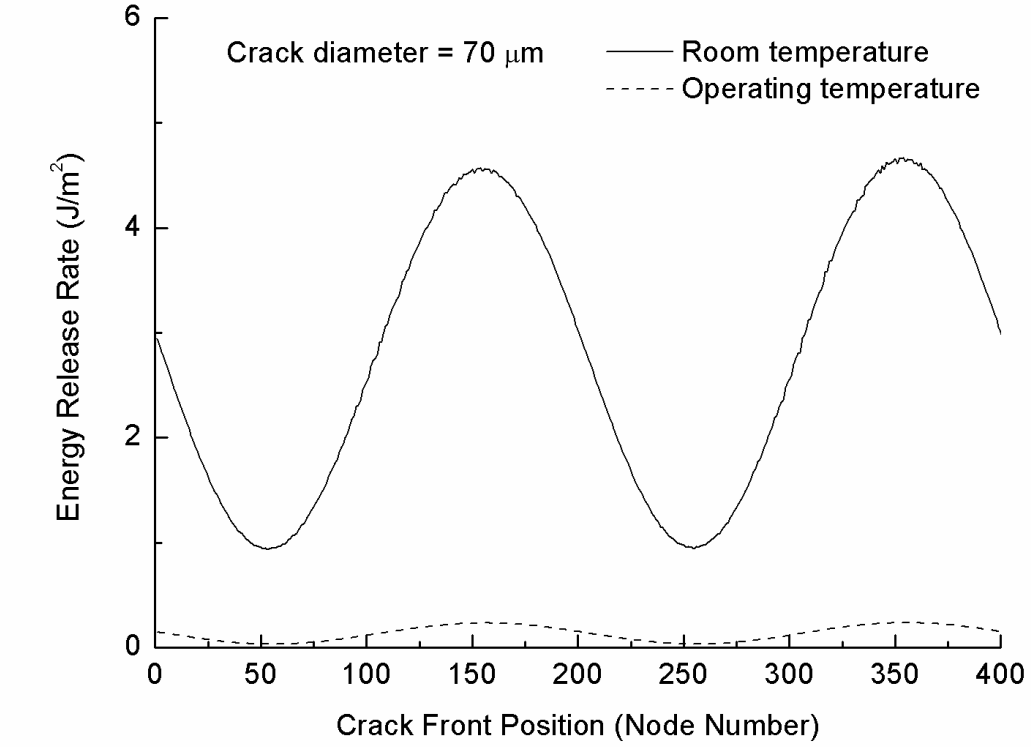

(a)

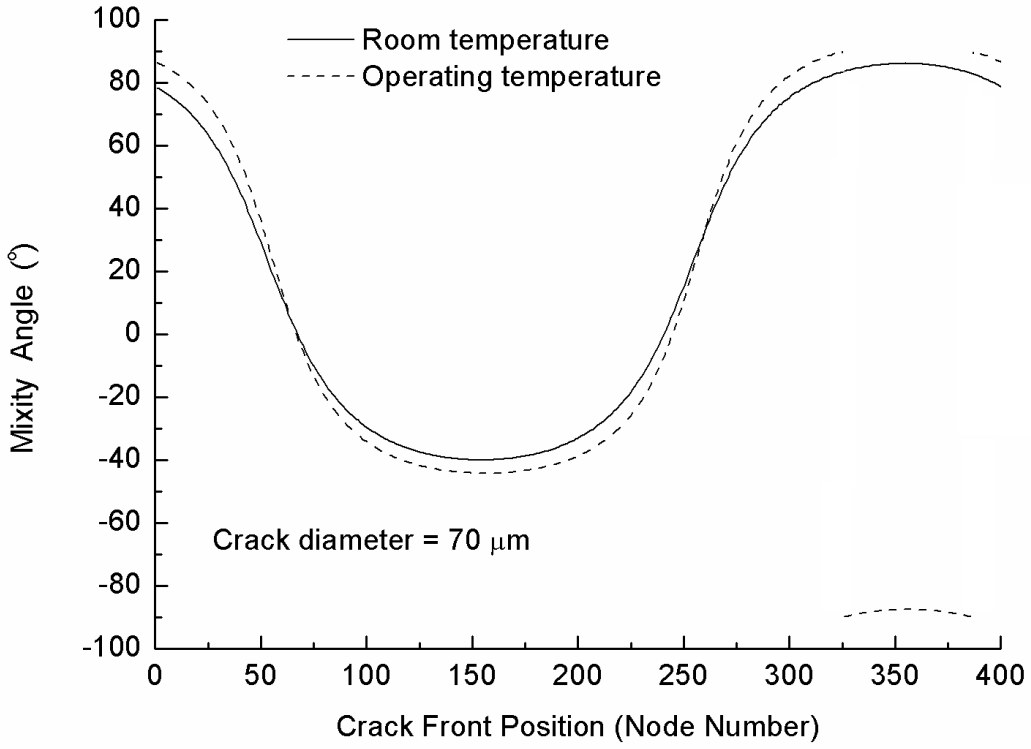

(b)

Fig. 60 (a) Calculated energy release rate along the crack front for crack diameter of 70 μm; (b) corresponding mixity angle along the crack front.